2015

System and process development for a coaxial extrusion nozzle for fused deposition modelling

Adam Christopher Taylor
University of Wollongong

UNIVERSITY OF WOLLONGONG

System and Process Development for a Coaxial Extrusion Nozzle for Fused Deposition Modelling

A thesis submitted in partial fulfilment of the

requirements for the award of the degree

Master of Philosophy (Mechatronic Engineering)

from

UNIVERSITY OF WOLLONGONG

by

Adam Christopher Taylor, BE (Hons) / BSc

School of Mechanical, Materials and Mechatronic Engineering

2015

Thesis Certification

I, Adam Christopher Taylor, declare that this thesis, submitted in partial fulfilment of the requirements for the award of Master of Philosophy, of the School of Mechanical, Materials and Mechatronic Engineering, University of Wollongong, is wholly my own work unless otherwise referenced or acknowledged. The document has not been submitted for qualifications at any other academic institution.

Adam Christopher Taylor (17/06/2015)

ACKNOWLEDGEMENTS

To successfully complete this work I have so many people to thank. I have received support in all different manners:

Firstly to my parents, Chris and Christine Taylor, you have encouraged me throughout the entirety of my life and have done your best to guide me to be the person I am today. I am eternally grateful for your ongoing support and your unknowing volunteering of your time to be a sounding board allowing me to vent about whatever is happening in my life. I would not be where I am today without you, I hope one day I can show how truly grateful I am.

To my beautiful Adriana, thank you for encouraging me to follow my passion and avoid avenues which were merely a means to an end. Thank you for supporting me to pursue my further study and tolerating my growing passion on all things engineering, even though sometimes my excited rants or explanations bore you half-to-death. You have changed my life in a way I never thought possible, you definitely are my better half. I'm glad one of us will be a Doctor of something, though one day I may want to catch up to you!

To my supervisor, Gursel Alici, firstly thank you for agreeing to let me into early entry for engineering from high school. You likely do not know that you sat in on my interview panel for early entry. I am so proud to have been one of your students, and I thank you sincerely for accepting to take me on as a postgraduate student and guiding me through my research. It has been an incredibly rewarding experience and I hope this is not the last of our work together.

To my supervisor, Stephen Beirne, thank you for allowing me to be a student of yours. Through the past year and a half I have viewed you as a mentor for academia and as a professional. You have allowed me to have creativity over this project and pushed me in a right direction when I was getting bogged down. You have been, and continue to be, a tremendous inspiration.

Fletcher, despite you not having any direct supervisory role with me, you have guided me significantly in my technical challenges and have an absolute encyclopaedic knowledge of all things engineering. Thank you for hearing out my ideas and educating me on the fine theoretical aspects of everything from the use of UHMWPE as crash pads to spot welding fine wires to meshes. I look forward to our next educational tangent.

To GGW and the team at IPRI and ACES, thank you sincerely for giving me the opportunity to work among you. You have welcomed me so warmly and always been so helpful where ever you could. Gordon, thank you for your guidance, you reminded me to look at the bigger picture, to see the next avenue for potential and pushed for bigger things to happen. To strive for the best I could in my work.

Thank you all.

ABSTRACT

Additive fabrication, commonly referred to as 3D printing, creates three-dimensional objects by depositing successive layers of a desired shape. While a number of additive processes currently exist, there is insufficient completed work regarding implementation of co-axial fabrication through any technique. Although initial progress has been made in this field, areas for potential improvement have been identified. This thesis has developed one of the first documented systems and associated processes to enable co-axial additive fabrication as a reliable printing method. This will expand the potential uses for these technologies and hence increase their appeal.

The developed integrated system allows two materials to be printed coaxially through the basis of fused deposition modelling (FDM). To do this, the printer must have simultaneous and independent control of two extruders. This feature, coupled with individual temperature control of up to 275°C for each heat chamber, allows for the device to facilitate a wide range of potential materials for extrusion. The materials extruded from this device form a fibre and sheath configuration with an outside diameter of approximately 900µm and an inside diameter of 400µm. This system produces fibres with a coaxial concentricity significantly lower than previous literature, reaching offsets as low as 2.89%.

In addition to this, a supplementary coaxial extrusion tip has been developed to allow for the creation of a coaxial coating process. This system facilitates the inclusion of pre-formed materials into the typical FDM process, allowing for the production of novel structures of increased complexity. The core material (a pre-formed material) is extruded passively by process of entrainment from the sheath material (typically a thermoplastic) and deposited in a layer-by-layer fashion. This has enabled the printing of conductive pathways using a variety of pre-formed materials with differing diameters (65µm iron and 190µm copper). A single thermoplastic coupled conductive pathway exhibits outside diameters of approximately 900µm and produces coaxial concentricity values which vary with core material diameter.

The outcomes of this research provide an opportunity to alter the paradigm of biofabrication by introducing a new level of versatility to the construction of biofabricated structures.

TABLE OF CONTENTS

LIST OF FIGURES

LIST OF TABLES

ABBREVIATIONS

A	Amperes (Units Amps)
ABS	Acrylonitrile Butadiene Styrene
AF	Additive Fabrication
BFB	Bits From Bytes
CAD	Computer-Aided-Design
CFD	Computational Fluid Dynamics
FDM	Fused Deposition Modelling
FGM	Functionally Graded Material
LENS	Laser Engineered Net Shaping
MJM	Multi-Jet Modelling
NiCr	Nichrome
PEEK	Polyether ether ketone
PLA	Poly(lactic acid)
PTFE	Polytetrafluoroethylene
R_a	Surface Roughness
SLM	Selective Laser Melting
V	Voltage (Units Volts)

PUBLICATIONS

Taylor, A., Beirne, S., Alici, G. & Wallace, G.G., "System and Process Development for Coaxial Extrusion in Fused Deposition Modelling" –Rapid Prototyping Journal (Under Review)

CONFERENCE PRESENTATIONS

Taylor, A., Beirne, S., Alici, G. & Wallace, G.G. 'Systems and Process Development for Co-Axial Additive Fabrication,' *4th Asia-Pacific Symposium on Nanobionics*, 15th November 2013, Melbourne, Victoria, Australia. (Poster Presentation)

Taylor, A., Beirne, S., Alici, G. & Wallace, G.G. 'Systems and Process Development for Co-Axial Additive Fabrication' *9th Annual International Electromaterials Science Symposium*, 12th-14th February 2014, Wollongong, New South Wales, Australia. (Poster Presentation)

Taylor, A., Beirne, S., Alici, G. & Wallace, G.G. 'Systems and Process Development for Co-Axial Additive Fabrication' *Australian National Fabrication Facility Annual Research Showcase 2014*, 18th-19th November 2014, Canberra, Australian Capital Territory, Australia. (Oral Presentation)

1 INTRODUCTION

Three-dimensional printing, also known as additive fabrication (AF) or additive manufacturing is an emerging technology finding applications in a wide range of industries. The crux of this concept lies in the addition of material in a desired geometry, essentially the opposite approach to traditional manufacturing. The process was initially praised for its ability to produce unique shapes quickly and at a reduced cost, coining the term 'rapid prototyping'. It became a useful asset to designers and engineers allowing concepts to be realised on a smaller scale, though the technology quickly found its way into further research.

AF has developed to fill the needs of its users worldwide. The initial process relied on the solidification of photocurable polymer resins, though a plethora of materials quickly became available, along with numerous additional processing methods. The current state of the technology, regardless of fabrication process, allows objects created using Computer-Aided-Design (CAD) software to be produced using the process shown in Figure 1.1.

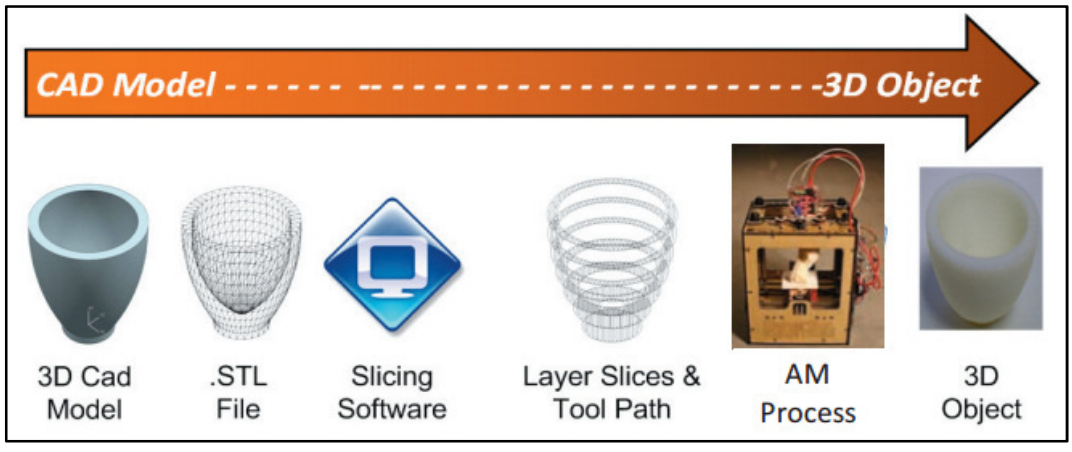

Figure 1-1 - Typical Additive Fabrication Process[1]

Each AF process has its distinct advantages and associated materials for object production. Fused Deposition Modelling systems focus on thermoplastics and are the most dominant method across industries, Selective Laser Melting (SLM) systems use metal powders while Stereolithography (SLA) uses liquids. Despite the many methods available, few AF processes offer the potential to combine materials while operating. Materials produced as a result of mixing are known as functionally graded materials (FGM) and are a developing area of AF.

The desire to create FGMs is a result of the necessity to expand the range of use for AF processes. This area of research aims to provide customisation over the composition of materials produced through filament, powder or liquid based fabrications and processes. Increasing the complexity of components produced, enabling a method to fabricate unique structures which blend materials to enhance their characteristics or performance.

A recent addition to the development of FGMs is the theme of coaxial extrusion. This concept aims to use filament based systems to produce a fibre and sheath extrusion. In doing so, the central material is entirely encapsulated by the external material. This process allows for the production increased complexity into fabricated structures, primarily focusing on the ability to utilise biocompatible or biodegradable materials, with conductive ones.

Current developments into coaxial extrusion are minimal and have great potential for application within the biomedical industry. This identifies an opportunity for advancement to a developing research area. The creation of a reliable and robust method to fabricate coaxial structures will fill the void and contribute to the continuous requirement of enhancing AF processes for further use.

The research presented in this thesis is designed to fulfil the requirement for developments in coaxial extrusion. This work endeavours to create one of the first controllable FDM systems capable of fabricating coaxial, multi-layer structures as well as conductive coaxial structures.

Placing emphasis on obtaining reliable concentricity of the fibres produced, while enhancing the materials for potential use by maximising the operating temperature of the device.

1.1 ADDITIVE FABRICATION

Additive fabrication, is defined as a "process of joining materials to make objects from three-dimensional model data, usually layer upon layer" [2]. When comparing this method with traditional manufacturing, it is evident that AF relies on the concept of addition of material where required, while traditional methods remove unwanted material to create the desired geometry. This results in a process that is more efficient from a material consumption perspective, though it has shown to lack efficiency in time to manufacture [3].

With the development of this technique originating in 1984 [4], the past three decades has shown a dramatic increase in the research and development of this field. The initial AF process was stereolithography, a process which forms three-dimensional objects by directing an ultraviolet light beam onto a photocurable material, resulting in a state transformation from liquid to solid. This technique results in a single layer of cured photopolymer resin, taking the shape of the desired cross section of the object at that instance. This method is repeated to create successive cross sections of the desired object, forming a layer-by-layer construction of the required geometry.

Since its creation, AF technology has developed to encompass many new methods for object realisation. Table 1.1 shows a summary of current AF processes classified by their initial construction material.

These processes service a variety of industries including, aerospace [5, 6], automotive [7], biomedical [8-10] and tooling [11]. Each industry utilises the desired method for a number of

reasons; though a common theme is the ability to manufacture using materials with unique properties [12-16]. AF processes can use materials which are biocompatible, biodegradable, conductive or insulating; while varying the density of the materials deposition. However, despite the recent expansion of research and development into these techniques, additional progression needs to be made to further enhance their capabilities.

Several milestones exist as markers to further improve these processes and their array of applications. Widely recognised [17-23], the regions for development are, expanding materials for use, enhancing the speed at which the fabrication processes occur, increasing the resolution for produced parts, and reducing the price of AF technologies. Within the concept of expansion of materials lies the desire for Functionally Graded Materials (FGM) [17, 24, 25], a prospective avenue which would benefit all fabrication processes. While resolution and fabrication speed differ from process to process they are directly linked to one another. Producing a part of increased resolution will require additional time to produce, and vice versa.

Table 1.1 - Summary of Additive Fabrication Processes

Material State	AF Process	Formation Material	Layer Construction Method	State Transformation	Typical Materials	Potential Applications
Liquid	Stereolithography	Liquid Resin Vat	Laser scanning	Photopolymerisation	UV curable resins, ceramic suspension	Prototypes, casting moulds, soft tools
	Multi-Jet Modelling (MJM)	Liquid Polymer	Ink-jet printing	Photopolymerisation and cooling	UV curable acrylic plastics	Prototypes, casting moulds
	Rapid Freeze Prototyping	Liquid Droplet	On-demand droplet deposition	Solidified by freezing	Water	Prototypes, casting moulds
Powder	Selective Laser Sintering	Powder on Bed	Laser scanning	Partial melting	Thermoplastics, metal and ceramic powder	Prototypes, casting moulds, metal and ceramics
	Selective Laser Melting (SLM)	Powder on Bed	Laser scanning	Full melting	Metal	Tooling and functional components
	Electron Beam Melting	Powder on Bed	Electron beam scanning	Full melting	Metal	Tooling and functional components
	Laser Engineered Net Shaping (LENS)	Powder injection	On-demand powder injection and laser melting	Full melting	Metal	Tooling, metal part repair and functional components
	Three Dimensional Printing	Powder on Bed	Drop-on-demand binder printing	-	Polymer, metal and ceramic	Prototypes, casting moulds and tooling
Filament / Paste	Fused Deposition Modelling (FDM)	Filament	Continuous extrusion and deposition	Solidified by cooling	Thermoplastics	Prototypes, casting moulds
	Robocasting	Paste	Continuous extrusion	-	Ceramic paste	Functional components
	Freeze-form Extrusion Fabrication	Paste	Continuous extrusion	Solidified by freezing	Ceramic paste	Functional components
Sheet	Laminated Objective Manufacturing	Laser Cutting	Feed and bind sheets with adhesives	-	Paper, plastic and metal	Prototypes, casting models
Gas	Selective Laser Chemical Vapour Deposition	Gases	Condensation of gas	Chemical reaction	Metal and ceramic	Material coating and micro-scale structures

[3, 25, 26]

1.2 FUNCTIONALLY GRADED MATERIALS

A functionally graded material is a composite material which consists of a change in volume percentage of its contents as distance along the component varies[27], as shown in Figure 1.2 Often used as coatings, they are employed to reduce mechanical stresses on the core material, enhance surface characteristics, protect against environmental factors and increase bonding strength. The ability to produce FGMs allows a composite material to be designed for a unique application where typical single materials would not suffice.

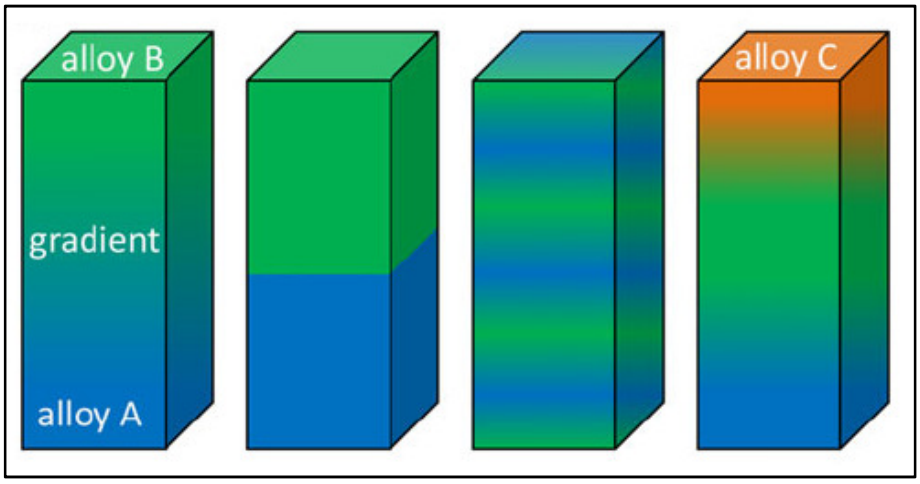

Figure 1-2 - Range of Functionally Graded Material Compositions. Adapted from[28]

FGMs were created in 1987 as a means to accommodate a 1000^{o}K thermal gradient across a 10 mm thickness [29]. Since then, their associated manufacturing processes have been limited to traditional concepts such as slip-casting, centrifugal casting, thermal spraying and electrophoretic deposition [30]. While these methods are capable of achieving the desired material gradients, they are limited to the production of simplistic geometries. To overcome this restriction, significant research has been done to the production of FGMs through AF processes, thereby enhancing the complexity of the objects to be created [31-35].

These unique materials have emerged across many industries, enabling a new technology to be possible where their predecessors failed. In aerospace, FGMs are used for their ability to tolerate very high temperatures, such as those found in rocket casings [36]. These materials also offer a resilience to crack propagation, making them of interest to the defence industry for the creation of bullet-proof vests [37]. Their ability to act as thermal sensors has attracted industry-wide interest [32].

Of all sectors being impacted by FGMs, biomedical has undergone one of the most significant enhancements from this technological shift. As graded materials are naturally occurring structures such as bones, teeth and tissue, they have the potential to be remodelled and produced using this technology [10, 33, 38, 39]. Though these structures are geometrically complex and unable to be created by traditional methods, AF offers the ability to fulfil this requirement. The subsequent sections examine in detail AF processes which are developing FGM integration, or those which are used in this work.

1.3 LIQUID ADDITIVE FABRICATION

1.3.1 Multi-Jet Modelling

Multi-Jet Modelling (MJM), as shown in Figure 1.3, builds up a structure layer-by-layer as with all AF processes. It supplies material in a method similar to a typical ink-jet printer; with each pass over the area, the required material is deposited in the desired configuration. The material used to build structures is a thermopolymer liquid, cured by an ultraviolet light which passes over the build area with each layer of new material deposited. As one layer is complete, the base lowers a distance equal to the thickness of one layer and the process is repeated, allowing for the construction of multi-layer components [25, 40].

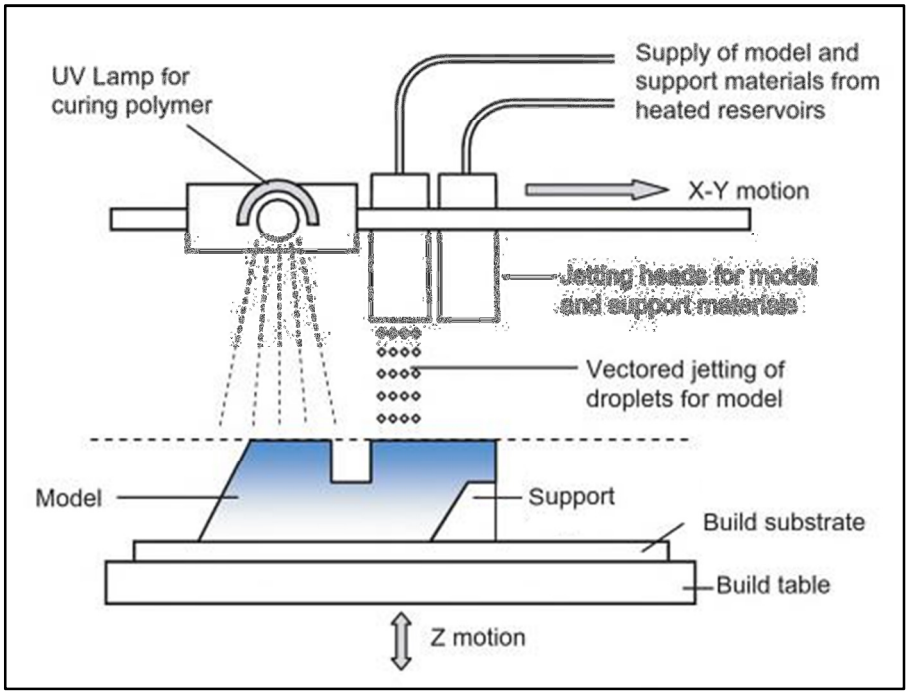

Figure 1-3 - Principle of Operation for Multi-Jet-Modelling Systems. Adapted from [41]

This process is primarily used for model visualisation [40], though the technology has progressed significantly, allowing current MJM machines to utilise many additional materials which may be high temperature, rigid or transparent [42]. The wide range of material selection and fine structure resolution obtained has allowed MJM to become a dominant form of AF [43]. With this developing reputation and advancement in potential materials, additional research is being conducted into its potential to create FGMs.

Producing FGMs through MJM is a developed concept which has progressed through to commercial applications. A typical early example of the technology involves the production of multi-layer structures using two aqueous suspensions [44]. These materials were housed separately within the MJM system and combined upon application. Given the liquid state of the raw materials used in this technique, it is possible to combine the materials in one pass of the print head. This is done by depositing both materials over the same area and curing them simultaneously. Using this technique, these two materials have been varied completely within one structure, producing a component which initiated as 100% material A and finished with

100% material B, linked by a linear gradient. Commercial devices capable of MJM offer potential to combine hundreds of composite materials within a single printed component [45].

This area of AF processing offers great variability in its components it can produce, as well as a capability to create FGMs. However, the spray based mechanics of material deposition for MJM does not provide a means to produce coaxial structures and appears unlikely to do so in the future. This limits the production of FGMs to dispersion mixing processes and eliminates this fabrication process from creating clearly defined coaxially concentric objects at lower resolutions.

1.4 POWDER ADDITIVE FABRICATION

1.4.1 Selective Laser Melting

Selective laser melting (SLM) uses a concentrated laser beam to melt a thin layer of metal powder in a specified pattern. The process is performed in a chamber of inert gas to eliminate contaminants and oxidation, as seen in Figure 1.4. After each melting pattern, the build platform is lowered one layer depth and a metal powder is spread over the platform. This process is repeated until the object created from a CAD model is produced from the defined material [25].

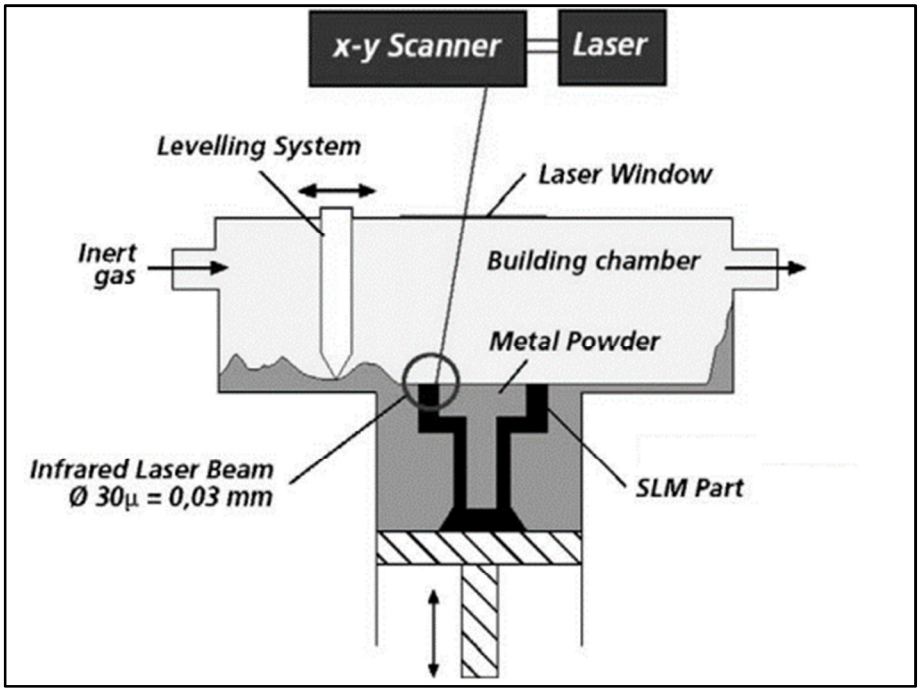

Figure 1-4 – Operating Principle for Selective Laser Melting. Adapted from [46]

This fabrication method enables the production of metal components with high mechanical properties, similar to that of rolled sheet metal. However, SLM is prone to the generation of internal stresses and part deformation as a result of the high energy levels required to melt the metal powders [47]. These undesirable effects are more likely to be produced in components with large cross sectional areas and of a large height. Consequently, these factors cause degrees of uncertainty in the dimensional accuracy of the produced part.

SLM is capable of fabricating parts using materials such as stainless steel, cobalt chromium, aluminium, nickel as well as titanium alloys; each offering their unique characteristics for the production of complex geometries. The powders associated with the printing process affects both the minimum dimension size of the component as well as the surface roughness (R_a) while the layer resolution remains unchanged at 25µm. Titanium alloy (Ti6Al4V) powders for use in this thesis typically have particle sizes of between 25µm and 65µm. This reduces the possible minimum dimensions to 150µm, and creates surface roughness up to a maximum of the power particle size [48].

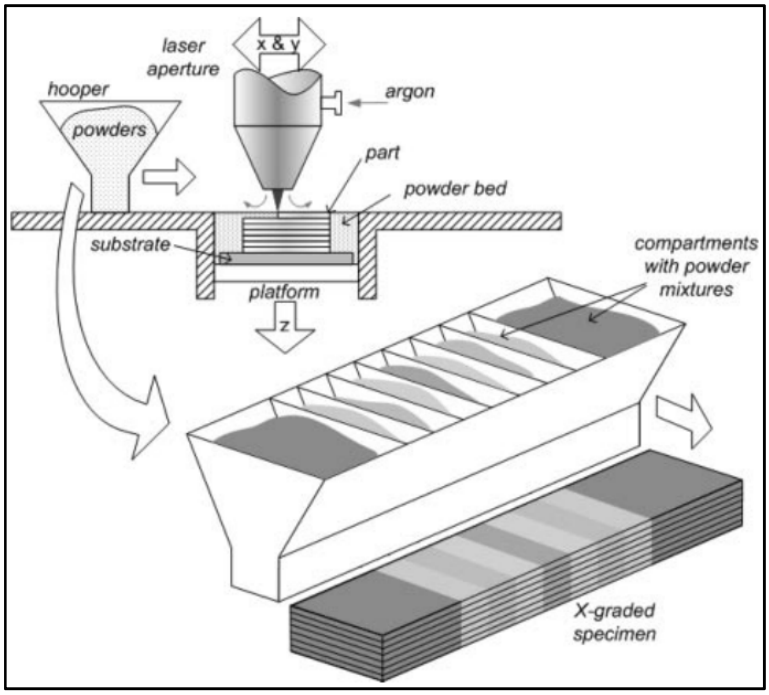

Figure 1-5 - FGM Powder Deposition Method for SLM. Adapted from [48]

This fabrication process has been developed for the creation of FGMs few times due to the difficult nature of the powder coating process. Multiple powders can be processed within a single SLM fabrication process using methods such as the one shown in Figure 1.5. Using this multiple powder configuration, materials with a 50% gradient can be produced [49], though achieving fine control in composition is difficult to obtain. Though this technique offers potential for FGM creation, coaxial structures have not been created. Additionally, given the mechanics behind material deposition, it is highly unlikely that this fabrication method will be capable of creating coaxial structures without significant modification to the overall design.

1.4.2 Laser Engineering Net Shaping

Laser Engineered Net Shaping (LENS), or laser cladding, is an AF process similar to SLM, though the metal powder is sprayed in a gas jet rather than being deposited across a print bed, as seen in Figure 1.6. These powder jets are typically positioned coaxially around the laser beam

with the powder arriving near perpendicularly to the substrate [50]. The laser then melts the deposited powder in a specified geometry within an inert chamber, protecting from oxidation and contaminants, and containing the powder spray. The substrate is then lowered one layer thickness and the process is repeated layer-by-layer until a fabricated component results.

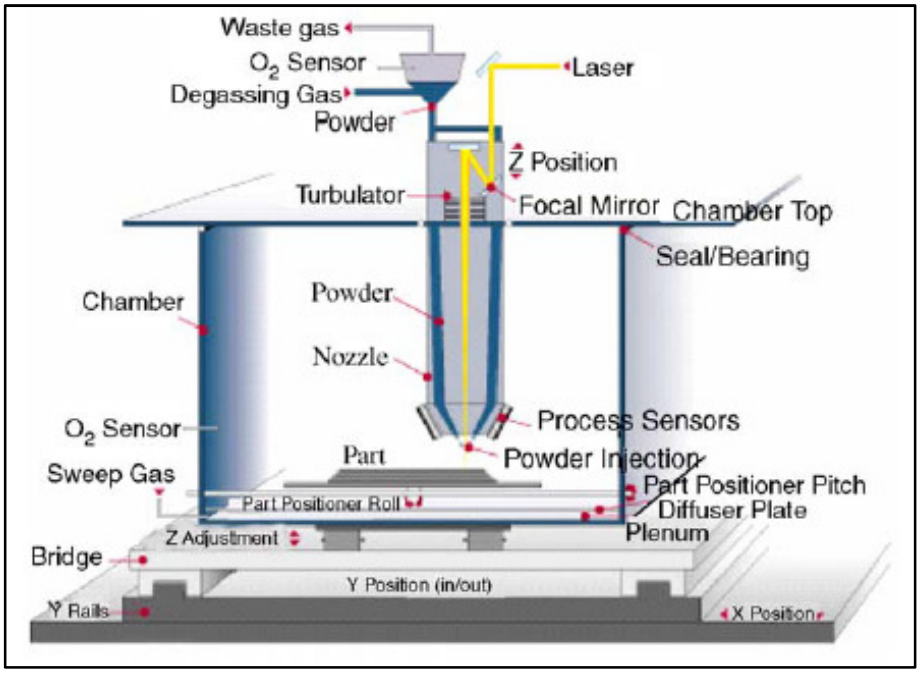

Figure 1-6 – Operating Principle for Laser Engineered Net Shaping. Adapted from [51]

The LENS technique produces materials from titanium, aluminium or cobalt alloys with mechanical properties similar to that of traditional manufacturing [52]. Additionally, this fabrication method offers the ability to create structures on existing parts, allowing for easy coating processes, or for the repair of damaged components. However, this technology lacks the ability to create components with any material overhang, implying any angular component must have supporting structure. This limits the speed of component production for objects which are not perpendicular to the substrate. This creates an increase in fabrication time for geometries with angles less than 45^{o} when compared to SLM.

As this method of fabrication relies on an in situ supply of powder to the laser, it allows an easy transition to fabricate FGMs. This widely developed concept [25, 53-55] typically utilises

two differing metallic supply powders, allowing for a great range of control over the composition of the produced materials. This process allows a full transition from material A to material B within the same component. While LENS is the most developed technique for metal based FGM creation; its mechanism of action renders it unable to fabricate structures of a coaxial nature. The powder deposition system renders this improbable, though a significant restructure of the process may allow for this to be possible. By allowing a powder jet to take the central axis of the nozzle, implementing a coaxial laser system, and retaining the coaxial powder jet, it could be feasible to create vertical coaxial metal structures.

1.5 Filament Additive Fabrication

1.5.1 Fused Deposition Modelling

Fused deposition modelling emerged as an AF process in 1992 and has rapidly become the leading method across industries, with more FDM machines used than any other AF machine [56]. This process (Figure 1.7) heats materials, primarily thermoplastics, beyond their melting temperature for a short period of time. This molten material is then deposited onto a surface as a continuous extrusion, following a predefined pathway to create an individual cross-sectional layer of an object. Subsequent layers are created by increasing the distance of the z-axis by the previous layers thickness and repeating the deposition process, with the newly deposited molten material adhering to the previous layer; allowing the creation of multi-layer structures of a desired geometry [25].

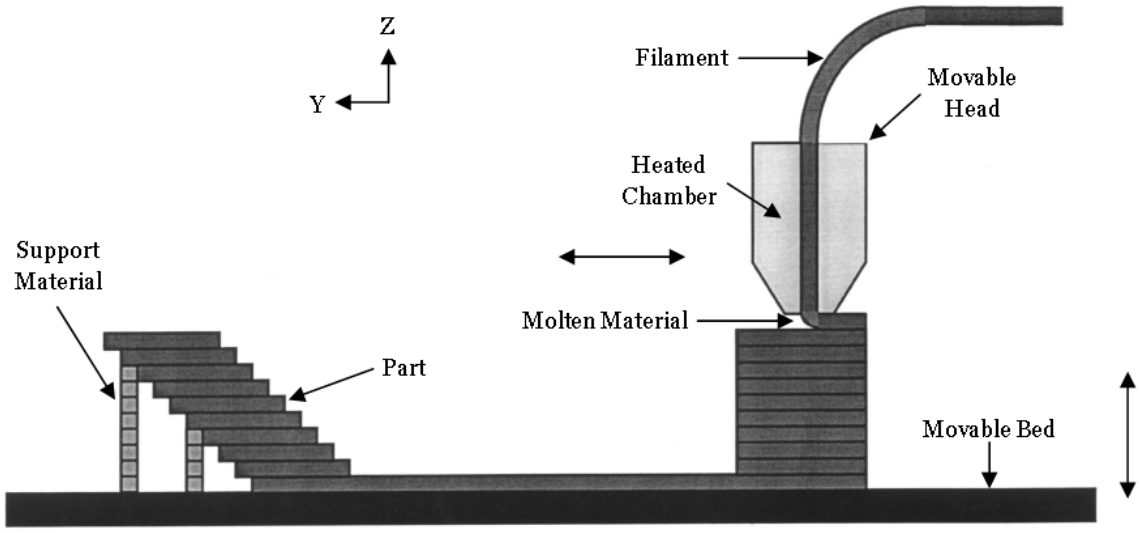

Figure 1-7 - Overview of a Fused Deposition Modelling System. Image adapted from [40]

This process has gained a strong reputation as a result of its simplistic, affordable and reliable component production, making it widely adopted by consumers and industry alike [57]. The FDM method has also attracted the interest for the research and development of future materials and enhancements to the process, notably by expanding to a multi-nozzle system where each can deposit a different material [58]. This process allows for the desired object to be fabricated with one material, and the support material to be created using another. Often, the supporting material will be one which may be easily dissolved without significantly altering the structure of the printed object, allowing for easy removal of support in complex geometries.

Expanding upon this, and linking FDM research and development to the milestones mentioned in Section 1.1. Work is currently being done to create FGMs through multi-ceramic deposition [59] and expanding materials for use such as Nylon [60]. However, minimal work has been done to create a constant graded functional material, one in which a gradient is present and remains so throughout the entire fabrication process. This method involves the coaxial extrusion of two materials and is discussed in detail in the following section.

1.6 COAXIAL ADDITIVE FABRICATION

A coaxial structure is one in which two materials are present and share a common axis. This structural configuration is commonly found in conducting cables, where the internal material is conductive in nature and the external is insulating, protecting the core from the environment and permitting the desired transfer of the signal. In the scenario of fused deposition modelling, they will take the form of concentric circles, forming a fibre and sheath configuration.

Traditional methods for the extrusion of plastic structures involves the material being heated to its melting point and forced through a die to obtain the desired geometry [61], similar to the FDM process. At this point, the polymer swells due to relaxation and is then pulled to reorientate the polymer chains, reducing the size back to that of the extrusion die. The resulting extruded material is cooled and solidified before post-processing operations take place.

For the co-extrusion of plastics, the process is similar, though it involves a more complicated die design to accommodate the input of additional materials for extrusion. Figure 1.8 shows a three layer coaxial extrusion die in which the output material exhibits an A/B/C/B/A structure [62]. While the concept of single material die extruding molten plastics is the basis for fused deposition modelling, the method of co-extrusion has had limited development in its application to AF.

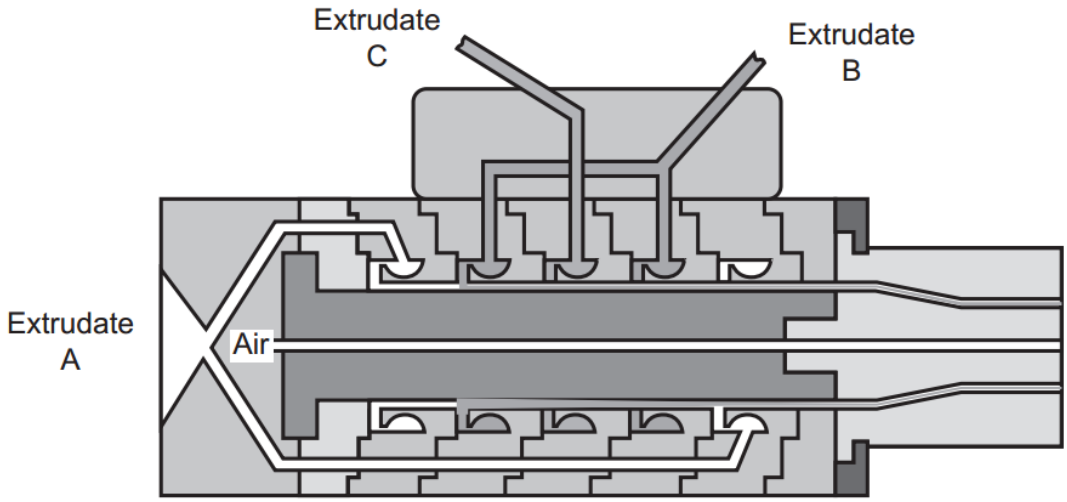

Figure 1-8 - Coaxial Extrusion Die [63]

Initial documented research into a side-by-side co-extrusion AF process was created for industry use in 2013 [64]. The Palo Alto Research Centre (PARC) developed a technique to enhance the power density of their batteries and the speed of their production. This process enabled the deposition of dissimilar, highly viscous materials, side by side at high speeds, while obtaining micron range resolutions. While this work will impact the enhancement of AF techniques, it does not address the need to expand into the production of coaxial structures for fabrication capabilities.

The first research into merging coaxial extrusion techniques with AF was completed in 2010 [65]. This work developed a means to produce a three-dimensional porous collagen scaffold with an alginate core. The scaffold was created through a solid freeform fabrication of collagen and alginate coupled with a cryogenic and freeze-drying system. The coaxial nozzle had an inner diameter of 175µm and an outer diameter of 500µm with the resultant structures showing a high level of dimensional accuracy. However, no measurements were made regarding the concentricity of the coaxial fibres, with a majority of the data suggesting the structures were not symmetrical about their longitudinal axis.

Subsequent work into coaxial extrusion in AF involved the modification of a bioplotting device, a similar concept to FDM though commonly used for low temperature biological fluids. This research primarily targeted coaxial extrusion of organic materials and their incorporation into scaffold structures; specifically, the use of poly-ε-caprolactone (PCL) and a composite PCL graphene material [66]. The designed tip exhibits diameters of 900µm and 300µm for external and internal, respectively. The fibres produced by this tip have dimensions of 800-700µm and 460-300µm for external and internal materials, respectively.

This research considers the importance of developing an accurate, reliable and repeatable process in producing coaxial fibres through an AF process. The reliability of the device is assessed by measuring the offset of the core materials longitudinal axis from the external material's longitudinal axis. The bioplotting coaxial process reports axis offset averages as low as 22%, though the method for obtaining this percentage is not defined.

1.7 RESEARCH OBJECTIVES

The literature has indicated an opportunity for improvements to existing research. This work builds upon previous developments by aiming to enhance the variability of structures which can be produced coaxially through an FDM system. This is done by modifying the framework of an existing FDM machine to accommodate a coaxial extrusion tip which is designed with the intent of producing high resolution coaxial structures.

The thesis aims to enhance the abilities of an FDM system by accomplishing the following primary goals:

1. Produce a thermally controlled coaxial extrusion tip with output diameters of 1200µm for external material and 400µm for internal material.

2. Enhance the reliability of the coaxial fiber production by optimising flow parameters through the coaxial tip, producing average coaxial axis offsets lower than the literature value of 22%.

3. Improve the range of materials to be printed coaxially. Previous work had allowed lower temperature structures to be created; this work aims to achieve temperatures up to 275^{o}C. This will enhance the range of materials for coaxial printing to reach the many commercial materials available in FDM systems.

4. Produce a secondary coaxial extrusion tip to facilitate the inclusion of pre-formed fibers into FDM processes.

5. Print multi-layer coaxially coated conductive pathways.

1.8 THESIS LAYOUT

This thesis is structured to provide a section by section view of the progressive work done to achieve the research objectives stated previously. Chapter 2 focuses on the experimental design for the coaxial nozzles, outlining the design considerations and fixed parameters for creating a customised FDM system. In doing so, the internal geometry of two coaxial hot-ends is explored and optimised via simulations, increasing the concentricity of the coaxial flow; this process is completed for both coaxial fibre deposition and coaxial coating deposition.

Chapter 3 outlines the fabrication methods used to realise the designs created in chapter two. In the process, the print resolution and structural properties of components produced by FDM and SLM systems is discussed. Comparing the dimensional accuracy of the physical models to their CAD counterparts and exploring the usefulness of post-fabrication processing to reduce surface roughness.

Chapter 4 details the results obtained from the successful construction and operation of the device designed. Discussing the methods used to test the system and its accuracy in producing coaxial structures as well as their characteristics. Subsequently, examining methods to improve the concentricity of multi-layer coaxial structures and discussing external parameters which will affect the print resolution.

Chapter 5 presents thesis conclusions and directions for future work. Noting specifically the high level of concentricity obtained for the coaxial structures as well as potential measures to improve the production of multi-layer objects.

2 EXPERIMENTAL DESIGN

In this section, the existing framework of the FDM system is outlined, the associated design considerations and fixed parameters in creating a coaxial three-dimensional printing device are presented. To this aim, the internal geometry is explored and optimised to obtain a uniform flow through two complex coaxial nozzle designs.

2.1 FUSED DEPOSITION MODELLING OVERVIEW

In assessing the requirements for the design of a coaxial FDM system, it is essential to first evaluate the core components of an FDM system. The design process stems from the appropriation and reconfiguration of a gantry style FDM system. Therefore, an audit is performed on the existing structure, identifying which of the essential components can be reappropriated or reused in the modified system and which must be discarded.

The system to be modified is a typical multi-material FDM printer (Figure 2.1 a) & b)); this device allows three materials to be used sequentially in any print. It offers a three extruder system, stable external structure and large build volume, making it a suitable candidate for the proposed improvements. Table 2.1 provides a clear layout of the essential components of an FDM system and the corresponding parts on the machine to be modified.

Table 2.1 - FDM Requirements and Stock Multi-Material FDM Components

FDM Requirement	**Existing Component**
Support Structure: A series of columns or beams arranged in a manner to permit movement of a hot-end along the X, Y and Z axes.	Well structured, rigid, gantry style support. Component will be reused.
X, Y and Z Axis Motors: Stepper motors mechanically drive movement of the hot-end along the associated axis.	NEMA 17 stepper motors control movement on all axes. A core component for FDM systems. Components will be reused.
Extruder: This component, usually a small stepper motor, is used to force the material feedstock into the hot-end. These are typically found either mounted above the hot-end or externally mounted on the support structure with the material transported via Teflon tubing to the hot-end.	Three NEMA 17 stepper motors are used with the triple head extrusion system. This design is common place amongst small FDM systems. Two NEMA 17 stepper motors will be reused, one will be reappropriated
Hot-end: A region which melts the feedstock material and reduces its diameter from 1.75 mm or 3 mm on the input, to 0.4mm on the output. This component requires a heating element and a sensor to provide feedback for thermal control.	Three hot-ends are in place in the BFB system, one linked to each extruder. Component will not be reused. Modified hot-end will be coaxial
Control System: A combination of a microcontroller, stepper driver boards and various additional electronic components which govern the commands sent to the printer via a pre-uploaded firmware.	Microcontroller and associated electronics to power six stepper motors and three hot-end heaters. No accessible firmware. Components will not be reused. Control system requires firmware modifications.
End-Stops: Sensors which are used to calibrate the position of the hot-end relative to the support structure and print bed prior to any printing	Three magnetic reed switches present in stock BFB Touch design, one for each axis. Components will not be reused. Magnetic switches replaced with mechanical leaf switches.
Print Bed: A flat surface on which the molten feedstock is extruded. The print bed may be heated or non-heated. Heating will improve the first layer adhesion which is imperative to the structure of the subsequent layers.	Current print bed is a composite rubber material and is prone to warping. Component will not be reused. Require sturdy print bed, modified for bed-levelling capabilities.

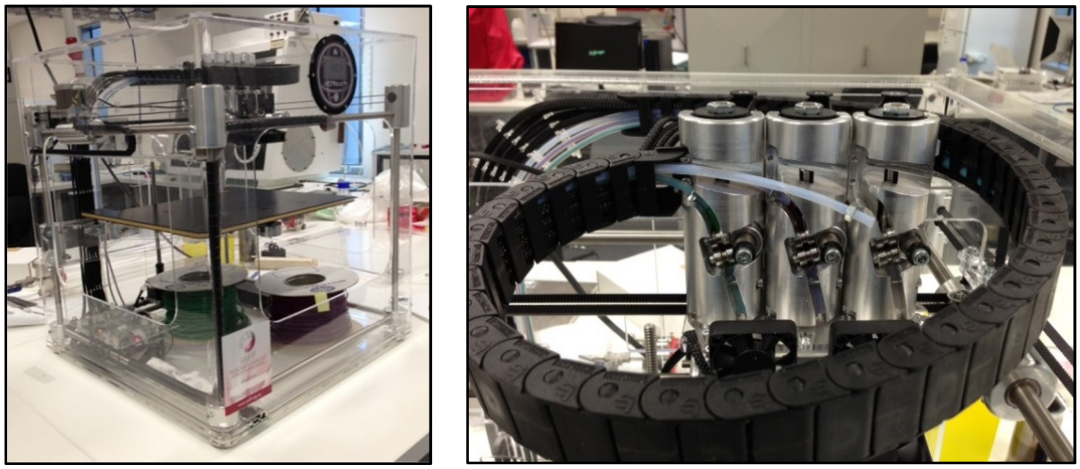

a) *b)*

Figure 2-1 - Stock FDM System for Modifications.

a) Overview of FDM System and Structure. b) Triple Head Extruder Configuration

2.2 Design Considerations

In Section 2.1, all crucial components have been identified which can be reused from the design of the stock device and those which must be replaced. This section examines the considerations associated with the components which are redesigned. These are split into either mechanical or electrical modifications, listing the components from Table 2.1 and then stating all relevant design constraints and the resultant solution.

2.2.1 Mechanical

The division between mechanical and electrical components is equally split when discussing additive fabrication processes; neither can function correctly without the other. In the mechanical partition of the components to be designed, the means of supplying the

thermoplastic material to the hot-end is examined. Detailing the previous design and using the decisions behind their operation to create an improved process. Subsequently, the coaxial nozzles to be designed are examined. Discussing the design requirements from a fluid dynamics and thermodynamics perspective, while also considering the method of fabrication and the restrictions it may enforce.

2.2.1.1 Feed Mechanism – Extruder

Due to the restrictions in the range of geometry which can be fabricated for the coaxial nozzle design, the feed mechanism must be oriented at a 45^{o} angle. This limits the potential configurations for the extruder position as new spatial constraints are now imposed. Most notably, the vertical volume which will be occupied, as the extruder design must not interfere with the external support structure when performing the pre-print calibration process. This involves the movement of the hot-end to the boundaries of the print volume as shown in Figure 2.2a. Finitely, it must remain 11mm and 17.5mm from the x and y origins respectively.

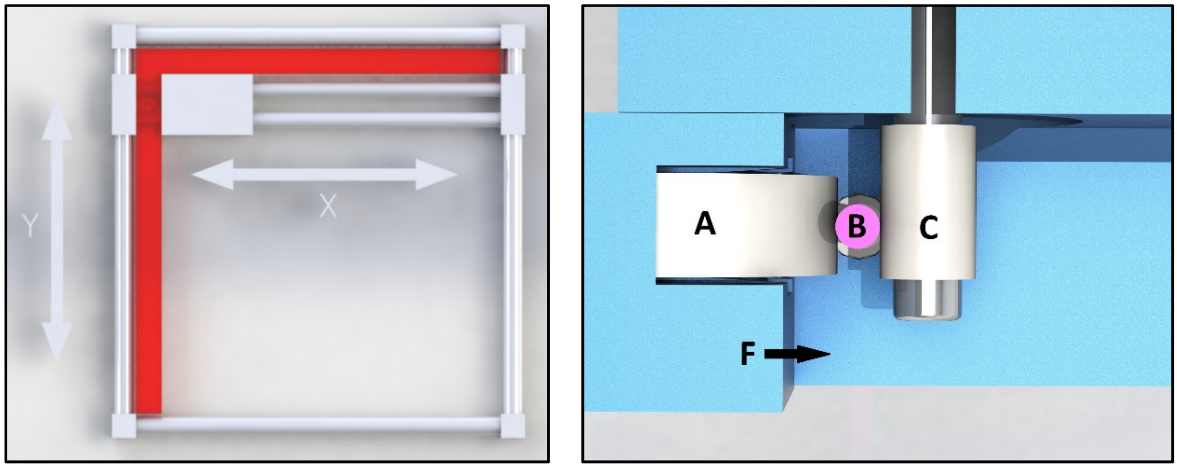

a) *b)*

Figure 2-2 – Mechanical Design and Restrictions for Frame and Extruder.

a) Dimensional Constraint for Homing. b) Top-Down View: Improved Geared Extruder Design

The stock design for the extrusion system relied on a long, screw-driven mechanism powered by a NEMA 17 stepper motor; this mechanism is both excessively heavy, and spatially inefficient. This draws motivation to create a geared drive extrusion method where the contact between the material and the drive mechanism is minimal, thus reducing the physical dimensions, creating an extruder similar to many commercial designs. Furthermore, the additional weight imposed by the preceding design instigated additional load on the X and Y axis motors, reducing the potential speed of hot-end movement.

Figure 2.2 b shows the geared extrusion design concept. This system works by applying a force (F) to a bearing housing (A) which causes a feedstock (B) to make contact with a toothed gear (C). The toothed gear then grips the feedstock and propels it in the desired direction. The bearing acts to reduce undesirable friction, while the contact force, F, is adjustable as a result of a spring mechanism shown in Figure 2.3.

An additional constraint of the extruder design is the requirement to supply feedstock for two materials simultaneously. Given the nature of the coaxial fibre nozzle design, which is defined in the following section, two materials must be supplied at differing rates. This implies that two extrusion systems are required and there must be independent control over the speed of each. This dual extruder necessity, coupled with the required orientation of 45^{o} or greater from the horizontal, eliminates the possibility of allowing a single stepper motor from supplying both feedstock materials.

As this system aims to accommodate a large variety of materials, the feed mechanism must be designed accordingly. A known issue exists in the attempted extrusion of flexible filaments via long Polytetrafluoroethylene (PTFE) material supply tubes. This process typically encounters material clogging in long, winding tubing systems. As such, the desired design will minimise the supply tubing length while keeping it linear, minimising the likelihood of material blocking occurring.

Resultant Design

With the above considerations accounted for, the optimum feed mechanism has been designed as shown in Figure 2.3. This component is to be oriented at a 45^{o} angle for ease in the design process for the coaxial nozzles, while also enabling a short, linear supply tube to be fitted, allowing for ease of printing flexible filaments. The feed mechanism fits a NEMA 17 stepper motors with MK8 geared drive systems within the spatial constraints applied by the pre-print calibration process. With this design fabricated from ABS, it proves to be significantly lighter than its predecessor, enabling faster hot-end movement.

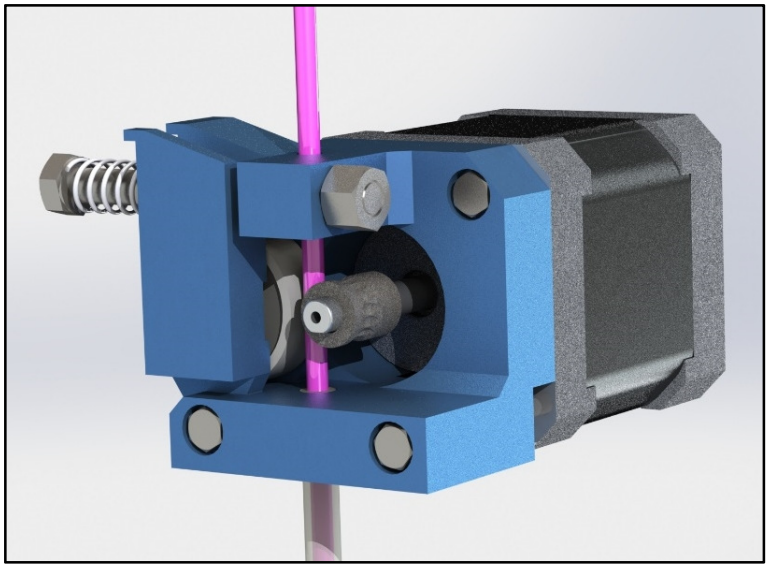

Figure 2-3 - CAD Model - Feed Mechanism

This concept accepts both standard diameter filaments (1.75mm and 3mm) due to the adjustable tensioning mechanism, allowing for further integration of materials into the produced coaxial structures. While this design is to be produced by a FDM system and is detailed in Section 3.1, manufacturing drawings are presented in Appendix C.

2.2.1.2 Coaxial Fibre Extrusion – Design and CFD Simulations

To create a system which produces coaxial flow, the external material must envelope the passage of the internal material before allowing the two fluids to interface. Accurately predicting the fluid flow for the given input materials will optimise the concentricity of the printed products; a key milestone for this project. While other factors such as heat chamber temperature and layer thickness will influence the concentricity of the coaxial fibres produced, they are parameters which can be more easily controlled in-situ; fluid flow optimisation however, must be designed in advance. This section focuses on the design constraints imposed on producing a coaxial hot-end and the process of creating its internal geometrical curvature. To optimize the flow performance of the coaxial nozzle design, several nozzles were created using Solidworks to generate three-dimensional models, and ANSYS CFX used to compute thermal and flow simulations on the concept designs.

ANSYS CFX has been selected as the ideal software to complete simulations due to its extensive history for use in fluid simulations as well as its ability to incorporate multi-physics approaches. This is essential for the simulations to be conducted as the coaxial hot-end will be affected by both thermal conduction and fluid flow. This CFD simulation allows for desired material characteristics to be selected for the fluid and solid components of the CAD model, while also imposing the associated melting temperatures for the feedstock materials. By doing so, it is possible to predict the thermal conduction of the fluid material as well as its behaviour navigating the complex internal geometry of the coaxial nozzle.

The coaxial tip models varied in the external fluid pathway only and were designed systematically as governed by the following conditions:

1. Straight pathway for external fluid (Figure 2.4)

2. Create 5° angular cross-sections which are perpendicular to the external fluid pathway and span a total of 50°. Progressively reduce the cross-sectional area of the external fluid pathway by an equal amount until the internal fluid pathway is concentric within the external pathway.
3. Following the external fluid pathway and using the 5° method from condition #2, progressively expand the cross-sectional area in an elliptical form until the internal fluid pathway has been enveloped by the external, but is not yet concentric
4. Identical methodology as condition #3 though the cross-sections were based on the internal fluid pathway rather than the external (Figure 2.6a and b)

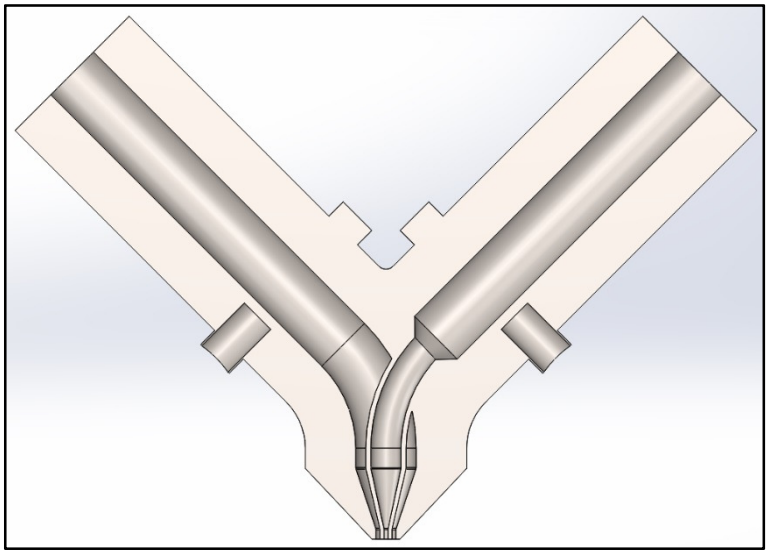

Figure 2-4 - Cross-Section of Standard Coaxial Nozzle Design

An initial CAD model was created and shown in Figure 2.4 and a fluid simulation has been performed using ANSYS CFX. The results identified an unbalanced velocity distribution and a region of static flow. This placed a strong emphasis on equalising the velocity distribution as the two fluid channels become concentric and minimising static flow where possible. While it is likely that these flow conditions will change depending on the material being processed, for the nature of this work, the primary material used will be PLA. This material has been selected due to its biocompatible nature. This will enable the system to produce scaffold structures with biological potential for medical applications; the target audience for this device.

Depending on the viscosity of the material to be printed and the speeds at which they will be processed, areas of static flow occur to some extent in all geometries similar to that shown in Figure 2.4. This region is found as the internal nozzle enters into the external chamber; the protruding structure obstructs flow and creates a surface shielded from the direction of fluid flow. As a result, a solid aerofoil shape has been modelled around the internal nozzle in an attempt to minimise this occurrence and create a more uniform velocity distribution. The variation in static flow between original and aerofoil model for the initial design is shown in Figure 2.5 a and b, respectively. While a more obvious example indicating the impact of the aerofoil model by comparison to the original can be found in Figure 2.10 a and b.

While the simulations aim to produce a more uniform pressure distribution and velocity, the ultimate goal is to achieve concentricity in the final print material. This is expected to be obtained by producing equal velocities for both the internal and external chambers. However, the merging of the materials outside of the nozzle may cause irregularities to appear in the print materials.

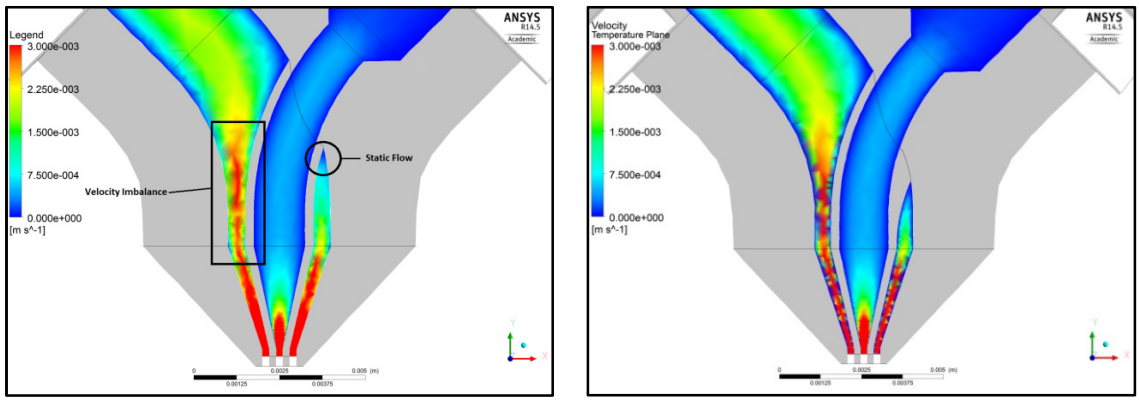

a) *b)*

Figure 2-5 - Initial Fluid Simulation.

a) Regions of Static Flow and Velocity Imbalance. b) The Impact of an Aerofoil Design on Velocity Imbalance and Static Flow

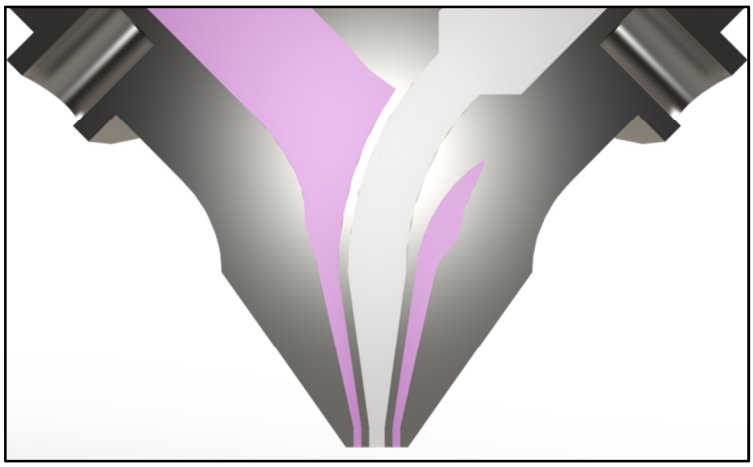

a)

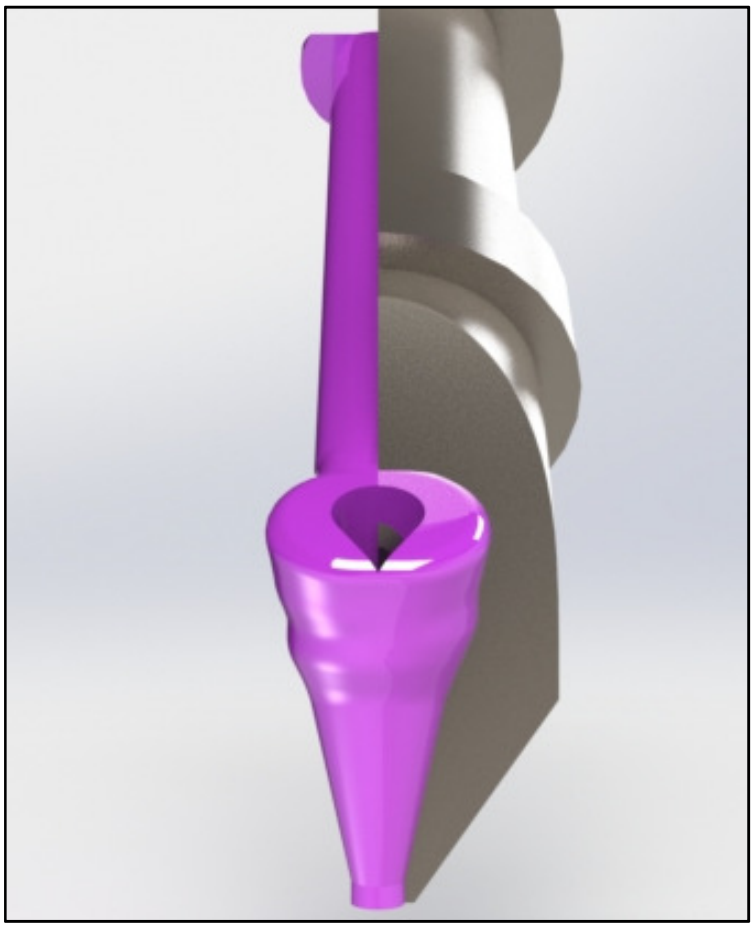

b)

Figure 2-6 – Fluid Pathways for Optimised Coaxial Nozzle Design – Condition 4

a) Cross Section Full View. b) Section View of Complex Geometry

The simulations have been completed under the following circumstances, assuming the most extreme thermal requirements, accommodating higher temperature materials. Let the internal material feedstock be ABS, the external material be PLA, and the body of the coaxial hot-end

be constructed from Ti6Al4V. The molar mass, density, specific heat capacity, dynamic viscosity and thermal conductivity for each material can be found in Appendix D. The heat chambers for external and internal materials are set to 468.15^{o}K and 533.15^{o}K, respectively; as these are typical printing temperatures for each material[67, 68]. Outlet pressure is assumed to be 101,325 Pa at an ambient temperature of 298.15^{o}K.

Material velocity for use in simulations has been determined from the output velocity of the stock multi-material FDM extrusion system. These calculations assume that the velocity for the external material is identical to that of the previous extruder design, with the internal material flow being determined from the nozzle tip dimensions shown in Figure 2.7. Velocity calculations are obtained as:

$$Velocity_{EXTERNAL} = 0.001\ (\frac{m}{s})$$

Let the external material have the same extrusion speed as the previous design.

$$Tip\ Area_{INTERNAL} = 0.125664\ (mm^2) \qquad Tip\ Area_{EXTERNAL} = 0.628319\ (mm^2)$$

$$EXTERNAL{:}INTERNAL\ Ratio = 5{:}1$$

Therefore, we can apply the output ratio to the external input speed to determine the ideal internal speed.

$$Velocity_{INTERNAL} = \frac{Velocity_{EXTERNAL}}{5} \qquad (2.1)$$

$$Velocity_{INTERNAL} = 0.0002\ (\frac{m}{s})$$

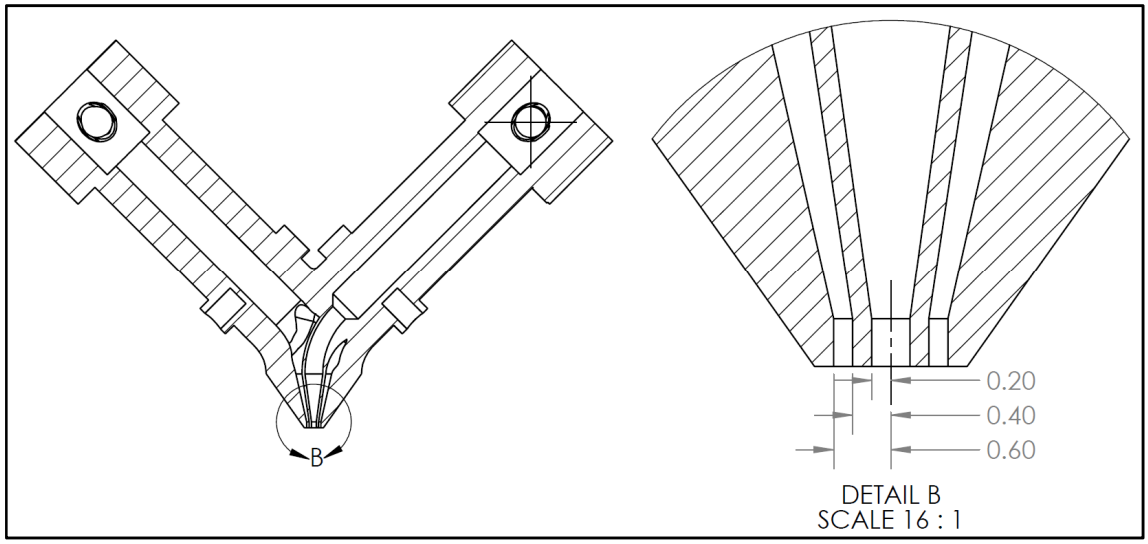

Figure 2-7 - Coaxial Nozzle Output Dimensions

All flow calculations have been completed using laminar conditions as calculated below:

$$Re = \frac{\rho v D}{\mu} \qquad (2.2)$$

Where

$Re = Reynolds\ number$

$(Re < 2300: laminar, 2300 < Re < 4000: transitional, Re > 4000: turbulent)$

$\rho = density\ \left(\frac{kg}{m^3}\right). PLA\ and\ ABS\ material\ values\ as\ per\ Appendix\ D.$

$v = velocity\ \left(\frac{m}{s}\right).\ 0 \leq v \leq 0.01$

$D = diameter\ (m). Largest\ diameter\ considered, 3mm.$

$\mu = viscosity\ (Pa.s). PLA\ and\ ABS\ material\ values\ as\ per\ Appendix\ D$

Figure 2.8 shows a plot of the Reynolds number for PLA and ABS within an optimum velocity range. This image clearly indicates that the flow will remain laminar for all velocities to be considered for this work.

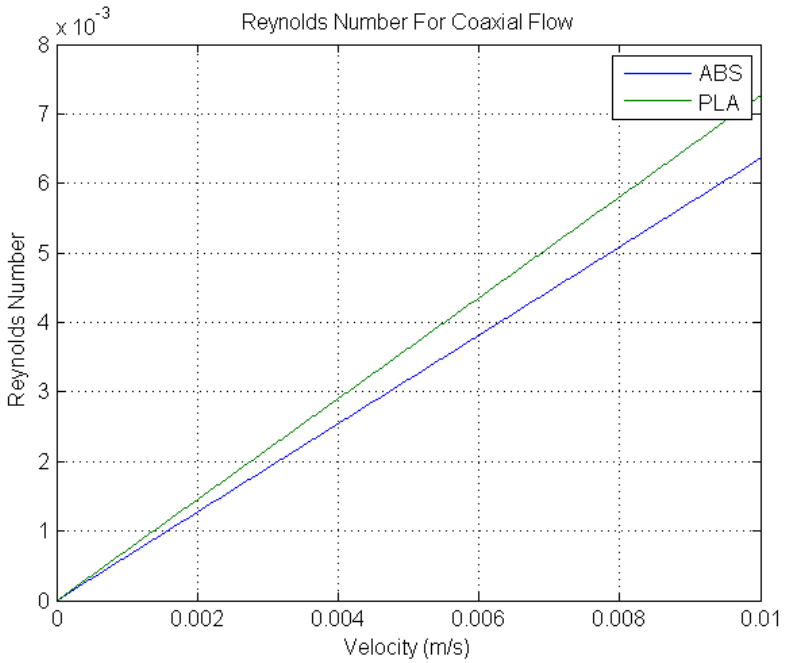

Figure 2-8 - Reynolds Number Plot

Using the defined parameters and the progressive design approach prioritising equal velocity profiles and minimising regions of static flow, the concept design shown in Figure 2.6 is finalised. The nozzle has input diameters of 3 mm for both internal and external materials and output diameters of 400µm and 1200µm for the internal and external materials, respectively. Figure 2.9 shows the impact of localised heating and the heat distribution beyond the heating coils for both the nozzle structure and the fluid flow thermal conductivity.

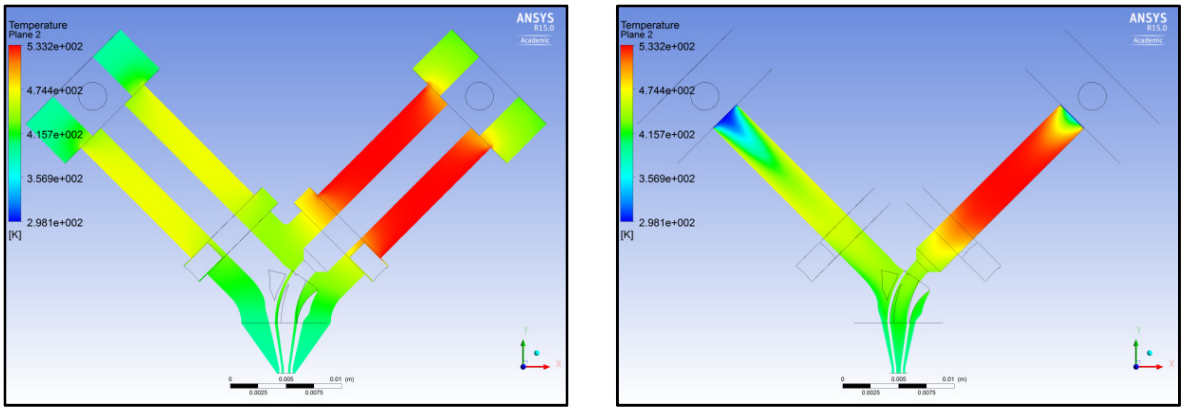

a) *b)*

Figure 2-9 - Coaxial Nozzle Thermal Simulations using PLA and ABS.

a) Titanium Alloy Body Thermal Conduction. b) Fluid Thermal Conductivity

This simulation has been conducted assuming that PLA and ABS are used for the external and internal materials, respectively. While this scenario will not be the initial range for testing, the simulations have been included as a worst-case-scenario for inducing a thermal gradient across the coaxial tip. The area of primary concern lies within the coaxial region of the tip design, determining what effect the thermal gradient will have on the print temperature of the lower melting point material (in this scenario, the PLA).

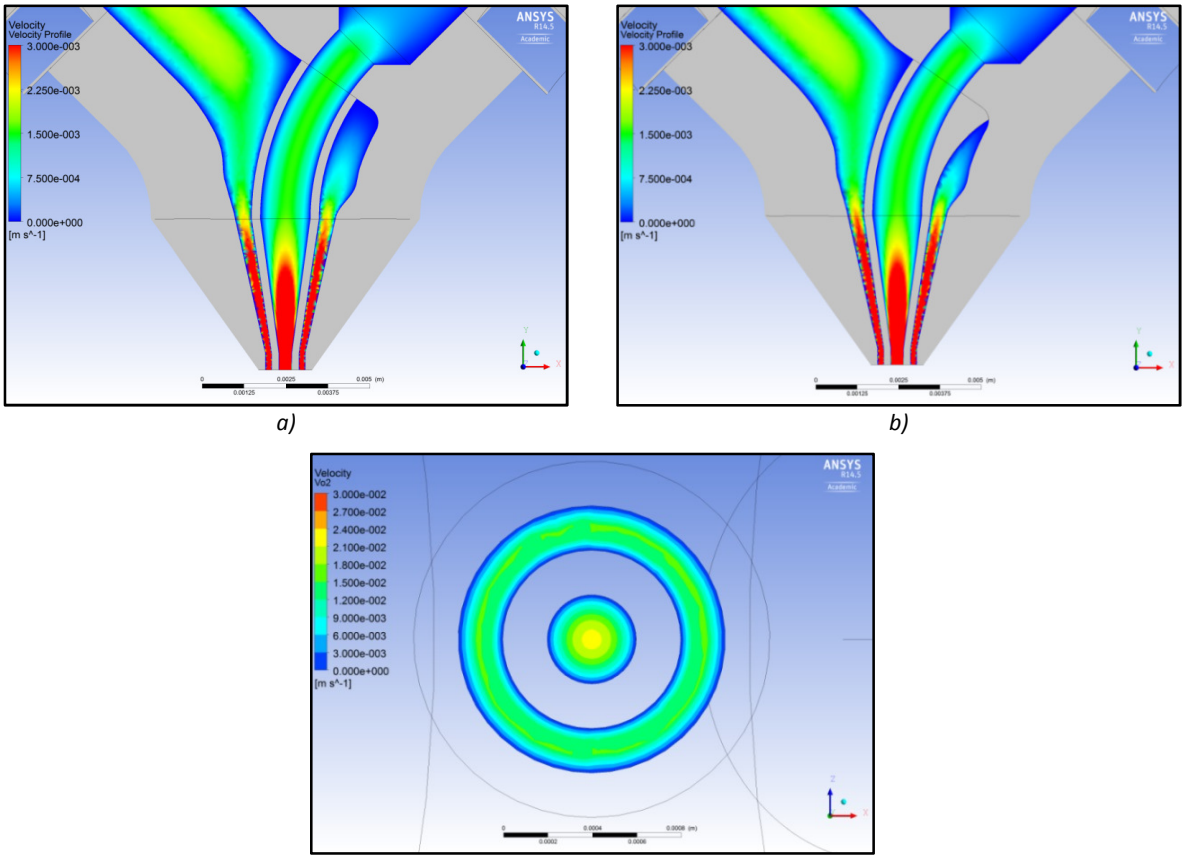

a) *b)*

c)

Figure 2-10 - Coaxial Fluid Velocity Simulations.

a) Cross-Sectional Velocity Profile without Aerofoil. b) Cross-Sectional Velocity Profile with Aerofoil c) Bottom-Up Velocity Profile of Coaxial Tip

Figure 2.10 indicates a fulfilled design criteria as stated previously, showing an equal velocity profile for the external fluid about the central axis. Concurrently, the simulation indicates that the aerofoil design for the protruding internal material minimises the likelihood for the occurrence of regions of static flow.

While Figure 2.9 shows the extreme case for coaxial printing and the presence of a thermal gradient, Figure 2.11 shows the ideal initial test printing scenario, PLA being used for both internal and external materials. The simulations show the impact of symmetrical heating as thermal conduction passes through the titanium structure (Figure 2.11a) and the heat sets the temperature for material extrusion. Figure 2.11b shows a potentially problematic issue, due to the decreased flow rate; the internal material reaches a higher temperature prior to extrusion, thereby lowering its viscosity. This may cause issues in concentricity of the printing process as one material will flow more freely than the other.

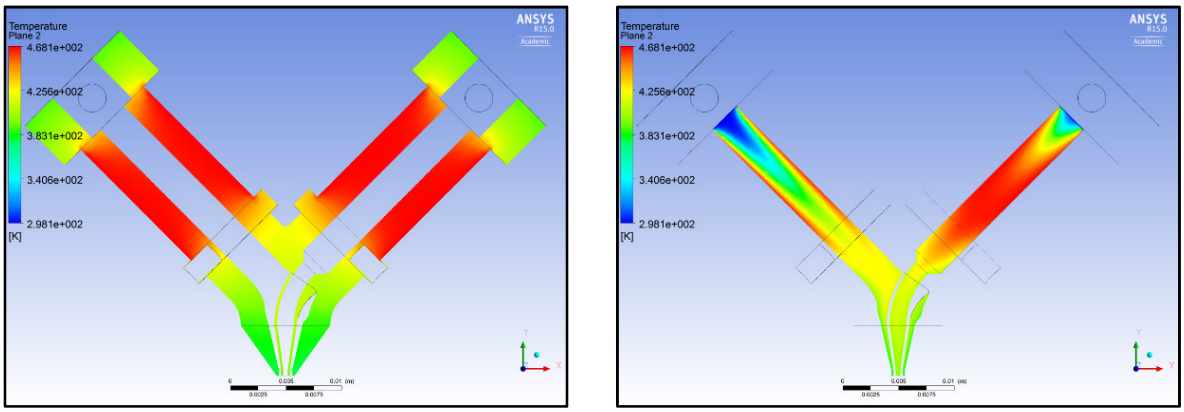

a) *b)*

Figure 2-11 - Coaxial Nozzle Thermal Simulations using PLA and PLA.

a) Titanium Alloy Body Thermal Conduction. b) Fluid Thermal Conductivity

2.2.1.3 Coaxial Coating Extrusion – Design and CFD Simulations

The coaxial coating process aims to modify the previous coaxial nozzle design in subsection 2.2.1.2 to allow for the inclusion of an external pre-formed material to be implemented in an FDM printing process. A unique feature of coaxial printing is the potential to print conductive core materials surrounded by insulating ones. Unfortunately, high quality conductive thermoplastic filaments are not yet common place; the design discussed in this section will

allow for a pre-formed conductive material to be incorporated into the coaxial FDM printing process. The optimum design requires only one method of extrusion for the sheath material, and allowing the internal material to be passively drawn by entrainment. As such, the internal tip must be recessed within the external tip (Figure 2.12), allowing the sheath material space to envelop the core, adhere to it, and draw it out of the tip.

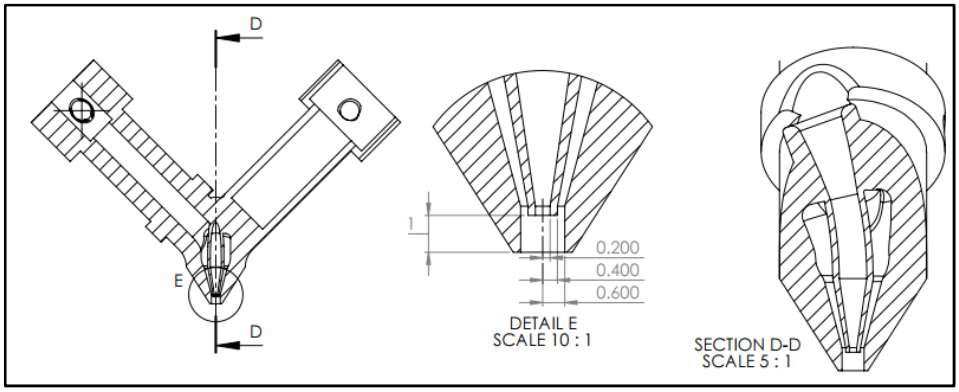

Figure 2-12 - Coaxial Coating Nozzle Cross Section: Internal Geometry, Output Dimensions and Entrainment Channel

Using the design process to obtain symmetrical velocity distributions about the internal tip and minimise regions of static flow entailed in subsection 2.2.1.2, the concept in Figure 2.12 is created. For ease of core material drawing, the entrainment channel is designed to be as linear as possible, while considering the materials pathway. Given the spool position for the pre-formed material must be located above the coaxial tip, the core material must pass through the support structure for the extruder housing. This constrains the linearity of the entrainment channel, indicating it must be slightly angled.

Additionally, the coaxial coating nozzle has been designed to accommodate 1.75mm filaments, while having identical output dimensions to the coaxial fibre extrusion design. Figure 2.12 shows a pathway for the external material to be heated on the left hand side, though it shows a hollow section on the right hand side of the tip. This has been done in an attempt to minimise what is expected to be a large heat sink, drawing away heat from the sheath material heat chamber. To determine the heat loss due to the unheated side of the tip, thermal

simulations have been conducted using ANSYS CFX. Figure 2.13 shows thermal conductivity using PLA as the external material and indicates the presence of a heat sink in the hollowed side of the coaxial tip. The simulation suggests that this could lower the PLA temperature in the tip from 468°K to 340°K, well below its melting temperature of approximately 420°K. This ultimately implies that the designed tip configuration would fail to perform as required and would cause solidifications of PLA within the tip itself.

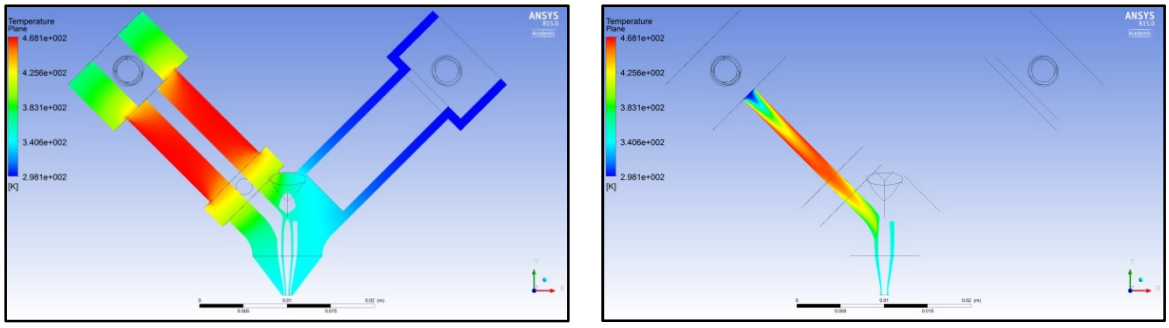

a) *b)*

Figure 2-13 - Coaxial Nozzle Thermal Simulations for PLA with Single Heat Source

a) Titanium Alloy Body Thermal Conduction. b) Fluid Thermal Conductivity

To combat the heat loss introduced by the hollowed section of the coaxial tip, an additional heat source may be included. This would be localised around the existing unwanted heat sink and prevent excessive thermal dissipation into the environment. To determine the effectiveness of this measure, additional thermal simulations were conducted, setting the new heat source to mirror the temperature of the external materials heat chamber. Figure 2.14 shows the impact of the additional heat source on the sheath material at the tip by comparison to its heat chamber temperature. The simulation suggests that this tip configuration could lower the PLA temperature in the tip from 468°K to 430°K. This indicates that the material should still be in its liquid form as it reaches the tip outlet, allowing it to be printed.

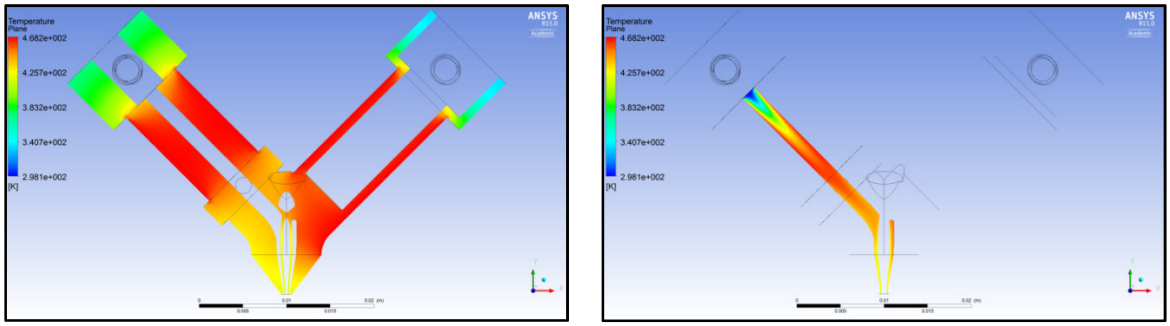

a) *b)*

Figure 2-14 - Coaxial Nozzle Thermal Simulations for PLA with Secondary Heat Source.

a) Titanium Alloy Body Thermal Conduction. b) Fluid Thermal Conductivity

With the configuration for coaxial heating identified, Figure 2.15 clarifies the designed passive extrusion process of entrainment. The molten polymer will fill the cavity and progress to envelope the core material, cooling around it, binding to it and extruding it through the tip as shown in Figure 2.15b. While it is expected that this process will work as desired, it is expected that there will be variability in the effectiveness of the adhesion process. The key factors likely to impact the adhesion are print temperature, rate of external cooling, diameter of pre-formed fibre as well as the surface properties of both the core material and the thermoplastic.

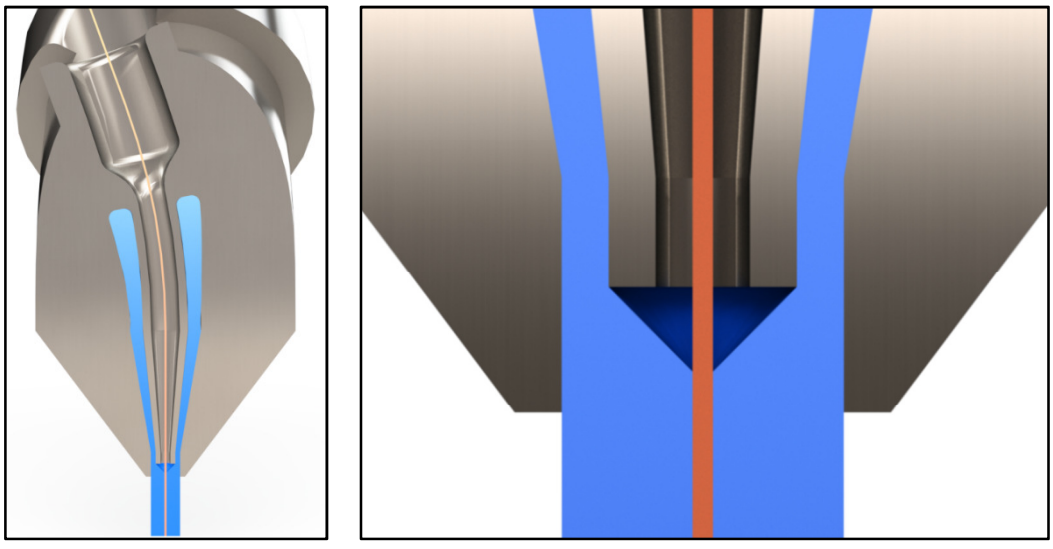

a) *b)*

Figure 2-15- Process of Entrainment for the Core Material.

a) Cross-Sectional View of Pre-formed Fibre Pathway and Entrainment Setup. b) Close-up of Cross-Sectional View of Entrainment Process, Showing Internal Nozzle Recessed Inside External Chamber, Forcing Thermal Expansion and Fluid Flow to Contact the Pre-formed Material Core.

2.2.2 Electrical

Continuing from subsection 2.2.1, the electronic components necessary to allow the device to operate as required are examined. These include the microcontroller, stepper motor drivers, microcontroller shield, microswitches and thermistors. Successively, the modifications which must be made to firmware to allow the FDM system to extrude two materials simultaneously and at differing rates have been determined.

2.2.2.1 Electronics

To control the device's thermal regulation and movement, a control system must be implemented. This must manage the movement of the hot-end in the X, Y and Z-axes while providing a simultaneous and independent control of two extruders as well as two heat chambers.

The proposed solution involves the use of an Arduino Mega 2560 microcontroller with customised firmware to govern the commands for the FDM system, a RepRap Arduino Mega Pololu Shield (RAMPS 1.4) with Pololu A4988 stepper motor drivers and SPDT microswitches replacing the previous reed switches. The electronics are powered by a 12V, 5A power supply, and the microcontroller is controlled through a USB connection to a computer using Pronterface control software. The schematics and datasheets for these components can be found in Appendix B

Stepper Motor Control

The resolution of any additive fabrication device is governed by the accuracy of the movement of the motors, specifically, the smallest z-axis step permissible. In the scenario of the coaxial FDM, all stepper motors have $1/16^{th}$ stepping enabled through the A4988 stepper motor drivers. This implies that the smallest movement each motor can make is 0.1125^{o} (NEMA 17 operating at 1.8^{o} per step), though this degree of movement must be translated to its corresponding movement in a particular direction.

Both the X and Y-axis stepper motors drive a pulley and belt system to create movement. The pulley has a pitch of 2 mm and 16 teeth, giving an outside diameter of 10.18 mm. Determining the minimum movement along the x and y axes requires the translation of the motors rotation into a linear motion. This is done by considering the smallest rotational movement the stepper can perform (0.1125^{o}) and its resultant linear movement. Resulting in a minimum movement distance along both the x and y axes of 10 µm.

The Z-axis stepper motor drives a threaded shaft via a coupling. The shaft has a pitch of 1.5mm and is attached to the substrate through an open-ended internally threaded chamber. This chamber attaches the two components via a rigid structure and two linear bearings. Using the pitch of 1.5mm and the minimum permissible motor rotation, the z axis resolution is determined to be 0.46 µm.

The designed extrusion system employs a geared drive system with a contact radius of 3.5mm. This dimension coupled with the minimum permissible rotation for the stepper motors indicates that the minimum linear movement translates to 6.8 µm.

While the resolutions for the Z-axis and the extrusion system appear small, they are rarely used at this minimal setting. Translating these movements requires overcoming the associated initial load to the motor. Additionally, movements of this magnitude are not likely to be useful for the extrusion system as it typically accepts millimetre sized movement commands. This scenario holds true for the Z-axis movement also; the movement commands sent to typically range from 0.2-0.6 mm depending on quality and speed of production. However, this fine z resolution does allow a greater accuracy in positioning the substrate when performing these larger movements. Simultaneously, these factors allow for an enhanced reliability and repeatability in producing coaxial structures.

Thermal Control

Correct thermal control of the device is crucial to maximising the number of materials for potential use. Thus, the operating temperature range should be maximised, reaching temperatures of 275 °C. To do so, a heat source must be implemented with a thermal sensor, giving the ability to create a feedback loop. The temperature will increase through the process of Joule heating, whereby a coil of conductive wire generates heat as a result of the current passing through it.

The heating coil is composed of a Nichrome wire (NiCr) with a resistance of 26.4 (Ω/m). Given that the power supply to the electronics is rated to 5 Amps, a maximum consumption is calculated to determine the required resistance for the heating coils. To reach a temperature of 275°C, a thermal sensor must be used to measure the temperature up to this point. As such, a 204GT-2 thermistor has been selected for its high temperature range and exceptional accuracy in measurement. The data sheet for this component can be found in Appendix B

Each stepper motor is capable of drawing 0.2 Amps of current while operating, though by the governing control system, not all stepper motors may be operating at the same instance. X and Y-axis motors will not operate while the Z-axis motor is functioning, and vice versa. Therefore, the maximum current drawn is when both Y-axis motors, both extruders and the X-axis stepper motor are operational. Drawing a cumulative current of 1 Amp, this value will be increased by 0.12 Amps for the digital output signals sent to the three microswitches. Therefore, each heating coil is designed to draw 1.5 Amps to prevent issues of overdrawing current from the 5 Amp supply. The current drawn will be fixed by specifying the length of the heating coil to be 0.3 m (8 ohms), allowing the cumulative current drawn to reach 4.12 Amps, allowing a margin of safety.

While time to heat the hot-end is controlled by a proportional-integral-derivative (PID) controller implemented in the microcontroller firmware, the rate at which heat conducts into the feedstock may create a limiting factor. Indicating that a flow-rate will exist at which point the heated material will no longer reach its required temperature for printing, as it has not remained within the heat chamber for a sufficient duration. The flow-rate used for the simulation data shown in Figure 2.10 b) is used as the limiting flow value.

Beyond this, the nature of this device demands that each heat chamber must be independently temperature regulated. As a result, it is expected that large thermal gradients between heat chambers will have a negative influence on the chamber with the lower target temperature. Unwanted heat contamination will reach this material and will not be controlled within the device. Therefore, consideration must be given when printing two materials with vastly different melting points.

2.2.2.2 Microcontroller Firmware

To control the actions of the FDM system, firmware must be uploaded to the Arduino Mega 2560. The volume of processing which must occur to correctly govern the control of an additive fabrication device is excessive; due to this, a new program has not been created. Rather, a modification of existing open-source firmware has been implemented. Marlin, as the code is known, is the selected firmware to modify. It offers compatibility with the selected electronic components and has the ability to be altered in the Arduino IDE. Due to the size of the firmware, code modifications have not been included in this thesis.

Modifications

The primary modification to be made is to enable two extruders to be active simultaneously, though at differing rates. This concept differs from commercially available extrusion systems which allow for mutually exclusive extruder activation. The required firmware modifications require extruder 1 to extruder 2 to operate at a ratio of 5:1, as discussed in the flow rate calculations in subsection 2.2.1.2. This functionality has been implemented by assigning a third extruder setting to a two extruder system. This additional setting will activate extruder 2 once per five steps of extruder 1. By fixing the ratio of speed for the extruders, a degree of flexibility has been removed from the system, as any dimensional changes in coaxial nozzle design will require a modification of the firmware.

Additional modifications have been made to the firmware notably in the pin configuration for the associated microcontroller. The RAMPS has two rows of header pins for the Z-axis motor, implying it can be used to drive two Z-axis stepper motors; the stock FDM system has two Y-axis stepper motors. As a result, the pin configuration for the Z and Y-axes has been swapped. As the current system utilises two Y-axis motors drive in opposing directions to one another,

their wiring too, must be altered. This allows the pin configuration and associated signals to remain the same, though the driving direction of the motor is swapped.

Subsequent modifications have been made to further enhance the reliability and repeatability of the FDM system. An auto-levelling system has been implemented to allow the print head to account for small discrepancies in elevation across the substrate. This process is completed by probing the print bed at three points and developing a new topographical map for the bed elevation. These probe points are linked by the assumption that the substrate will be flat and that the contact points are linearly related. This process allows for z-axis correction when printing, allowing for more accurate layer resolutions

2.3 GENERAL DESIGN

In addition to the modifications made in Section 2.2, several other supplementary design changes have been made to the FDM system (technical drawings for all general design components can be found in Appendix C). These include:

- Feed mechanism housing and hot-end stage. This component houses the two feed mechanisms and orients them at the required 45^{o}. It is designed to act as the moving stage and fits into the physical constraints of the previous hot-end stage. The housing also accommodates the insertion of PEEK collars and allows electrical wiring to pass to the hot-end.
- Polyether ether ketone (PEEK) collars. As the coaxial hot-end is designed to reach temperatures of $275^{o}C$, it must be thermally insulated from the surround support structure. The PEEK collars slide inside a cavity within the feed-mechanism housing, and allow the coaxial nozzle to be encapsulated in an insulating material.

- Microswitch mounting brackets. By removing the previous reed switches from the design, new mounting brackets must be created to allow for the fixation of these new components. This has been done by reappropriating the mounting points for the magnetic switches, allowing the microswitches to be positioned in the desired locations.
- Perspex print bed. The previous bed has been redesigned and replaced with 10mm thick Perspex. The new component maximises print tray area without causing warping while also reducing z-axis load.
- Z-axis motor coupling. The previous Z-axis motor was a NEMA 23 stepper motor. This component proved to draw a greater current than was permissible through the A4988 stepper motor driver. As such, the stepper motor was replaced with a NEMA17, requiring a redesign of a shaft coupling between the motor shaft and the screw mechanism. This smaller motor was able to be used due to the new Perspex print bed weighing significantly less than its predecessor.

3 COMPONENT FABRICATION

This section outlines the fabrication methods used for realising the designs created in Chapter 2. Specifically, it discusses the print resolution and structural properties resulting from FDM and SLM processes used; compares the dimensional accuracy of the fabricated components to their CAD counterparts and explores the effect of post-fabrication processing on the reduction of surface roughness.

3.1 FUSED DEPOSITION MODELLING - MECHANICAL STRUCTURES

Additive fabrication systems offer the ability to realise complex structures which would be otherwise impossible to manufacture using traditional methods. They offer rapid production with a variety of materials, making them an ideal solution for quick, complex designs. To take advantage of these abilities, several of the designed components were fabricated using the UPrint Plus system.

This device enables the production of objects with a minimum layer thickness of 254µm, while providing a variety of material fill density options. This infill density allows the printed structure to tolerate more force at the expense of increased object weight. All components manufactured through this method have been created with the minimum layer thickness and at a high density infill.

The feed mechanism, feed mechanism housing, microswitch brackets and shaft coupling have been created through this FDM system. Figure 3.1 shows the components produced via this method.

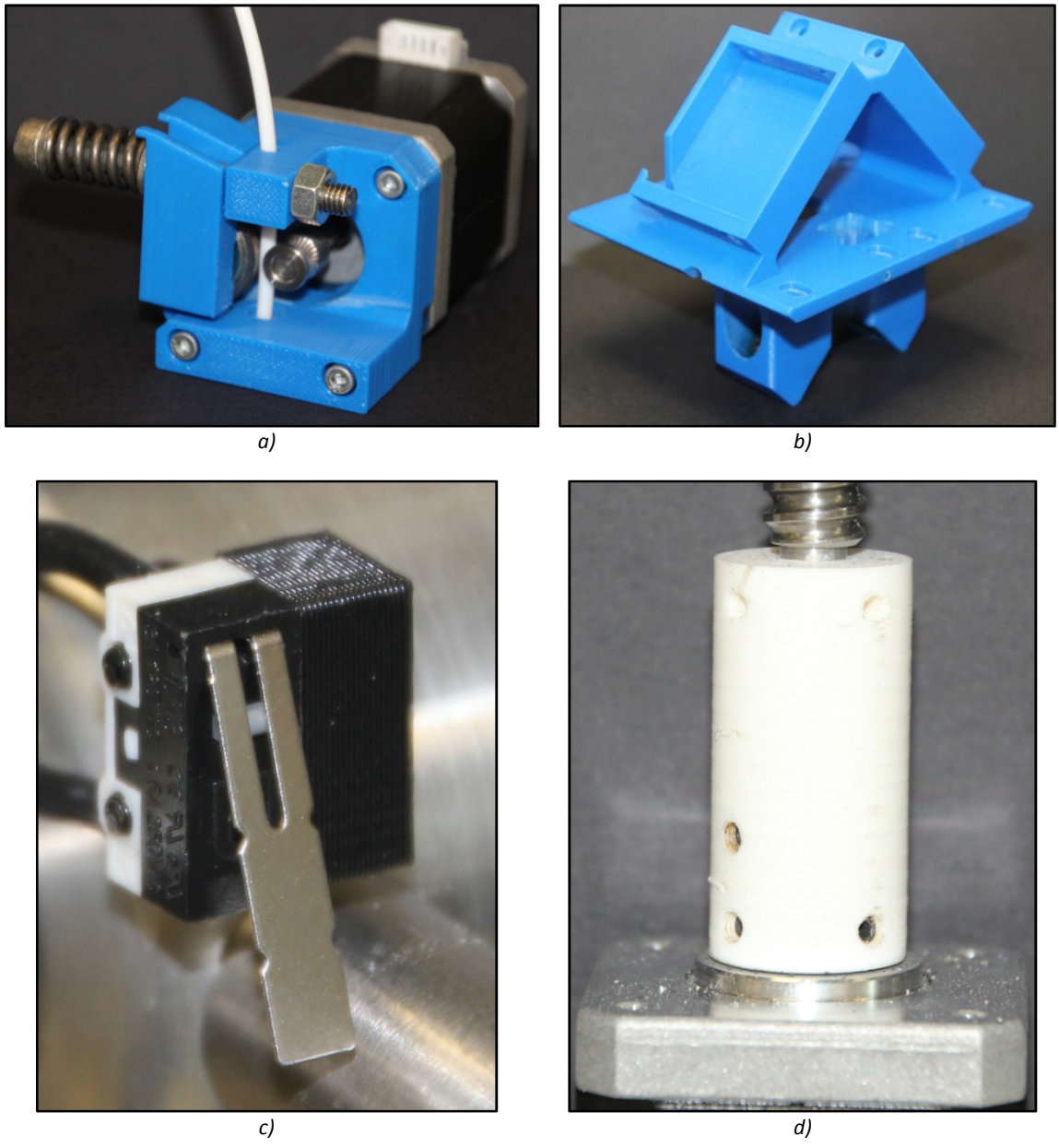

a) *b)*

c) *d)*

Figure 3-1 - Fused Deposition Modelling of Mechanical Structures.

a) Feed Mechanism. b) Feed Mechanism Housing. c) Microswitch Mounting Bracket. d) Shaft Coupling

3.2 Selective Laser Melting – Coaxial Nozzle Fabrication

This work uses the Realizer SLM 50 system, producing components out of a titanium alloy (Ti6Al4V). The process offers 25µm layer resolutions with a minimum feature size of approximately 150µm, though this may vary depending on the material powder properties. While this process melts the powder in a specified pattern, small amounts of neighbouring powder also loosely adhere during the process. Leaving a finish with a varying surface roughness, with the titanium powder used, these adhesions reach sizes of 65µm. Excessive surface roughness is detrimental to obtaining optimum coaxial flow. This issue is addressed in Section 3.4. Figure 3.2 shows adhesions in the coaxial tip.

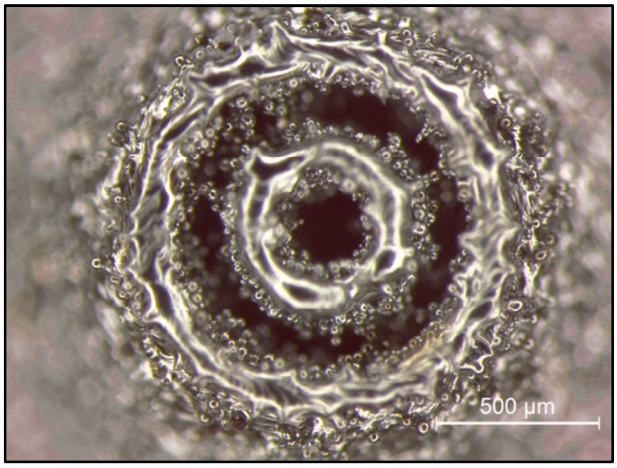

Figure 3-2 – Titanium Particle Adhesions Formed within the Internal and External Material Chambers

Due to the complex internal geometry of the coaxial nozzle, this component has been oriented in such a way to minimise the requirements of any internal support structure during the build process. Additionally, due to the height of the nozzle (both coaxial fibre and coaxial coating nozzles exhibit identical external dimensions), 32.6mm, and its narrow design of 12mm, several supporting beams have been included to reduce the likelihood of part deformation during fabrication. The resultant structures and the support associated are shown in Figure 3.3.

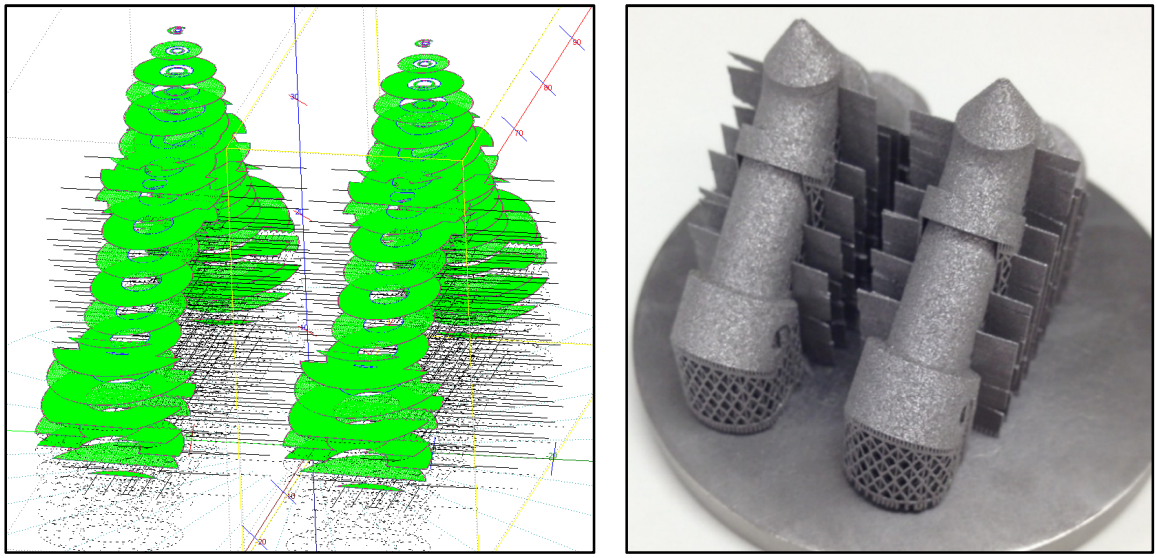

a) *b)*

Figure 3-3 - SLM Fabrication Process for Production of Ti6Al4V Coaxial Nozzle.

a) Sliced Data sent to SLM System. b) Resultant Coaxial Nozzles from SLM

The designed coaxial nozzle model includes two threaded M3 holes which are shown in Figure 3.3 b). This threaded feature must be physically present in the CAD model to allow for the inclusion of threaded channels. Previous attempts produced the component without the physical thread being modelled, requiring the thread to be tapped into the titanium alloy. This process proved difficult and the introduction of a guide channel for the tool to follow was beneficial. Due to the orientation of the component during fabrication, this newly formed thread must be correctly supported. The support must provide structural stability during the build, but minimising the contact area, making it easy to remove.

3.3 Dimensional Accuracy - Selective Laser Melting

Surface roughness has the potential to play an influential factor on obtaining optimised flow conditions similar to those simulated in subsection 2.2.1.2. The maximum surface roughness for the coaxial nozzle is expected to be $\leqslant$65µm, a value which is acceptable amongst a

majority of applications. However, obstructions of this magnitude may be detrimental to obtaining the simulated fluid flow. The presence of maximum surface roughness adhesions may cause issues in the finer dimensions of the nozzle; specifically, in the narrowed coaxial regions of the tip, where the designed gap is limited to 200µm.

The primary concern is that these adhesions will draw additional heat during the build process and create a merged structure, resulting in a blockage. To determine the magnitude of these adhesions, microscopic analysis is used to examine a cross-section of a fabricated hot-end. This tip is assumed to be indicative of the SLM process and used to identify potential issues in flow and also in decreasing the nozzle output dimensions for future work with the aim of obtaining higher resolution coaxial structures.

Figure 3.4 a) and b) show a microscopic image of the coaxial cross-section and coaxial tip cross-section with the associated dimensions. From the external material input, the average for the chamber diameter is 3040.82µm. This indicates that the design is within the expected range, considering maximum adhesions lining the wall. In the tip cross-section image, the average external tip dimensions are 225.55µm with the internal dimensional average being 396.98µm. Both are within the expected range of ± 65µm for the SLM system using Ti6Al4V powder as the build material.

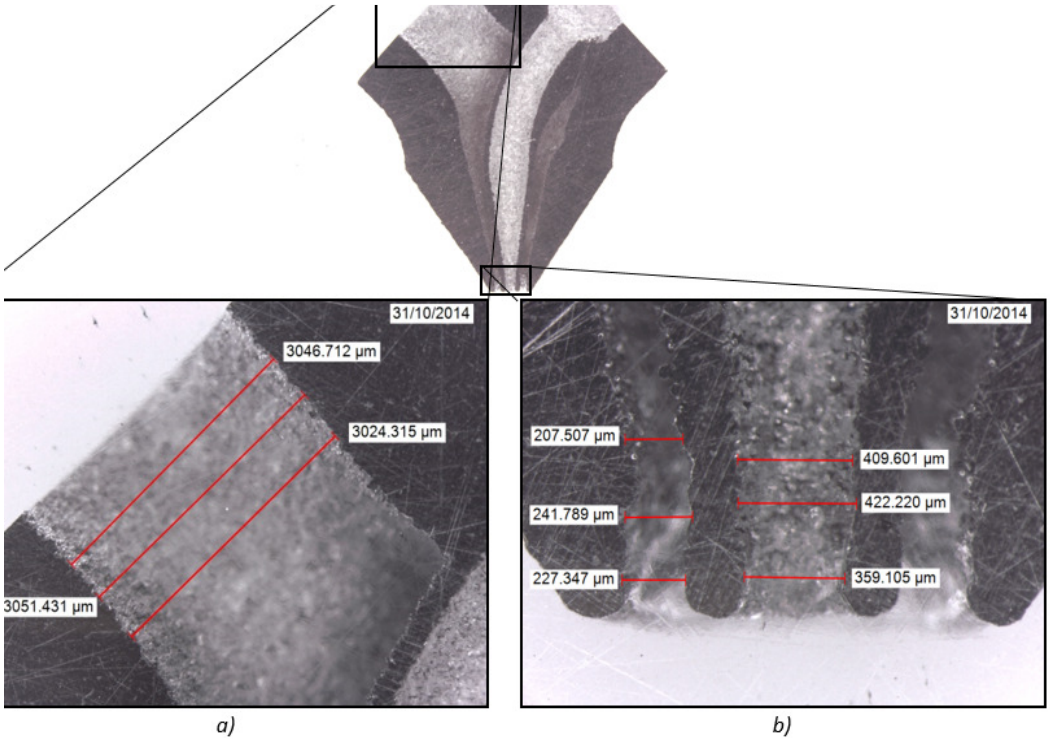

Figure 3-4 - Microscopic Images of a Cross-Section of an SLM produced Coaxial Nozzle.

a) View of the External Material Input. CAD Measurements for Associated Region = 3000µm. b) View of Tip Output.

CAD Measurements for Associated Region = 200µm and 400µm for the dimensions reading left to right.

Additional dimensional discrepancies can be seen between the angles of the internal and external heat chambers when comparing the fabricated and CAD models. Despite attempts to minimise part deformation through the incorporation of external support structure, a small amount of distortion has occurred. The CAD model measures the angle to be exactly 90^{o} while the produced component exhibits a 92^{o} angle. Though the length of the component is short, it is expected that this deformation will alter the assembly of the coaxial nozzle to the feed mechanism, likely leading to undesirable mechanical seals.

3.4 POST-FABRICATION PROCESSING

Post-fabrication processing is a necessary part of any additive fabrication method and encompasses any techniques used for material enhancements, typically enhancing strength characteristics or altering the surface finish. Within this context, we refer primarily to the decrease in the surface roughness (R_a) of the component, as the titanium alloy from which it is printed exhibits exceptional mechanical and thermal properties. As discussed in Section 3.3, the SLM process may create unwanted adhesions giving a R_a up to the size of the initial powder (65µm).

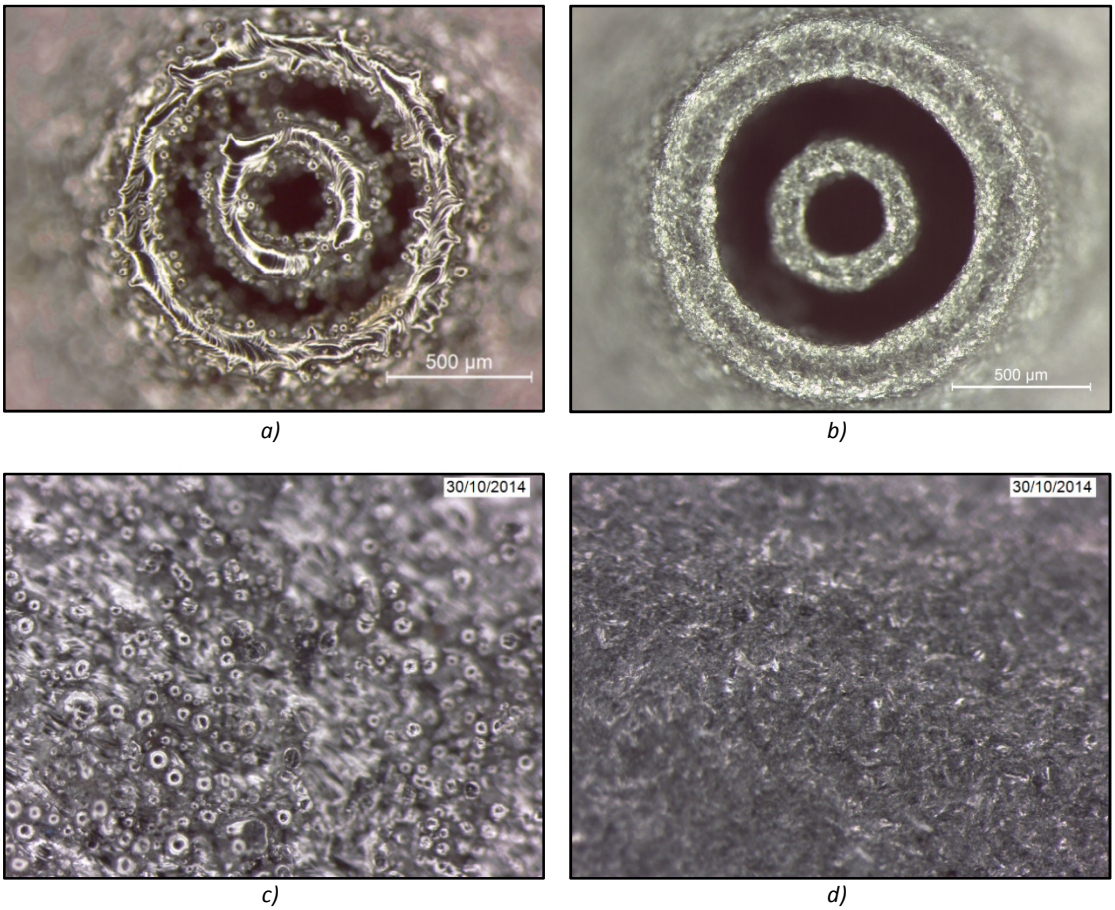

a) *b)*

c) *d)*

Figure 3-5 - Surface Roughness for SLM Fabricated Components.

a) Ti6Al4V Coaxial Tip Prior to Surface Roughness Reducing Post-Processing. b) Tip from a) after Post-Processing Sandblasting. c) External Nozzle Surface Prior to Surface Roughness Reducing Post-Processing. d) Surface from c) after Post-Processing Sandblasting.

To reduce the R_a, the titanium model undergoes an abrasive blasting process. This involves firing streams of 20µm glass particles onto the surface of the part at a high velocity. The momentum generated by this process allows it to strip the material surface of the poorly bound and unwanted adhesions. As the selected process involves such small fragments, it can safely be used on the inner chambers of the coaxial nozzle without a risk of the particles creating an obstruction. Regardless of the particle size, this process is done in bursts to further reduce the likelihood of these blockages.

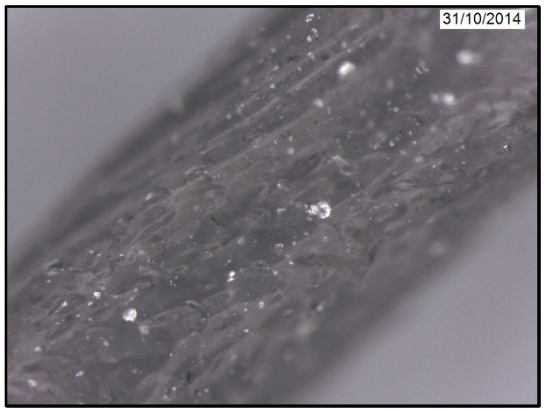

Figure 3-6- Initial Purge Material Containing Loosely Bound Titanium Alloy Particles.

The resulting component has its R_a reduced significantly. Figure 3.5 a-d) shows a comparison of a coaxial tip before and after the sandblasting process, clearly showing a removal of the externally bound powdery adhesions. Figure 3.5 b), however, still indicates that a portion of the internal adhesions remain. This suggests that a majority of the R_a reduction has occurred on the outer surface of the part, providing benefits for the assembly process and for aesthetics.

To combat the existing internal adhesions, many complex approaches were considered, though a simple solution was identified. It was hypothesised that the titanium powder adhesions would be so weakly bound to the core structure and that the first molten thermoplastic to pass through it would envelop these structures and purge them from the

system. This process involved heating the coaxial tip to an associated thermoplastic melting temperature and forcing the relevant material through it. The result of this method (Figure 3.6) shows a semitransparent PLA material embedded with Ti6Al4V particles throughout, indicating the internal structure was completely purged of the loosely bound titanium powder.

3.5 FDM ASSEMBLY

While a majority of the required components can be fabricated through a FDM or SLM process, some require an alternate means of production. This includes the creation of the PEEK thermal insulating collars (Figure 3.7) through the use of a lathe and a milling machine, as well as the various Perspex components cut using a high-powered laser cutting system.

Figure 3-7 – PEEK Thermal Insulating Collars

To assemble all the components into a functional FDM system requires several steps. These are detailed below.

Wiring Preparation: To allow the coaxial nozzle to heat in a controlled manner; four wires are required for each heat chamber. There are two wires for the thermistor connection and two

for the heating coil. To wire the thermistor, two 40mm lengths of small diameter heat-shrink tubing were carefully slid around each of the terminals extending from the thermistor tip; applying heat to reduce this diameter further. It is imperative that these two wires never touch as this can lead to a short circuit and erroneous thermal readings.

With the thermistor terminals insulated, approximately 10mm of shroud was stripped from a wire rated to carry 5V and 0.2A. Subsequently cutting an additional two lengths of 40mm heat-shrink with a slightly larger diameter than previous, these were slid onto the newly stripped wires. Finally, two crimps were used to attach the newly stripped wire to the thermistor terminals, finishing by sliding the heat-shrink over the crimps and applying heat. It is possible to complete this process by replacing crimps with soldering, though it is not recommended. Fixing the connection by soldering can damage the thermistor if done incorrectly, exposing the component to higher temperatures than it can safely tolerate.

To prepare the nichrome wire, a 300mm length of insulated NiCr was cut (8Ω) and the ends stripped 10mm. Two wires rated to carry up to 12V and 2A were stripped, exposing 10mm of wire. At this point, two 60mm lengths of fibreglass sleeving were slid onto the NiCr. It is important that the sleeving used can withstand temperatures of up to 275^{o}C, implying that typical heat-shrink will fail if used. Finally, the NiCr and the wire were attached with crimps and the fibreglass sleeving slid down to insulate the exposed connection.

Wiring the Hot-end: With the above cables constructed, it is possible to wire the coaxial nozzle. As this process requires heating the component to 275^{o}C, for safety, the hot-end was elevated from the work bench using a retort stand.

To assemble the heating coil, the prepared NiCr cable is wrapped tightly around one heat chamber, ensuring the coil is equally spaced and does not overlap at any point. As this coil heats up to its peak temperature, the insulation shrouding the nichrome diminishes, leaving it prone to short-circuits if done incorrectly. While the wrapped wire was taut, fire cement was

applied to secure the coil in place and acts as a mild thermal insulation. The proceeding task is the installation of the thermistor. These two tasks must be completed concurrently as the fire cement must be heated to be correctly cured.

To install the thermistor, a small amount of fire cement is placed into the 2mm hole located on the flange near the output for the tip. By pressing the thermal sensor into the cement, it simultaneously locks the component in place while also protecting its fragile terminal connections from undesirable stresses. With both the heating coil and thermistor fitted, the temperature was set to 270^{o}C for 30 minutes to allow for adequate curing, with the finished product shown in Figure 3.8.

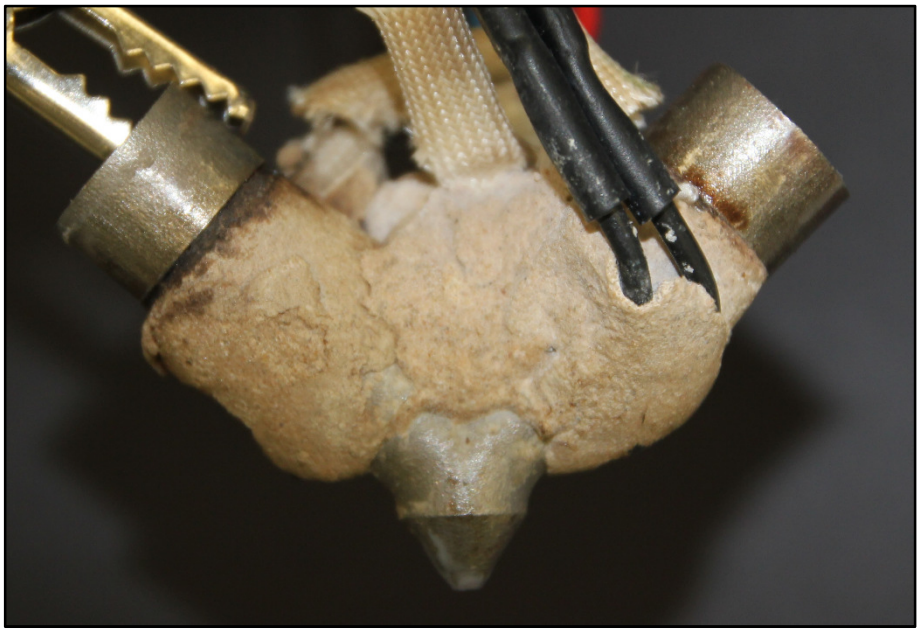

Figure 3-8 – Wired and Sealed Coaxial Nozzle

Microswitch Mounting Brackets: As discussed in Section 2.3, the fabricated microswitch brackets have been designed to fit into existing reed switch mounting points. The components themselves are anchored by means of a grub screw acting perpendicular to the bracket and through the existing support structure. The switches are attached through an interference fit between cavities in the switch body and mounting rods on the brackets. These have been

positioned the required 11mm and 17.5mm for the X and Y-axes, respectively as described in subsection 2.2.1.1.

Z-Axis Coupling: The initial Z-axis motor was a NEMA 23 stepper motor which required more current than the A4988 stepper driver could safely provide. As a result, it has been replaced with a NEMA 17 reappropriated from the original FDMs third extruder. Therefore, the shaft coupling which exists between the stepper motor shaft and the screw mechanism has been replaced. The coupling has been fixed through the use of grub screws which have been tightened with the correct series of forces to allow concentric rotation of the two shafts.

Coaxial Assembly: The coaxial assembly involves the construction of the feed mechanism, housing, coaxial nozzle, PEEK collars and PTFE tubing and fixing it to the support structure. Figure 3.9 shows a cross sectional view of the full assembly as designed, while Figure 3.10 shows the physical assembly prior to coaxial nozzle wiring.

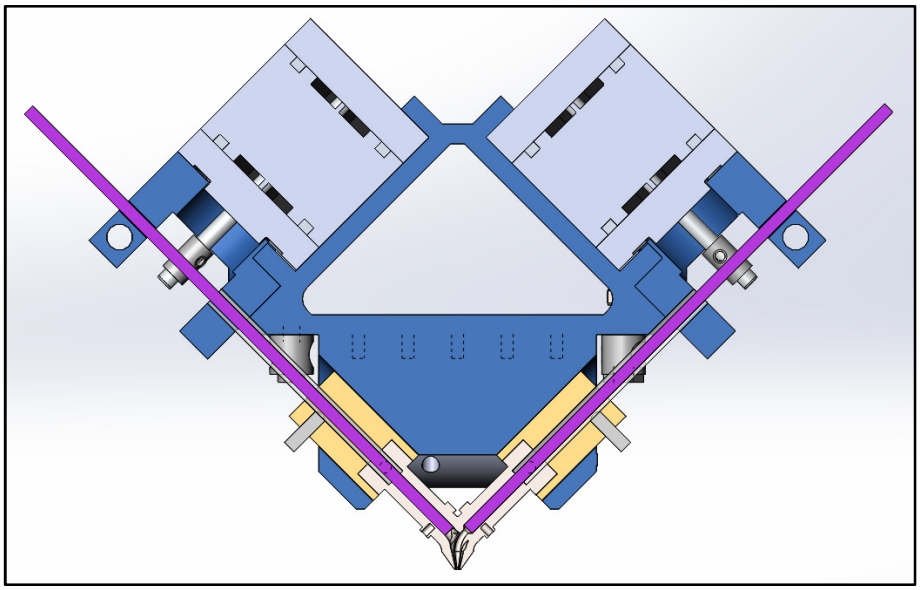

Figure 3-9 – CAD Model of Assembled Coaxial Extrusion System

To construct this assembly, the PEEK collars were placed within the housing. Following this, the coaxial nozzle was positioned along the collar's intersecting axes at which point the PEEK is slid over the top of the nozzle flange. At this point, the PTFE tubing is inserted through the collar

until it becomes flush with the flange base inside the hot-end; the process is finished by securing the nozzle to the PEEK by use of a grub screw. Subsequently, the extruders are mounted into position, with the lip of the extruder base causing further compression of the PTFE tubing into the coaxial nozzle.

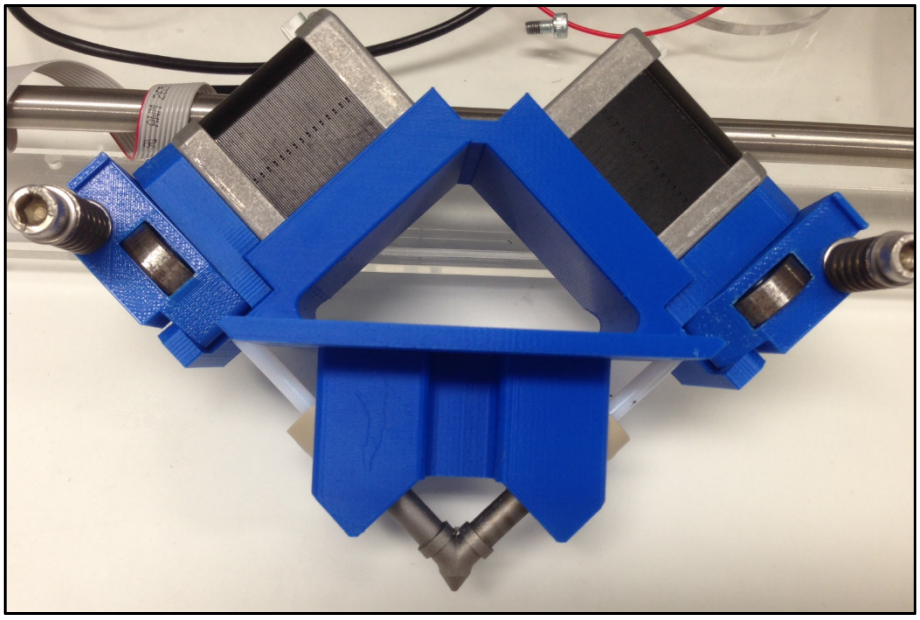

Figure 3-10 – Coaxial Extrusion System prior to Wiring of the Hot-end

With the assembly constructed, it is then attached to the support structure to permit its movement. The housing is attached to linear bearing based platforms with screws, ensuring that the grub screws in the coaxial nozzle face away from the front of the system. The housing is then attached to the X-axis stepper motor through two grub screw locking mechanisms. It is crucial to secure the locking mechanism with the circular mounting hole last as this shape permits rotation, therefore, the process of attaching the screw simultaneously tightens the X-axis belt.

4 RESULTS AND DISCUSSION

This chapter details the results obtained from the operation of the device designed and fabricated in Chapters 2 and 3. Within this chapter, the means of testing the device to determine its accuracy in operation by producing coaxial structures is discussed. Subsequently, methods to improve the concentricity of multi-layer structures are examined as well as determination of individual fibre strength characteristics. Finally, the external effects which impact on the overall print resolution are identified and discussed. All results obtained are discussed and their implications for further development of AF research are presented.

4.1 COAXIAL MEASUREMENTS

Coaxial Fibre

The concentricity of individually produced coaxial fibres is a key milestone for the successful completion of this work. Coaxial samples have been obtained by extruding two PLA materials through the coaxial nozzle at speeds calculated in Chapter 2. The tip was heated to 200^{o}C and both flow rates controlled at 0.001 (m/s) and 0.0002 (m/s) for the external and internal material, respectively. The extruded distance was measured to be 10mm of 3mm diameter feedstock, with the resultant material free to flow without contact to the substrate. The length of the extrudate is small enough to prevent deformation from a drawing effect; a change in cross-section in response to the weight of the produced fibre. This allows it to maintain its coaxial and cylindrical shape for ease of cross-sectional analysis. This procedure was conducted

three times and the fibre cross-sectioned by a scalpel. The dissected fibre was examined using a Leica M205A microscope; an example of the resultant fibre is shown in Figure 4.2.

To assess the concentricity of the coaxial fibres, a method has been devised on the basis of the coaxial extrusion research by Cornock et.al. [66]. While the research does not indicate the exact process for assessing concentricity, it states that the desired measurement is between the longitudinal axis for both the internal and external materials. Therefore, the central axis for each material must be located and the distance between them measured. This is to be expressed as a percentage of the external material's radius to account for any dimensional variation between samples. The core material offset has been calculated using Eq.4.1 and uses Figure 4.1 as a guide while Figure 4.2 shows an analysed cross-sectional sample.

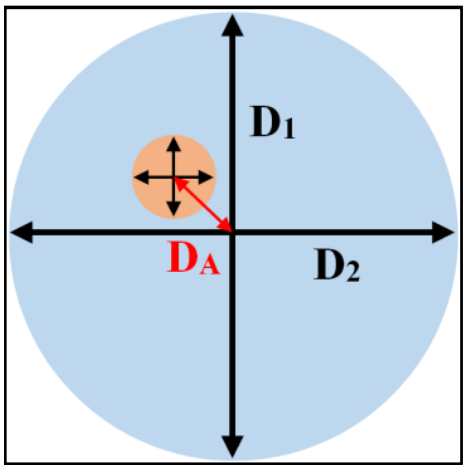

Figure 4-1 - Guide for the Calculation of Coaxial Axis Offset

$$O_A = \frac{2D_A}{\frac{D_1+D_2}{2}} \times 100 \qquad (4.1)$$

Where

$O_A = Axis\ Offset\ (\%).$

$D_A = Distance\ from\ External\ Axis\ to\ Internal\ Axis.$

$D_1 = Diameter\ 1\ of\ External\ Material.$

$D_2 = Diameter\ 2\ of\ External\ Material.$

$Note$: D_1 and D_2 are to be perpendicular measurements about their midpoint.

By using this method to calculate offset, the effect of variation in the external diameter is minimised. By taking the average of both the vertical and horizontal diameters, it is possible to obtain a more relevant measure of offset. Failing to do so would result in skewed data as the resultant coaxial fibres are not perfectly symmetrical in shape. Therefore, measuring an offset with respect to a non-symmetric shape would give ambiguous results.

Conducting the measurements and compiling the data for coaxial concentricity at 200^{o}C under the flow conditions described previously results in an average axis offset of 9.77% with a standard deviation of 3.8%. The range of offsets is 7.53% and associated minimum and maximum values are 5.5% and 13.03%, respectively. This data indicates that the coaxial nozzle produced has been successful in completing its second objective, producing coaxial offsets well below the literature standards of an average of 22% [66].

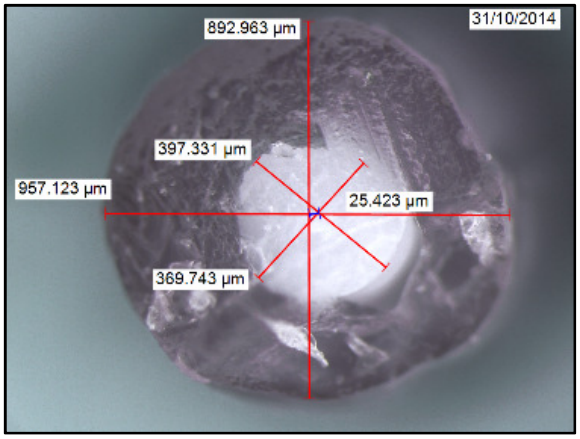

Figure 4-2– Cross-Sectional View of Coaxial Fibre

While obtaining concentricity of the extrudate is a milestone for this work, producing a material with reliable and repeatable dimensions is of equal importance. To assess this factor, both the internal and external material dimensions from the coaxial cross-sections have been examined using a Leica M205A microscope. An example of the obtained data is seen in Figure 4.2. Table 4.1 compares the internal and external material dimensions to their respective orifices of extrusion using the triplicate results obtained previously. As with the coaxial

measurements, a horizontal dimension and a vertical dimension are taken for each structure, minimising the impact of non-symmetric shapes may have on the results.

Table 4.1 - Physical Model Measurements Compared to CAD Model Dimensions

	Measured Average Diameter (µm)	CAD Model Diameter (µm)	Average Difference (µm | %)
Internal	451.4848	400	51.48 | 12.8
External	983.2233	1200	-216.777 | -18.1

Table 4.1 shows that the diameter of the internal material is on average 12.8% larger than the anticipated. The external material exhibits opposing features, producing diameters 18.1% smaller than the expected. This external material measurement is counterintuitive on the basis of thermal expansion, though can be explained. The reason behind these results is associated with the wall thickness of the internal nozzle.

This feature exhibits a 200µm wall for the internal material and is a boundary which abruptly stops, allowing the two fluids to interface. The lack of a tapered edge on the internal nozzle fails to guide the fluids to interface as desired, however due to die swelling from extruding polymers; it is likely that materials will increase in size as they exit the hot-end. It is expected that the external material exhibits a greater change in diameter as it shields the internal material from further die swelling. This gives the external material two exposed surfaces to expand from rather than the single exposed surface of the internal material. As the two materials make contact and begin to cool, the effect of the swelling for the internal material is limited to the point where the fluids initially interface.

Additional information reinforces the theory that the discrepancies in the material dimensions are attributed to wall thickness. By performing a comparison between combined nozzle

material area and combined coaxial material area, it is possible to see what the true expected external diameter is. This information is shown in Table 4.2 which indicates that there is a 0.0049mm^2 difference between the expected total area and the tips' total area. This small number reinforces that the average external material diameter is expected to be approximately 980µm instead of the tip diameter of 1200µm.

Table 4.2 - Diameter and Area Comparison between Coaxial Nozzle and the Produced Fibre

	Internal (mm)	Wall Thickness (mm)	External (mm)	Material only Area (mm^2)	Expected Diameter from Material only Area (mm)
Nozzle	0.4	0.2	1.2	0.753982	0.979
Fibre	0.451	-	0.983	0.758922	0.983

Additionally, this information must be considered when creating any subsequent coaxial nozzle geometry. Attempts to increase the resolution of the print material by decreasing the external diameter of the coaxial nozzle will have a greater effect than anticipated. The wall thickness must be accounted for in future developments of coaxial printing, particularly if being designed to have a volumetric ratio of internal material: external material.

This method and data set will produce, on average, coaxial fibres with 983µm external diameter, 451µm internal diameter, and their concentricity will be 9.77%. Converting the percentage to dimensions indicates that the internal material's longitudinal axis is within a 48 µm radius of the external material's longitudinal axis. This value is less than a half of the distance specified in the literature [66], indicating that the coaxial concentricity has been achieved within the desired range specified in Section 1.7.

Coaxial Coating

This same process has been applied to the developed coaxial coating nozzle. Coaxial samples have been produced by extruding PLA through the designed tip, with both heat chambers set to 200°C and extrusion speed set to 0.001(m/s). The process involved extruding 10mm of 1.75mm diameter feedstock through the tip with the resultant material free to flow without contact to the substrate. This prevents any cross-sectional change due to a fibre drawing effect and allows for an ease of cross-sectional measurement. This process was conducted three times while using the internal material as a 190µm copper wire and three times while using a 65µm iron wire. The fibres were cross-sectioned by a scalpel. The dissected fibre was examined using a Leica M205A microscope; an example of the resultant fibres is shown in Figure 4.3.

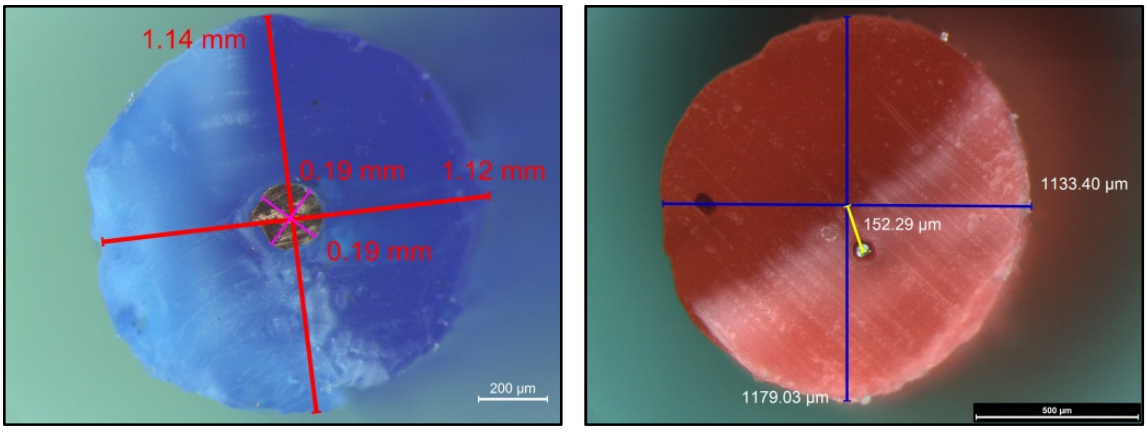

a) b)

Figure 4-3 - Cross-Sectional View of Coaxial Coating Process.

a) Fibre produced using 190µm core copper wire. b) Fibre produced using 65µm iron wire.

Due to the nature of the passive extrusion system, coaxial concentricity is difficult to replicate. The rigidity in the core material maintains a small proportion of its initial curvature in the extrusion process. This results in movement of the core material within the cooling polymer sheath, therefore altering initial concentricity. While cross-sections such as those shown in Figure 4.3 can be produced, often more hollowed cross-sections result (Figure 4.4).

As consistent cross-sections cannot be reliably replicated, data relating to concentricity has not been evaluated. The uniform velocity profiled created in subsection 2.2.1.3 appears to have played no notable role in producing coaxially concentric fibres. While it is likely the optimised velocity profile will enhance the symmetry of thermoplastic binding to core material, the rate of cooling clearly plays a more significant impact in producing coated concentric fibres.

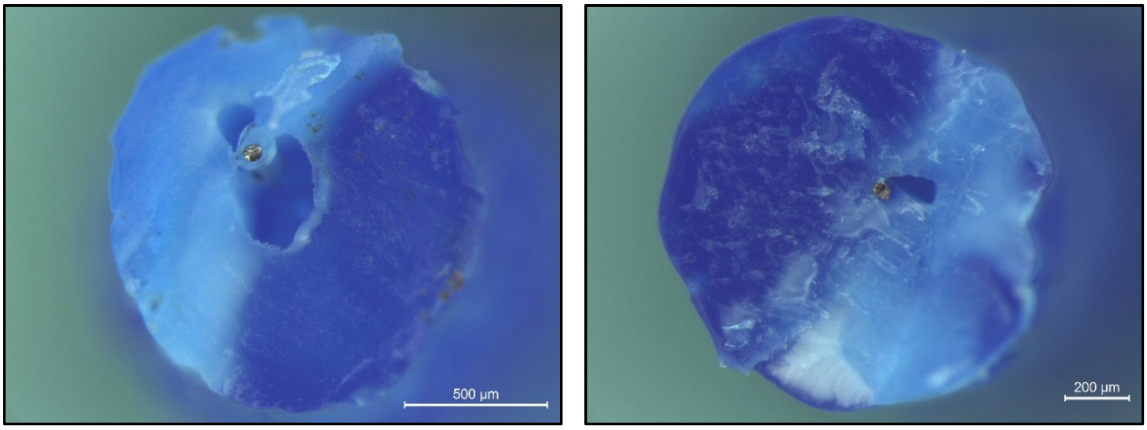

a) b)

Figure 4-4 – Cross-Sectional View of Coaxial Coating with 65µm Iron.

a) Extreme Case of Core Material Movement Resulting in Large Hollowed Section Neighbouring Core Material. b) Typical Magnitude of Movement for Specified Core Material Coated Printing.

By altering the cooling process or decreasing the amount of molten material, it may be possible to control the core material curvature and produce repeatable and concentric fibres. An increased cooling process may solidify the thermoplastic before the core material curvature has the potential to move and disrupt the sheath. However, it is more likely that a decreased amount of sheath material will have a larger impact. By decreasing the diameter of the sheath material, the rate of cooling required will in-turn decrease. This may be difficult to achieve given the dimensional restrictions for objects produced using SLM fabrication as mentioned in section 3.3.

However, this issue of core material movement may prove to be insignificant during the printing process. As the two materials are being deposited in the FDM process, they are forced into the substrate or preceding material layers. This creates a compressed structure,

potentially removing the unwanted core material movement from the process and thereby eliminating the hollowed effect seen in straight extrusion. If the sheath thermoplastic has not cooled sufficiently prior to the coaxial tip changing direction during printing, the core material may pull through the semi-molten polymer. This suggests three potential mechanisms for improvement, active cooling on the thermoplastic sheath, decreased sheath diameter or a slower printing process.

4.2 IMPACT OF FLOW-RATE ON CONCENTRICITY

Based on the coaxial concentricity defined, the system can be tested to optimise parameters governing its performance. This section examines the rate at which feedstock is to be supplied to the hot-end (flow-rate) on coaxial concentricity for coaxial fibres. Flow-rate for concentricity for coaxially coated fibres has not been assessed due to repeatability problems mentioned in section 4.1.

It is expected that an optimum flow rate will exist for coaxial fibre deposition, where internal flow parameters are most uniform, producing more uniform concentric structures. Additionally, it is anticipated that lower flow rates will have less impact on die swelling. This is due to the molten material being held at pressure and temperature for longer, allowing the polymer chains to relax or detangle.

Figure 4.5 shows the effect of flow-rate on coaxial concentricity for coaxial fibres produced using PLA for both internal and external materials, clearly indicating an optimum parameter range to obtain ideal results. Flow-rates of 40 and 50 (mm/min) produce coaxial offsets of 2.89% and 3.5%, respectively. This demonstrates the range over which the system will produce

the most coaxial structures. This result was anticipated, though the mechanisms governing these findings are numerous but are highly attributed to polymer melting time.

While it was expected that varying the flow-rate would alter the internal flow parameters, the most influential factor was deemed to be time the feedstock spent in the heat chamber. By slowing the flow-rate, the feedstock remains within the heat chamber for a longer duration, allowing it to reach higher temperatures. This in turn lowers the viscosity of the molten polymer, allowing it to flow more freely. Consequently, allowing the external material to more readily envelope the gap which exists due to the internal nozzle wall.

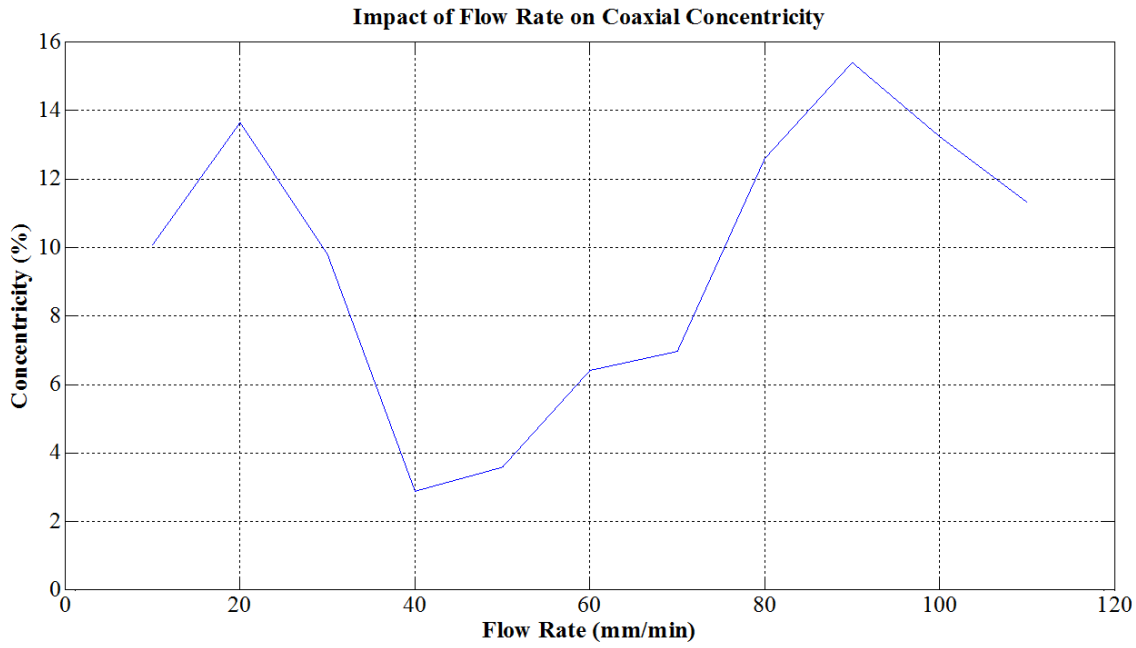

Figure 4-5 - Impact of Flow-Rate on Coaxial Concentricity of Coaxial Fibre

This indicates two key outcomes, that flow-rate does impact coaxial fibre concentricity, and also that concentricity is highly linked to material viscosity, and therefore print temperature. This test was conducted at 200^{o}C and flow rates linked at a ratio of 5:1 for external and internal materials.

Though the increased fluid temperature may produce more uniform coaxial structures, it may have detrimental effects on structures printed onto a substrate instead of freely extruded. The

rate of cooling and material deformation resulting from depositing a higher temperature liquid will likely impact the coaxial quality of printed structures. Suggesting that printing at lower flow-rates may require external cooling on the resultant fibres to maintain their desired geometrical states.

Consequently, the increased temperature, and potential external cooling, is likely to induce undesirable internal stresses in the produced coaxial fibre as well as locking the extrudate in its polymer entangled state. The introduction of a sudden thermal gradient will cause a variation in cooling between the internal and external materials, causing stresses to form within the structure, altering its mechanical strength. However, it is likely the internal material will be shielded from this effect and will remain largely unaffected, implying a weaker sheath with a stronger core material.

4.3 TENSILE TESTING

Coaxial Fibre

With the device assessed for its concentricity based on flow-rate, this section examines the impact of extrusion temperature on tensile strength. Determining fibre strength as a result of extrusion temperature will be highly influential on obtaining optimised parameters for printing structures with PLA for both core and sheath materials. It is expected that an optimum extrusion temperature will exist which will allow the two materials to create a strong merged structure. It is anticipated that higher print temperatures will have a positive effect on the produced fibres strength, up to the point at which the PLA begins to reach its degradation temperature of 200^{o}C [69].

The fibres for testing were produced by extruding 30mm of a PLA core and sheath filament at a flow-rate of 40 mm/min as this velocity produced the most coaxially concentric fibres. This process was repeated five times for temperatures of 190^{o}C, 200^{o}C and 210^{o}C. The fibres were extruded freely so as not to touch the substrate, though they were extruded at such a length that a drawing effect had not visibly occurred. The test samples were allowed to cool by their exposure to an ambient temperature of 23.5^{o}C and were cut from the coaxial nozzle using snips.

The samples were tensile tested using a Shimadzu Compact Tabletop Testing Machine EZTest and a load cell of 50N. The samples were cut to be 30mm in length and each sample diameter was measured three times using a Mitutoyo I 65 micrometre (resolution of 0.001mm) and the average of the diameters used as gauge diameter. The samples were then placed into two clamps to anchor them; due to the thin diameter and low surface roughness of the samples, P60 sandpaper was used on the inside of the clamping mechanism to increase friction to the sample and prevent slippage, see Figure 4.6b) for tensile testing layout.

Tests were conducted using a cylindrical testing method, specifying the gauge diameter as a result of individual measurements for each sample and a gauge length of 30mm. The test process strained the sample at a rate of 1mm/min. Any test which exhibited slipping within the clamps was discarded. All resultant data was imported to MATLAB to be processed and plotted.

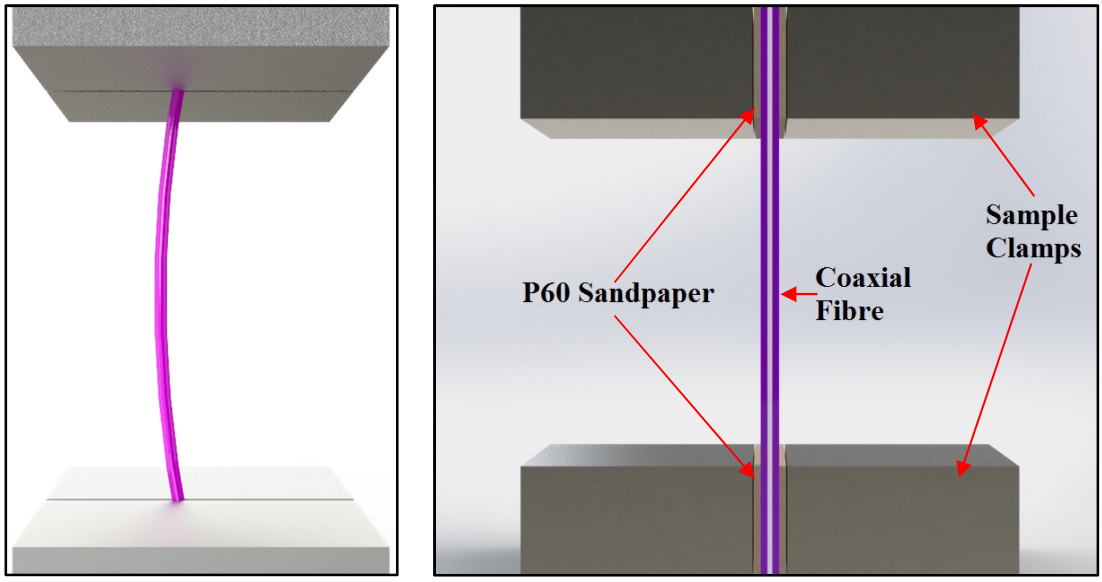

a) b)

Figure 4-6 - Tensile Testing Layout

a) Samples for Tensile Testing Exhibited a Curved Geometry Prior to Force Application. b) Tensile Testing Schematic and Linear Sample Geometry after Tensile Testing Toe-in Region.

Figure 4.7 shows the stress-strain curve for tensile tests conducted at 190°C, 200°C and 210°C and clearly shows differing peak stresses for each temperature related test. The shape of the stress curves look to be appropriate for PLA undergoing tensile testing, exhibiting brittle failure. However, a section below 2% strain exhibits unusual characteristics. For a range between approximately 0.3% to 1.5% strain, the stress appears to prematurely plateau, with the same phenomenon found in Figure 4.8 (coaxially coated fibres). This dramatic decrease in stress accumulation can be attributed to the physical shape of the fibres being tested.

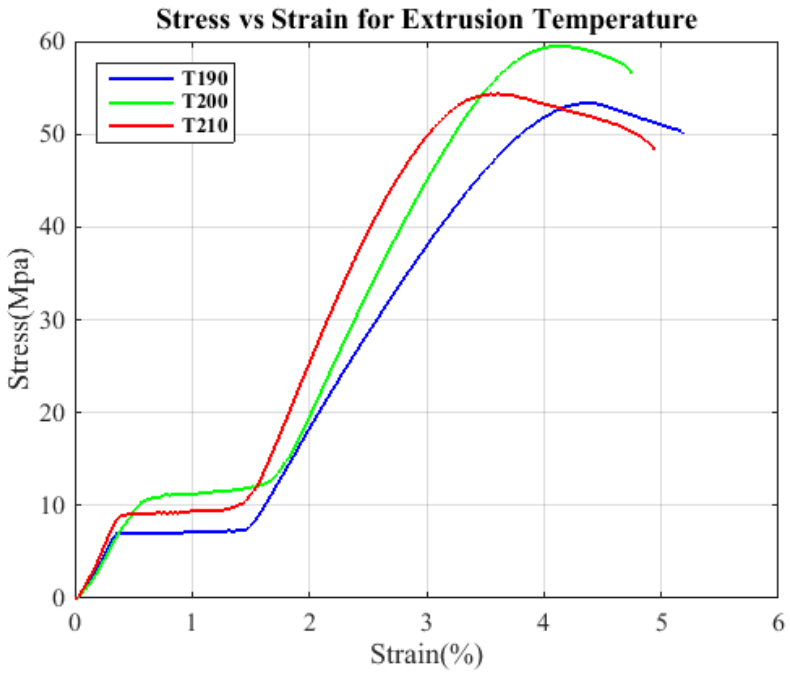

Figure 4-7-Stress Strain Curve for PLA Sheath and Core Materials. Testing 190 °C, 200 °C and 210 °C

The fibres were produced by extrusion into free space. By the nature of this free extrusion, fibres have been created which are not linear, but rather exhibit an elongated curve (Figure 4.6a). We postulate that the plateau in the stress curve is a result of a reorientation of the fibre undergoing tensile testing. Upon observation of the testing process, it was evident that under the stress values in question, the fibre sample would begin to lose its curvature and become linear.

It appears that prior to the required stress, the force is not high enough to overcome the material curvature and instead accumulates within the fibre. Once the critical stress is reached, the reorientation occurs, and subsequently, tensile testing resumes as normal. This phenomenon appears to be similar to a toe-in region, whereby structures reorientate themselves under an external load. This characteristic is typically seen from zero strain, rather than after a brief period of strain.

Figure 4.7 shows a maximum overall strength at 200^{o}C with 190^{o}C and 210^{o}C slightly lower. It is expected that this peak value is the result of the two materials reaching temperatures just

below the PLA degradation temperature of 200^{o}C. While the heat chambers themselves are set to 200^{o}C, the flow-rate associated prevents the feedstock material from reaching this temperature. The constant flow of lower temperature material is at such a rate that the external material is not exposed to the degradation temperature for a significant duration for thermal conductivity to allow the material to reach the heat chamber temperature. While this is the case for the external material, the internal material is extruded 80% slower and has sufficient time to reach the heat chamber temperature. This is reinforced from the simulation data shown in Figure 2.11b. By this indication, it is possible that the internal material heat chamber setting should be lowered to prevent the PLA from reaching its degradation temperature.

It is expected that setting the heat chamber temperatures to above the degradation temperature (210^{o}C) results in the external material reaching its degradation temperature in the extrusion process. This may cause damage to the polymer chain, potentially reducing the molecular weight of the structure and its associated mechanical strength. In addition to this, the internal material will reach temperatures above its thermal degradation and may contribute further to this negative effect.

Setting the heat chamber temperature to below thermal degradation temperature (190^{o}C) produced fibres which exhibit similar strength characteristics to that of fibres extruded at 210^{o}C. This is likely due to decreased melt temperature for the external liquid, minimising energy on material merge. However, at this temperature, the internal material is no longer exposed to degradation temperatures, though it still produces lower mechanical strength fibres than the 200^{o}C setting.

Coaxial Coating

The fibres for coaxial coating testing were produced and assessed using the same methodology as specified for coaxial fibres, using a PLA sheath and 65µm iron for the core material.

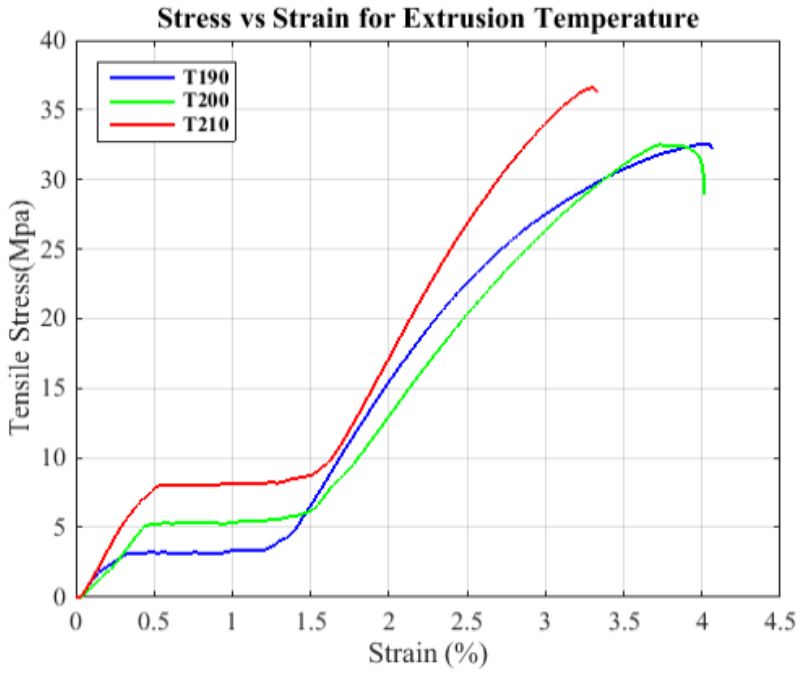

Figure 4-8-Stress Strain Curve for PLA Sheath and 65µm Iron Core. Testing 190 °C, 200 °C and 210 °C

Figure 4.8 shows the stress-strain curve for tensile tests conducted at 190°C, 200°C and 210°C for coaxially coated fibres using PLA for the sheath material and 65µm iron for the core material. The curve shows clearly differing peak stresses for each temperature related test. As with Figure 4.7, the shape of the stress curves appear appropriate for PLA undergoing tensile testing, exhibiting brittle fracture [70]. The fibres produced exhibit the same toe-in related characteristics as described previously, likely due to their elongated curve shape.

Figure 4.8 shows a maximum overall strength at 210°C with 190°C and 200°C slightly lower. It is expected that this peak value due to the PLA reaching temperatures just below its degradation temperature, similar to tensile testing for coaxial fibres. While the heat chamber is set to 210°C, the flow-rate associated prevents the feedstock from reaching this

temperature. Unlike coaxial fibre testing, the internal material is not subjected to a temperature for a sufficient duration so as to change its viscous properties. Instead, the thermal conductivity is only relevant to the sheath material.

It is likely that setting the heat chamber to 210^{o}C (above degradation temperature for PLA) allows the sheath material to reach values close to 200^{o}C but not exceed it. This is due to the flow-rate associated with the sheath fluid. As the material is passing through the chamber at a sufficient rate, it will never have adequate time to reach the temperature of the surrounding structure. This prevents portions of degraded PLA being present in the extruded fibre and the exhibiting associated decreases in tensile strength.

While the above explanation can hypothesis the reason for obtaining peak tensile strength at 210^{o}C, it does not enlighten as to why the remaining extrusion temperatures exhibit similar tensile strengths. It is likely that the core material plays an insignificant role in individually contributing to the coaxially coated fibres strength, however, the diameter of the material may. As it is seen with the coaxial fibre extrusion, the sheath material envelopes the core structure as it passes into free space. It is likely that the viscosity of the sheath material will dictate the extent to which the sheath material will bind to the core material.

A decrease in viscosity as a result of an increase in fluid temperature may alter the bonding of the polymer sheath to the iron core. However, the required viscosity to allow for substantial bonding to form may be exhibited only at temperatures nearing 210^{o}C. This would reduce the likelihood of both the lower extrusion temperatures from obtaining significant differences in tensile strength. As 190^{o}C and 200^{o}C may both fail to allow the fluid to reach a desired viscosity for increased bonding, the impact of extrusion temperature may only affect the polymer chain structure, and not the bonding to the iron core. Potentially explaining why both lower temperatures extrusions failed at similar stresses.

4.4 CALIBRATION

The calibration of this device is paramount for it to perform as required that is to say, to deposit concentric, coaxial materials in a desired geometry onto a substrate. This process is completed by configuring the slicing software parameters to suit the fabrication requirements and environment. This also requires physical measurements of the device to be included in the firmware. The parameter optimisation is an iterative process involving altering extruder speeds, x and y axis motor speeds, layer height, nozzle output diameter and filament deposition width settings.

For a uniform deposition, the output speed is equal to the hot-end movement speed. Indicating that the nozzle must only move as fast as it can deposit a full stream of extrudate, and vice versa. Therefore, two key parameters will affect the calibration settings governing coaxial deposition; the rate at which feedstock is to be supplied to the hot-end (flow-rate) and the speed at which the hot-end moves (feed-rate). The feed-rate is a stable movement with only motor rotational speed and its associated linear translational characteristics affecting it. The flow-rate, however, has much greater variability in its control process. For this calibration, the feed-rate is equal to the calculated flow-rate.

The flow-rate is governed by these factors; motor rotational speed, material input diameter, nozzle output diameter and material heat conduction. As the internal material flow-rate has been programmed to be dependent on the external flow-rate, this calibration only needs to be completed for the external material. For the purpose of calibration and initial printing, any material retract settings have been disabled. This process occurs immediately prior to the hot-end performing a non-extruding movement; implemented to prevent molten material leakage.

Given the simulations completed and thermal conductivity to PLA, the extruder speed is fixed to 60 rpm. The material input is specified to be a 3mm diameter; however, upon measuring with digital callipers, it has shown an average of 2.88mm. For the calibration calculations, the average material input is set to a 2.88mm diameter. The output diameter is only considered for the external material. Using the tip area for the external material in subsection 2.2.1.2, we can normalise this area to find its equivalent diameter if it were not coaxial. This is done by rearranging the equation for the area of a circle (Eq.4.2), resulting in an equivalent diameter of 0.8944mm.

$$r = \sqrt{\frac{TipArea}{\pi}} \tag{4.2}$$

With the feed-rate and flow-rate determined, the calibration process focusses upon the layer height resolution and the width of deposition for the extruded material. These are crucial parameters as they must blend to provide a coaxial structure, but must also deposit material of sufficient width to allow it to adhere to surrounding material. This segment of the calibration process was iterative, with the progressive results shown in the next section.

4.5 Multi-Layer Structures

Coaxial Fibre

With coaxial fibre extrudate being produced, the device was assessed in its ability to create multi-layer coaxial structures. To do so, a concentric square pattern was created using CAD and the file processed accordingly to allow for slice data to be created. This information was then uploaded to the system through a control interface and processed. The resultant structure was cross-sectioned by a scalpel and examined using a Leica M205A optical microscope.

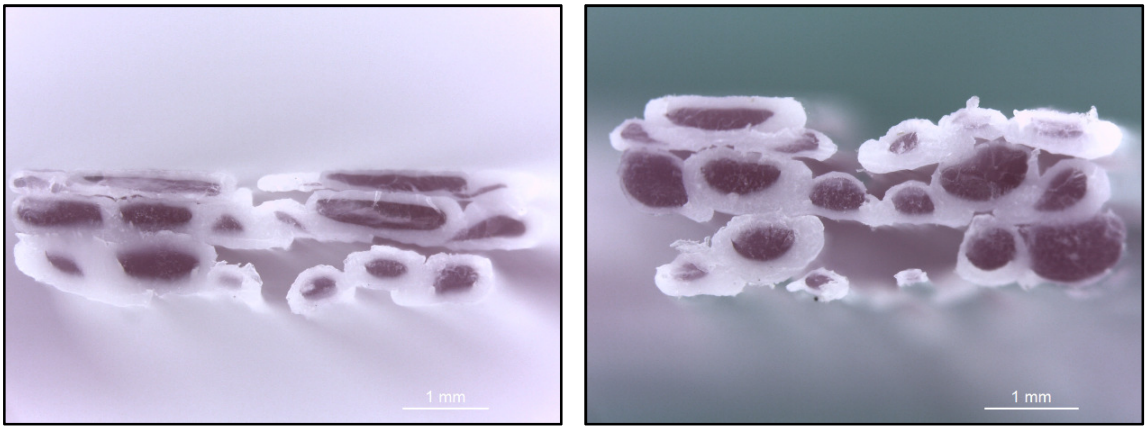

a) *b)*

Figure 4-9-Preliminary Multi-Layered Structures.

a) Trial 1 at 0.5mm Layer Resolution. b) Trial 2 at 0.65mm Layer Resolution

As a result of the iterative process refining layer resolution and extrudate deposition width, improvements were made to the images shown in Figure 4.9. By optimising this process, it was possible to create cohesive, repeatable, coaxial multi-layer structures. Increasing the layer resolution and deposition width to 0.8mm for each parameter has allowed for a significant improvement in the component output, depositing fully encapsulated coaxial fibres with sufficient width to allow them to adhere to their neighbouring materials. This tuned configuration led to the fabrication of the sample in Figure 4.10, a five layer coaxial structure. While six layers are present, the first is an adherence layer whose purpose is to create stability for the subsequent layers.

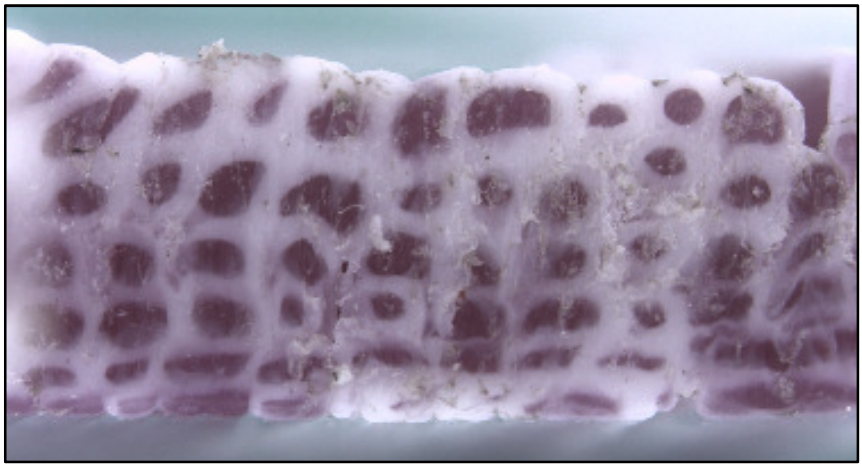

Figure 4-10-Multi-Layer Coaxial Structure produced using Optimised Calibration Parameters.

Measuring the resultant coaxial dimensions for each fibre is impossible as there is no boundary to divide two merged external materials. Instead, a dimensional analysis is conducted on the internal material dimensions only, comparing them to the coaxial fibres produced in Section 4.2 and to the tip dimensions (Table 4.3). As with the coaxial measurements, a horizontal measurement and a vertical measurement are taken for the internal structure, minimising the impact of non-symmetric shapes may have on the results.

Table 4.3 - Dimensional Comparison for Multi-Layer Structures to Coaxial Fibres and CAD Model

	Structure Average Diameter (µm)	Fibre Average Diameter (µm)	CAD Model Diameter (µm)	Difference from Model (µm | %)
Internal	518.414	451.4848	400	118.4 | 29.6

The average internal material diameter for the multi-layer structures is significantly higher than the internal nozzle diameter. Values 29.6% larger have been measured to be the average, linking this to the results found for the coaxial measurement suggests that this increase in size may not be due to the removal of the wall thickness in the materials transition from nozzle to

the environment. Therefore, indicating that other factors are influencing this dimensional change.

On inspection of Figure 4.10, the internal structures appear skewed; many are not circular, but more rectangular. This suggests that the discrepancies in the dimensional measurement may be linked to the horizontal measurements of the internal structures, while the vertical measurements are more accurate. This is likely due to non-optimised parameters for layer height settings. The fibre is expected to be compressed on printing, thereby losing its cylindrical shape on deposition and producing the resultant rectangular geometries.

While the layer height is a likely contributing factor to the non-symmetrical nature of the multi-layer fibres, it is not the only parameter which may produce this print deformation. It is a possibility that either feed-rate or flow-rate may need to be modified to improve this geometry. Issues such as this may occur if the hot-end is depositing material too quickly, or if the nozzle is moving too slowly, resulting in a non-uniform structure on the substrate.

Consequently, it may prove difficult to obtain truly concentric coaxial fibres in the production of multi-layer structures. Typical FDM processes compress the material into the substrate or into preceding layers, creating extrudate pathways with flat surfaces on both the top and bottom. Applying this process to coaxial printing will result in features which are less likely to be concentric and more likely to be rectangular in nature, similar to those shown in Figure 4.10, though more linearly structured. The consistency of the coaxial deposition can only be obtained by optimising fluid flow parameters for the designed tip, coupled with appropriate thermal settings of the input materials to achieve their desired print viscosity.

Coaxial Coating

With coaxially coated fibres being produced, the device was calibrated to produce multi-layer conductive structures. To do this, several test patterns were created and processed into STL

format. The patterns assessed deposition rate and tip movement speed in relation to the production of a structure with an encapsulated conductive core. As with coaxial fibre structures, STL data was uploaded to the system through a control interface and processed.

Through an iterative process, a range of parameters were identified to allow for the production of encapsulated multi-layer structures. Initial prints were conducted to determine if issues discussed in section 4.1 would eventuate, specifically investigating the impact of the sheath thermoplastic cooling prior to the coaxial tip changing direction during printing. With the expectation being that the core material may pull through the semi-molten polymer.

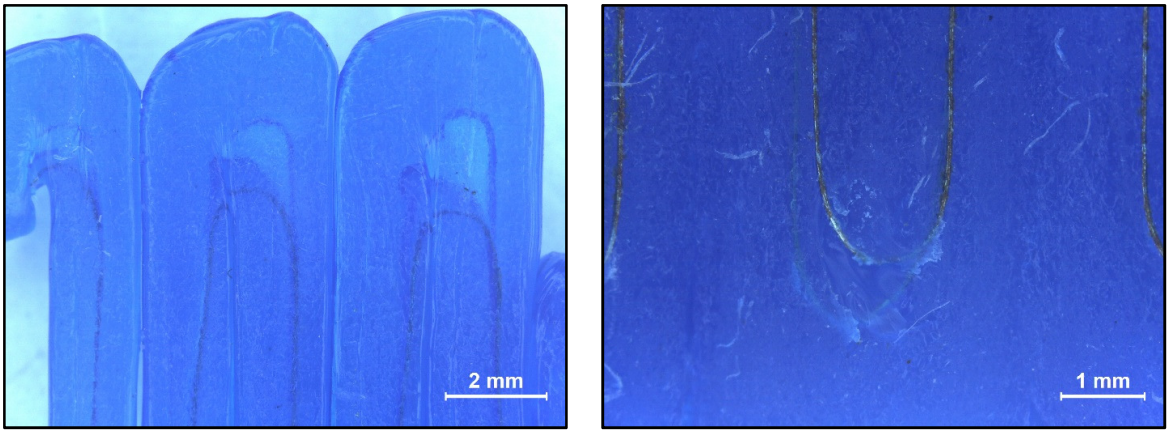

a) *b)*

Figure 4-11-Microscopic Images of Coaxially Coated Prints.

a) Prints at Moderate Speed Pull Core Material Through Semi-Molten Polymer in 180° Print Turns. b) Lowered Print Speeds Reduce the Effect.

Figure 4.11a shows the impact of a 180° tip direction change on core material encapsulation when printed at moderate speeds. Clearly identifying regions where the wire core has pulled through the molten polymer during the print process. Stepping down printing speeds resulted in reliable encapsulation during printing as seen in Figure 4.11b, though small amounts of core material movement were still evident through the semi-transparent thermoplastic. However, as anticipated in Section45.1, the compressive nature of FDM has removed the voids within

the material cross-section and produced solid, un-porous structures when viewed on a micro level.

With the parameters defined, a multi-layer structure was produced; Figure 4.12a and b show a 10 layer cube printed with a 65µm iron core. The structure exhibited conductive continuity for the iron core when terminals were exposed on both the top and bottom of the cube. Indicating that no break has occurred during the printing process and that current can flow throughout. It became evident that the small amounts of core material movement seen at the reduced printing speed had a cascading impact on a multi-layer structure. Printed regions immediately after a tip directional change resulted in small deformation in the sheath material as seen in Figure 4.12b. While these deformations are minor, they must be addressed to produce multi-layer structures more reliably.

a) *b)*

Figure 4-12– Coaxially Coated Multi-Layer Structures.

a) Bottom-up View of 10 Layer Cube Showing Iron Core Embedded within Surrounding PLA. b) Top View 10 Layer Cube

This concept of multi-layer conductive structures is currently under experimentation in an attempt to produce a variety of conductive components. Initial objects for test printing include RFID tags, air-core transformers, strain gauges as well as wearable, flexible electronic circuits. Figure 4.13a shows a preliminary print of an RFID tag designed to couple to standard

13.56MHz RFID readers. Figure 4.13 b) and d) show microscopic images of the printed structure, identifying the encapsulation and centralisation of the core material within the thermoplastic sheath. As previously identified, coaxial tip turns of even 90° can suffice to pull the core material from within the printed sheath, as seen in Figure 4.13c).

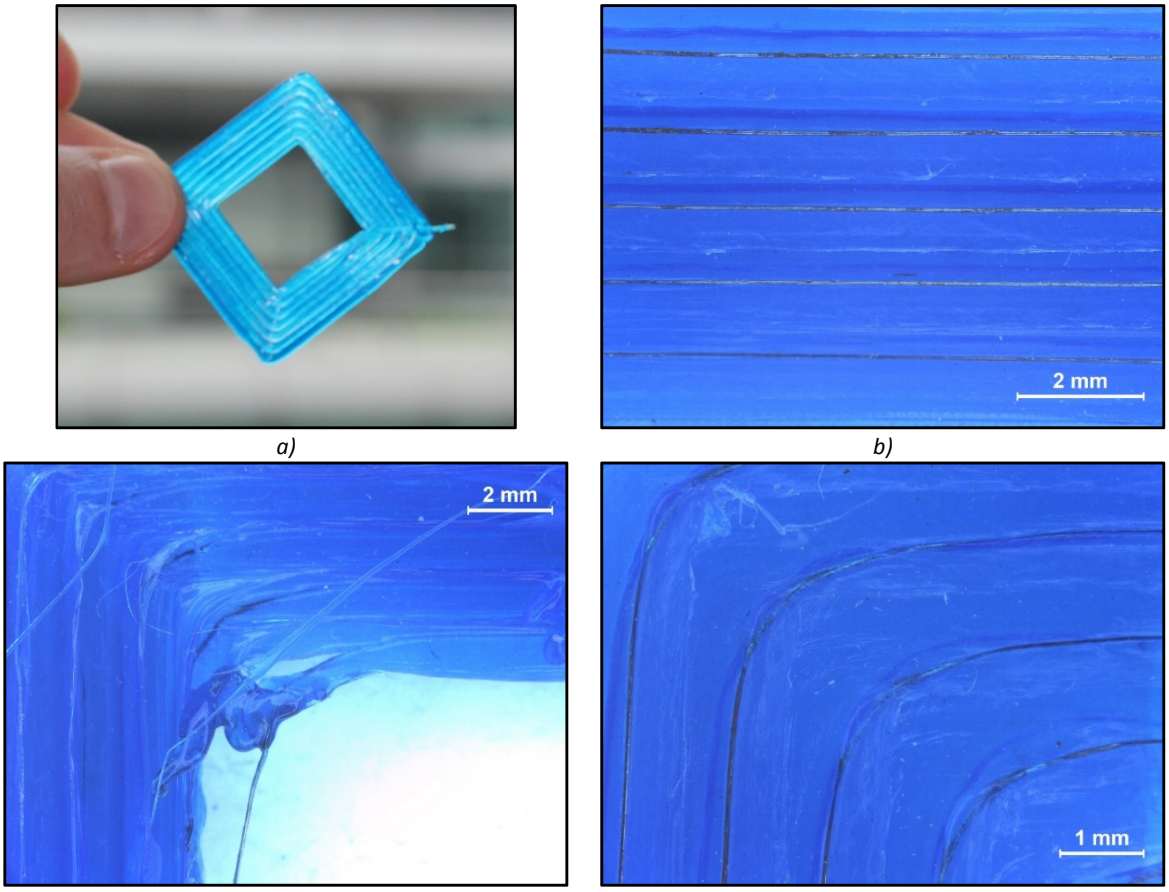

Figure 4-13– RFID Tag Printing Trials

a) Concept Design for Printing RFID Tags. b) Microscopic Image of Linear Section of RFID Tag. c) Material Pull Effect as a Result of Increase Printing Speed. d) Identical Corner to c) Printed at a Lower Speed, Minimising Pull Effect

4.6 THERMAL EXPANSION

As the aim of this work is to produce a concentric coaxial print material to the highest reliable resolution, we must consider the effect which thermal expansion plays on the final product. Any material to be printed in this nozzle will undergo a heating process for printing and a cooling process for post printing. As such, we must consider the temperature gradient

between the molten material and the substrate or environment. Each material has its own unique print temperature as well as its own thermal expansion characteristics.

The typical scenario of heat causes expansion and cold causes contraction plays an unusual role in the case of FDM systems. Typically, the heated material would be expected to decrease in size as it cools, and this will still be the case. The additional factor is the nature of the extrusion process for the material being produced. As the process involves a polymer undergoing temperature change through an extrusion die, it is expected that die swelling will influence the volume of the material immediately post-printing. The key factor is to understand the ratio of thermal expansion against die swelling.

Taking PLA as the test material and applying thermal expansion formula for the area as shown below:

$$\frac{\Delta Area}{Area_o} = \alpha \times \Delta T \tag{4.3}$$

Where

$\Delta Area = Change\ in\ area\ (mm^2)$

$Area_o = Initial\ area\ (mm^2)$

$\alpha = Thermal\ coefficient\ of\ expansion. 7.4e^{-4} (^oC^{-1})$

$\Delta T = Change\ in\ temperature. (^o\mathrm{C})$

Assuming an initial temperature of 200°C, and a final temperature of 25°C, Eq.4.3 is applied to both the internal and external nozzle diameters. This results in the output material diameters decreasing to 26.8µm and 59.9µm for the internal and external materials, respectively. Compounding this value for the internal decreases with the measured value average from Section 4.2 suggests that die swelling may account for a 78µm difference in diameter instead of the 51µm measured which suggests that the die swelling effect may be hiding these changes

in area. This implies that the swelling factor is significantly influential on coaxial extrusion with research into die-swelling within FDM systems identifying a 1.05-1.3 swell ratio dependent upon the material used for printing[71].

This thermal expansion calculation has been used as a guide and will likely vary in practical application for the coaxial nozzle design. As the molten plastic pass from the heat chamber towards the tip, the material is slowly being cooled. The titanium alloy used to fabricate the coaxial nozzle exhibits suitable thermal conduction properties, though it is still anticipated that levels of heat loss are present as the distance from the heat chamber increases. This results in a lower change in temperature for the thermal expansion calculations, indicating that the calculated values would be the extreme conditions.

5 CONCLUSIONS AND RECOMMENDATIONS FOR FUTURE RESEARCH

This thesis has aimed to enhance the variability of structures which can be produced through means of fused deposition modelling. To do so, to the best of our knowledge, one of the first documented coaxial fused deposition modelling systems was designed and constructed, offering a wide range of control over the process. Five key milestones have been realised to measure the success of the work produced. Firstly, a coaxial extrusion tip has been produced capable of accepting standard 3mm thermoplastic filament while having output dimensions of 1200µm and 400µm for the external and internal materials, respectively. Secondly, the reliability of the coaxial tip has been enhanced by optimising its flow parameters and obtaining average coaxial offsets lower than the literature value of 22%. Thirdly, this work aimed to reach a peak operating temperature of 275^{o}C to maximise the range of materials to be used in the system. Milestone four and five are paired, aiming to produce a secondary coaxial extrusion tip to facilitate pre-formed fibres into the FDM process and subsequently produce multi-layer conductive structures.

The first and second milestones are intertwined in their accomplishment. The coaxial extrusion tip has been designed using CAD software; with the associated flow characteristics simulated using a CFD package. This process was iterative as the aim was to obtain a uniform flow for the external material; a task which resulted in a high coaxial axis offset accuracy. With the model optimised for its flow characteristics, the design was realised using an additive fabrication process. Due to complex internal geometry, the component could not be manufactured by traditional methods and so was produced from a titanium alloy powder (Ti6Al4V) using an SLM system. The resultant coaxial nozzle exhibited output diameters of 1200µm and 400µm for the

external and internal materials, respectively, therefore successfully completing the first milestone.

The subsequent task to obtain high levels of accuracy in coaxial concentricity was measured when the custom FDM system had been assembled. The coaxial extrusion process operated at the fluid flow-rates as used in the CFD simulations used to produce the nozzle. For simplicity of the testing procedure, both the internal and external materials were PLA, requiring temperatures of 200^{o}C for printing. This process produced coaxial structures with high levels of coaxial concentricity, a process measured by determining the distance between the longitudinal axes for both internal and external materials. The results indicated that the process is capable of extruding coaxial fibres with an axis offset as low as 2.89%, significantly lower than the literature value of 22%. Achieving such accuracy indicates that the second milestone, too, has been completed successfully.

The third task was to maximise the temperature range for the designed device, increasing the potential materials it could accept. To do this, a Joule heating system was implemented, altering heating coil length to create a sufficiently high maximum temperature while drawing limited amperes. The finished coaxial nozzle is capable of reaching temperatures of 275^{o}C for both heat chambers, indicating that the third milestone has been accomplished successfully; however materials have only been printed requiring temperatures of 260^{o}C.

Milestone four required the design and production of an additional coaxial tip which would allow the introduction of pre-formed materials into an FDM process. To do this, an iterative process was employed, refining CAD models to obtain uniform velocity distributions for sheath material fluid flow using CFD. The design allowed a pre-fabricated core material to be encapsulated within a printed sheath. The core material was passively driven through an entrainment process from the external material fluid flow. As a result of the intricate internal geometry required, the coaxial coating tip was fabricated in Ti6Al4V using an SLM system.

Finally, the fifth milestone required the production of multi-layer coaxially coated conductive pathways. This was successfully achieved through a calibration process of the assembled technology and coaxial tip designed in milestone four. The produced multi-layer structure was a cube, 10 layers in height, which exhibited conductive continuity through the entire structure. This implied that the conductive core had not fractured during the printing process and that a complete circuit had been encapsulated within the sheath material.

With these milestones completed, this work contributes to research in additive fabrication by:

- Enabling the creation of increasingly complex scaffold structures for potential use with biological fabrication development. Allowing a greater range of materials to be printed in a coaxial manner.
- Allowing for construction of fully encapsulated multi-layered structures, providing a reliable system for repeatable use.
- Producing high geometrically accurate extrudate with coaxial concentricity as low as 2.89%.
- Introduce a reliable means of printing multi-layer insulated conductive pathways.

With the goals achieved, and the results obtained, several avenues exist for future work.

- The first potential improvement to the process is to examine additional methods for reducing internal surface roughness. Abrasive blasting and a material purge process proved successful for the post fabrication processing of the current coaxial tip. Improvements to the method would involve decreasing the diameters for both the internal and external materials, achieving a higher print resolution. This creates an issue as chambers which were currently designed to be 200µm will be decreased in size, increasing the chance of titanium powder adhesions forming a blockage in the fabrication process. Therefore, a new post fabrication processing technique to reduce

surface roughness would greatly enhance the likelihood of success if smaller tip dimensions were to be produced.

- Alternatively, another option for achieving decreased internal surface roughness would be to source finer particle sizes for the Ti6Al4V powder used to fabricate the coaxial tip. This would reduce the size of the partially bound particle adhesions, reducing the potential of the SLM process from creating an internal blockage.
- Additionally, the alignment and coaxial concentricity of multi-layer structures has opportunity to be improved. The device was calibrated during its design process, though additional modifications to the parameters would likely produce an improved coaxial structure. The calibrated layer height, feed-rate and flow-rate must be altered to obtain this improvement. Due to the compressive nature of FDM printing, the fibres may not become significantly more concentric than those produced, though the repeatability can be enhanced.
- Subsequent research into the realm of coaxial fused deposition modelling should look to modifying an existing coaxial fibre system to allow the core material to be deposited as a percentage of its full value. This process will produce FGMs within a sheathed environment, offering great potential to the biomedical industry for gradient based drug delivery processes.

APPENDIX A – COMPONENT DATASHEETS

NEMA 17 Stepper Motor Datasheet [72]

MOTION CONTROL PRODUCTS LTD

1.8° Size 42mm High Torque Hybrid Stepping Motor

- **General Specification for High Torque Hybrid Stepping Motor**

Item	Specifications
Step Angle	1.8°
Step Angle Accuracy	± 5% (full step, no load)
Resistance Accuracy	± 10%
Inductance Accuracy	± 20%
Temperature Rise	80℃ Max.(rated current,2 phase on)
Ambient Temperature	-20℃~+50℃
Insulation Resistance	100M Ω Min. ,500VDC
Dielectric Strength	500VAC for one minute
Shaft Radial Play	0.02Max. (450 g-load)
Shaft Axial Play	0.08Max. (450 g-load)
Max. radial force	28N (20mm from the flange)
Max. axial force	10N
Rotation	CW(See from Front Flange)

- **Size 42mm High Torque Hybrid Stepping Motor Specifications**

Model No.		Rated Voltage	Current /Phase	Resistance /Phase	Inductance /Phase	Holding Torque	# of Leads	Rotor Inertia	Weight	Detent Torque	Length
Single Shaft	Double Shaft	V	A	Ω	mH	Kg-cm		g-cm²	kg	g-cm	mm
FL42STH25-0404A	FL42STH25-0404B	9.6	0.4	24	36	1.7	4	20	0.15	200	25
FL42STH33-0404A	FL42STH34-0404B	12	0.4	30	37	2.5	4	38	0.2	120	34
FL42STH33-0956A	FL42STH34-0956B	3.99	0.95	4.2	2.8	1.6	6				
FL42STH33-0476A	FL42STH34-0476B	6.392	0.47	13.6	9.8						
FL42STH38-0406A	FL42STH38-0406B	12	0.4	30	24	2.5	6	57	0.24	150	40
FL42STH38-0804A	FL42STH38-0804B	8	0.8	10	17	3.2	4				
FL42STH38-1206A	FL42STH38-1206B	3.96	1.2	3.3	2.4	2.4	6				
FL42STH38-0806A	FL42STH38-0806B	6.0	0.8	7.5	7.0	2.8					
FL42STH47-1006A	FL42STH48-1006B	4.6	1.0	4.6	4.0	3.4	6	82	0.34	200	48
FL42STH47-0406A	FL42STH48-0406B	12	0.4	30	28	3.8					
FL42STH47-1204A	FL42STH48-1204B	3.84	1.2	3.2	6.0	4.5	4				
FL42STH47-0854A	FL42STH48-0854B	5.61	0.85	6.6	11						

- **Dimension**

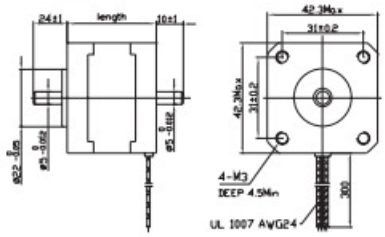

Wiring Diagram

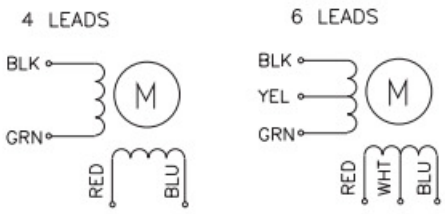

TEL: +44(0) 1202 599922 Email: sales@motioncontrolproducts.com
FAX: +44(0) 1202 599955 Home Page: www.motioncontrolproducts.com

14

SPDT Microswitch Datasheet [73]

MINIATURE SWITCHES

Ultra Miniature Microswitches

- Rating 3A switching S.P.D.T.
- Space saving

CSMU01

SPECIFICATION		
Rating		3A/125VAC
Contact resistance		50mΩ max
Insulation strength		100MΩ min/500VDC
Electrical Life		10,000 operations min
Temperature range		-10°C to +85°C
Material	Case	PBT
	Button	PBT
	Actuator	Stainless steel
	Contacts	AgNi10
Terminals		Brass alloy H65 Silver Plated

	ACTUATOR STYLE	OPERATING FORCE MAX	RELEASE FORCE MAX	OPERATING POSITION	PRE TRAVEL MAX	MOVEMENT DIFFERENTIAL	OVER TRAVEL MIN
CSMU0100	Button	1.5N	0.08N	5.5 ± 0.3mm		0.2mm	0.2mm
CSMU0101	Tapered Lever	0.23N	0.03N	6.2 ± 0.8mm		0.7mm	0.7mm
CSMU0106	Parallel Lever	0.23N	0.03N	7 ± 1.2mm		0.7mm	0.7mm
CSMU0140	Simulated Roller	0.4N	0.05N	8.2 ± 1.5mm	4.2mm	0.9mm	0.9mm

Types of Actuator:

Button

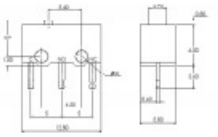

Tapered Lever

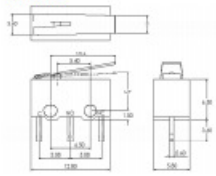

Parallel Lever

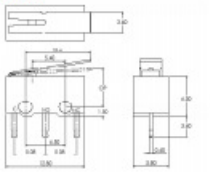

Simulated Roller

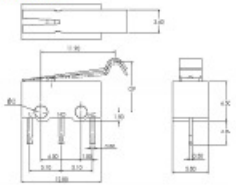

CSMU01 Series Replaces CSSM Series
Example CSMU0100 replaces CSSM100
ExampleCSMU0140 replaces CSSM030C

+44 (0)1638 716101
info@camdenboss.com
www.camdenboss.com

We operate a constant improvement policy, our products are subject to change without notice.

Ver 1.0

CAMDENBOSS ELECTRONICS & ENCLOSURES

204-GT 2 High Temperature Thermistor [74]

HIGH HEAT-RESISTANCE AND HIGH SENSITIVE THERMISTOR

GT THERMISTOR

GT thermistor is combined both superior feature of BT thermistor and ET thermistor as fast response time, high reliability, wide category temperature range, high moisture proof, high accuracy and reasonable price.
GT thermistor is made up of a high quality thermistor element and the lead wire is connected to the thermistor element by alloyed technology, and glass coating for the thermistor element.

Time constant

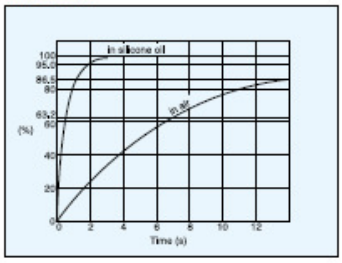

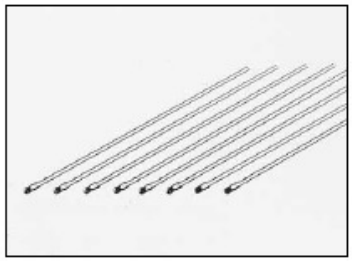

Part number

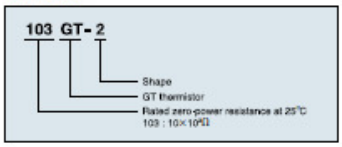

Dimensions

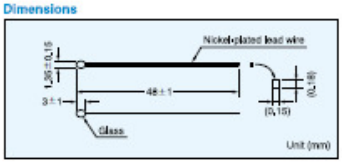

Specifications

Part No.	R_{25}*1	B value*2	Dissipation factor (mW/°C) Approx.	Thermal time constant(s)*3 Approx.	Rated maximum power dissipation (at 25°C)(mW)	Category temp. range(°C)
102GT-2	1,0kΩ±3%	3305K±2%				−50~+200
202GT-2	2,0kΩ±3%	3838K±2%				
502GT-2	5,0kΩ±3%	3964K±2%				
103GT-2	10,0kΩ±3%	4126K±2%				
203GT-2	20,0kΩ±3%	4282K±2%				
503GT-2	50,0kΩ±3%	4288K±2%	0.6	7	3.0	−50~+300
104GT-2	100,0kΩ±3%	4267K±2%				
104GTA-2	100,0kΩ±3%	4390K±2%				
204GT-2	200,0kΩ±3%	4338K±2%				
504GT-2	500,0kΩ±3%	4526K±2%				
105GT-2	1000,0kΩ±3%	4608K±2%				

Specifications

Part No.	Rated zero-power resistance temperature*1 (°C)	Rated zero-power resistance resistance	Rated zero-power resistance tolerance	temperature (°C)	B value*2	Dissipation factor (mW/°C) Approx.	Thermal time constant(s)*3 Approx.	Rated Electricity mW at 25°C	Category temp. range(°C)
252GT-2-20185	0	6kΩ	±5%	0/100	3390K±2%				
252GT-❷-20197	25	2,5kΩ	±2,5%						
262GT-❷-20198	0	8kΩ	±1%	25/50	3745K±2%				
542GT-❷-20184	75	0.7331kΩ	±3%	0/100	3450K±2%				
542GT-❷-20186	0	15kΩ	±3%						
852GT-❷-20156	50	3,485kΩ	±3%						
103GT-2-20196	25	10kΩ	±1%	25/85	3435K±1%				
103GTA-2-20199	25	10kΩ	±5%	25/125	3980K±2%				
303GT-2-20205	25	30kΩ	±3%	0/100	3970K±2%	0.6	7	3.0	−50~+300
333GT-❷-20204	125	1,509kΩ	±3%	0/100	3570K±2%				
493GT-❷-20157	5	127kΩ	±2%	0/100	3970K±2%				
493GT-❷-20159	75	7.214kΩ	±3%						
493GT-❷-20188	40	26.06kΩ	±2%						
104GT-❷-20201	25	100kΩ	±3%	100/200	4300K±3%				
234GT-❷-20194	25	231,44kΩ	±3%	100/200	4537K±1%				
234GT-2-20195	150	3,161kΩ	±3%		4537K±2%				
145GT-2-20203	200	4kΩ	±5%	200/300	5133K±3%				

*1 Rated zero-power resistance at each temperature.
*2 B value : determined by rated zero-power resistance at each temperature.
*3 Time when thermistor reaches 63.2% of the temperature difference. The value is measured in the air.

APPENDIX B – MICROCONTROLLER SCHEMATICS

Arduino Mega 2560 Pin Configurations [75]

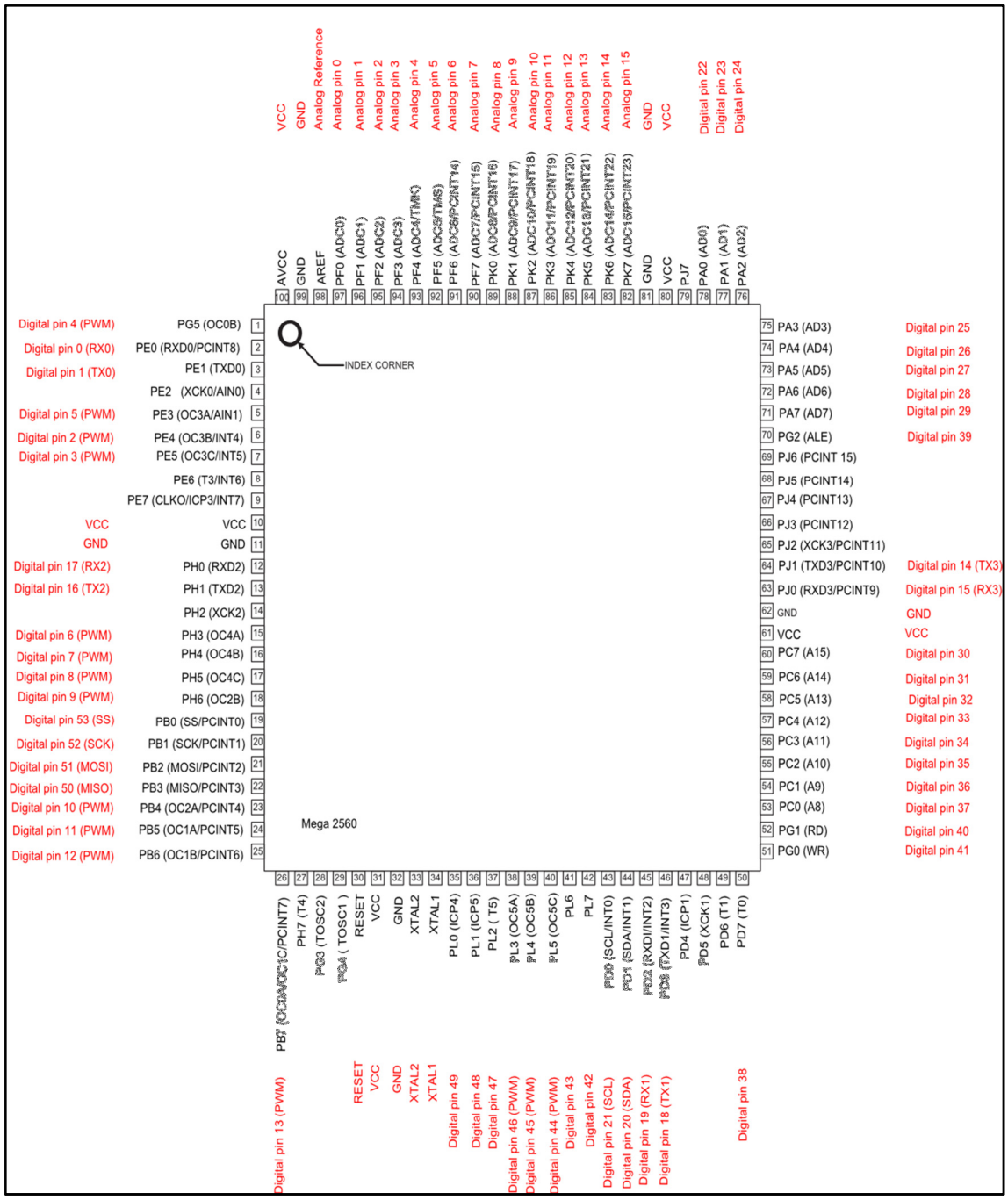

Arduino Mega 2560 Pin Mapping [75]

Pin Number	Mapped Pin Name	Pin Number	Mapped Pin Name
1	Digital pin 4 (PWM)	51	Digital pin 41
2	Digital pin 0 (RX0)	52	Digital pin 40
3	Digital pin 1 (TX0)	53	Digital pin 37
4		54	Digital pin 36
5	Digital pin 5 (PWM)	55	Digital pin 35
6	Digital pin 2 (PWM)	56	Digital pin 34
7	Digital pin 3 (PWM)	57	Digital pin 33
8		58	Digital pin 32
9		59	Digital pin 31
10	VCC	60	Digital pin 30
11	GND	61	VCC
12	Digital pin 17 (RX2)	62	GND
13	Digital pin 16 (TX2)	63	Digital pin 15 (RX3)
14		64	Digital pin 14 (TX3)
15	Digital pin 6 (PWM)	65	
16	Digital pin 7 (PWM)	66	
17	Digital pin 8 (PWM)	67	
18	Digital pin 9 (PWM)	68	
19	Digital pin 53 (SS)	69	
20	Digital pin 52 (SCK)	70	Digital pin 39
21	Digital pin 51 (MOSI)	71	Digital pin 29
22	Digital pin 50 (MISO)	72	Digital pin 28
23	Digital pin 10 (PWM)	73	Digital pin 27
24	Digital pin 11 (PWM)	74	Digital pin 26
25	Digital pin 12 (PWM)	75	Digital pin 25
26	Digital pin 13 (PWM)	76	Digital pin 24
27		77	Digital pin 23
28		78	Digital pin 22
29		79	
30	RESET	80	VCC
31	VCC	81	GND
32	GND	82	Analog pin 15
33	XTAL2	83	Analog pin 14
34	XTAL1	84	Analog pin 13
35	Digital pin 49	85	Analog pin 12
36	Digital pin 48	86	Analog pin 11
37	Digital pin 47	87	Analog pin 10
38	Digital pin 46 (PWM)	88	Analog pin 9
39	Digital pin 45 (PWM)	89	Analog pin 8
40	Digital pin 44 (PWM)	90	Analog pin 7
41	Digital pin 43	91	Analog pin 6
42	Digital pin 42	92	Analog pin 5
43	Digital pin 21 (SCL)	93	Analog pin 4
44	Digital pin 20 (SDA)	94	Analog pin 3
45	Digital pin 19 (RX1)	95	Analog pin 2
46	Digital pin 18 (TX1)	96	Analog pin 1
47		97	Analog pin 0
48		98	Analog Reference
49		99	GND
50	Digital pin 38	100	VCC

RAMPS 1.4 Connector Diagram

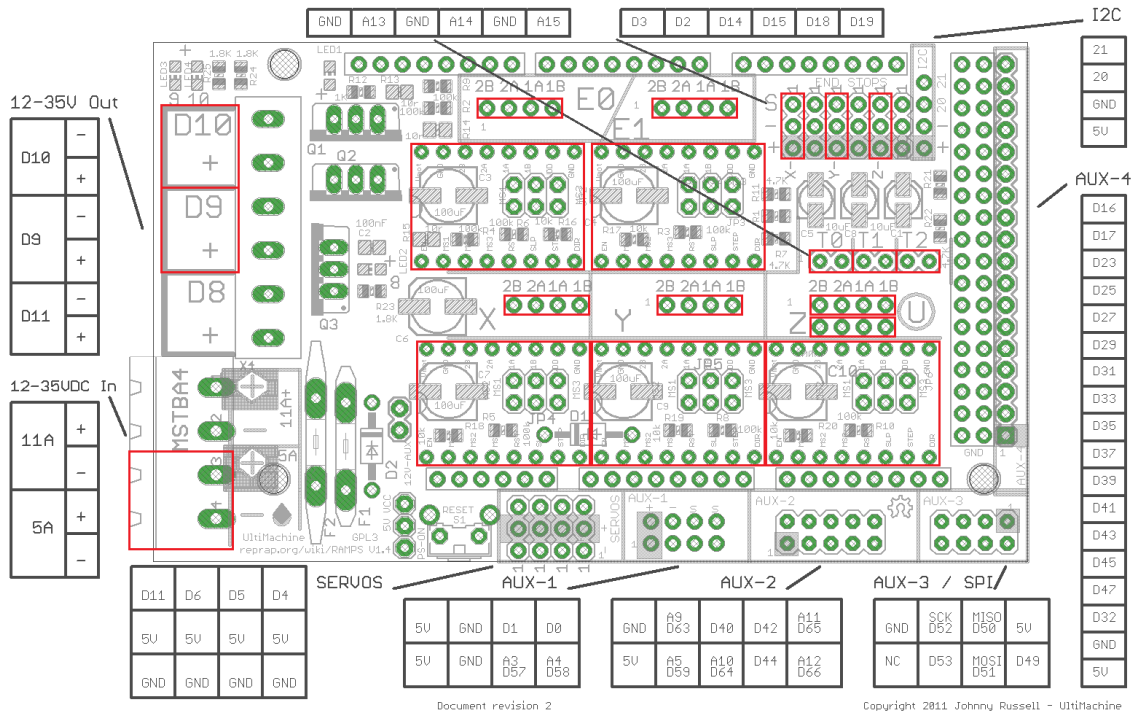

Pololu - A4988 Stepper Motor Driver Datasheet [76]

A4988

DMOS Microstepping Driver with Translator and Overcurrent Protection

Pin-out Diagram

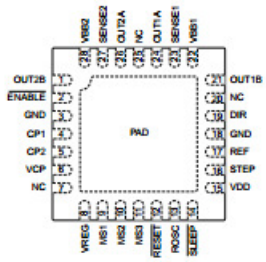

Terminal List Table

Name	Number	Description
CP1	4	Charge pump capacitor terminal
CP2	5	Charge pump capacitor terminal
VCP	6	Reservoir capacitor terminal
VREG	8	Regulator decoupling terminal
MS1	9	Logic input
MS2	10	Logic input
MS3	11	Logic input
$\overline{\text{RESET}}$	12	Logic input
ROSC	13	Timing set
$\overline{\text{SLEEP}}$	14	Logic input
VDD	15	Logic supply
STEP	16	Logic input
REF	17	G_m reference voltage input
GND	3, 18	Ground*
DIR	19	Logic input
OUT1B	21	DMOS Full Bridge 1 Output B
VBB1	22	Load supply
SENSE1	23	Sense resistor terminal for Bridge 1
OUT1A	24	DMOS Full Bridge 1 Output A
OUT2A	26	DMOS Full Bridge 2 Output A
SENSE2	27	Sense resistor terminal for Bridge 2
VBB2	28	Load supply
OUT2B	1	DMOS Full Bridge 2 Output B
$\overline{\text{ENABLE}}$	2	Logic input
NC	7, 20, 25	No connection
PAD	–	Exposed pad for enhanced thermal dissipation*

*The GND pins must be tied together externally by connecting to the PAD ground plane under the device.

Allegro MicroSystems, Inc.
115 Northeast Cutoff
Worcester, Massachusetts 01615-0036 U.S.A.
1.508.853.5000; www.allegromicro.com

APPENDIX C – TECHNICAL DRAWINGS

Feed Mechanism – Housing

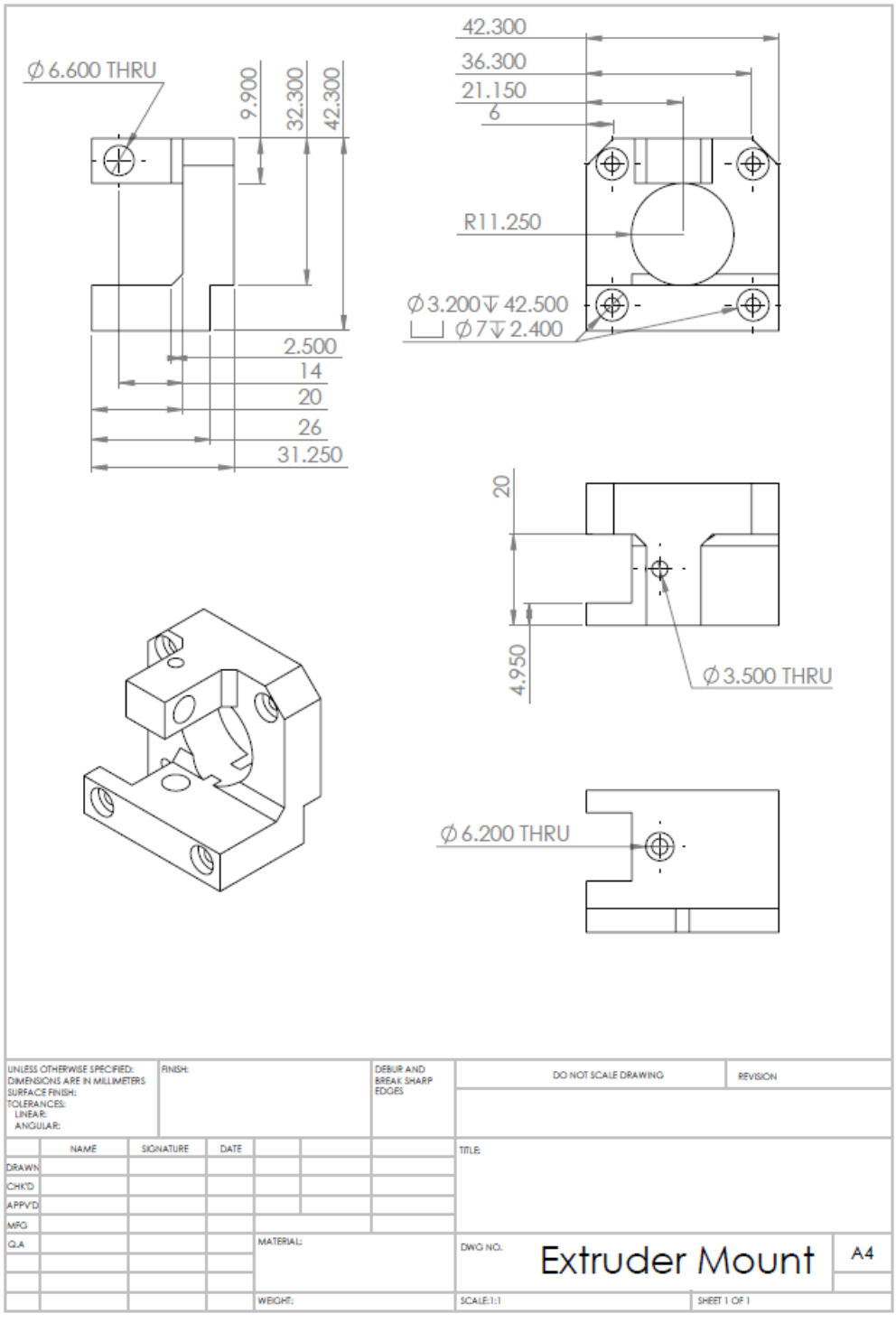

Feed Mechanism – Bracket

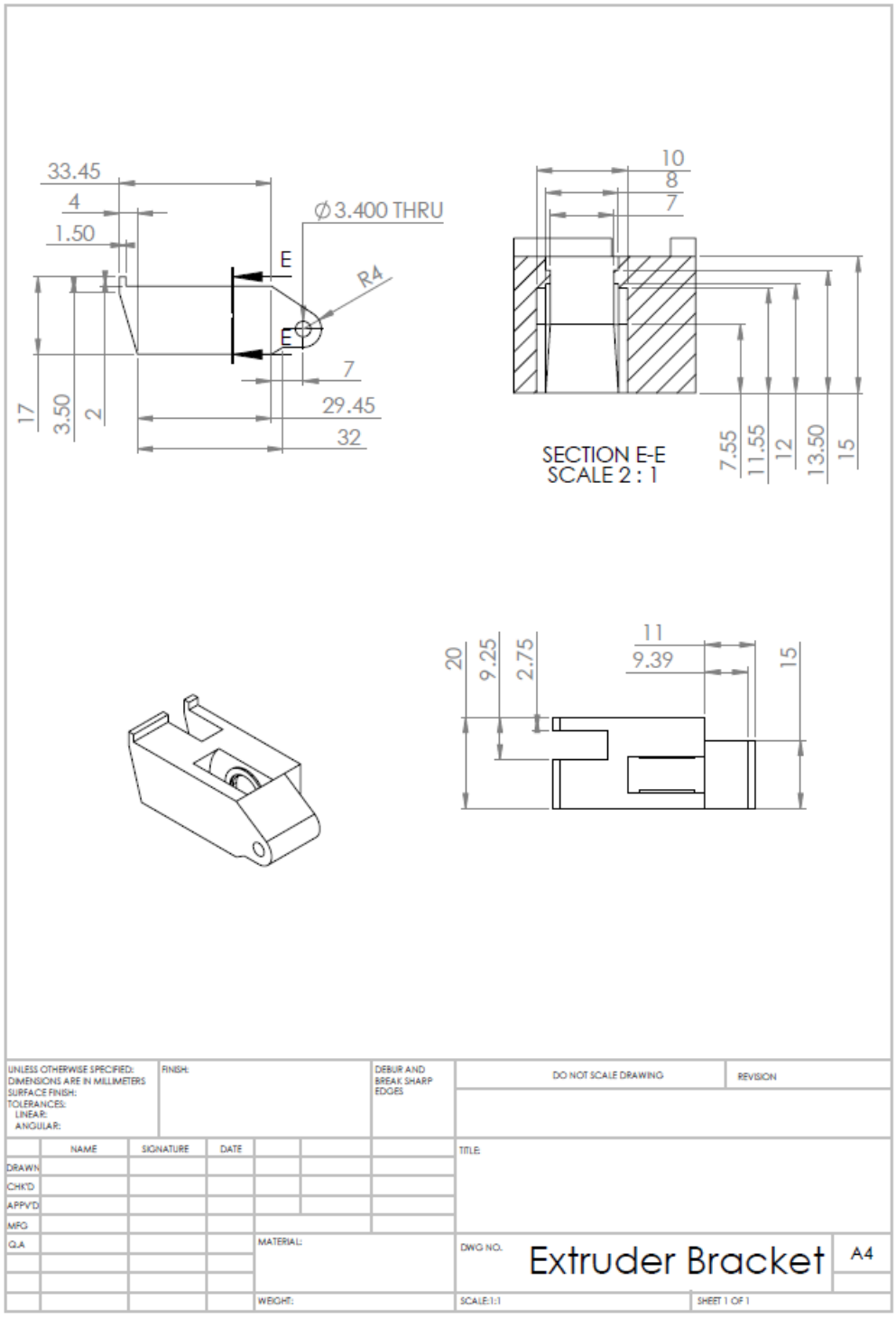

PEEK Collar

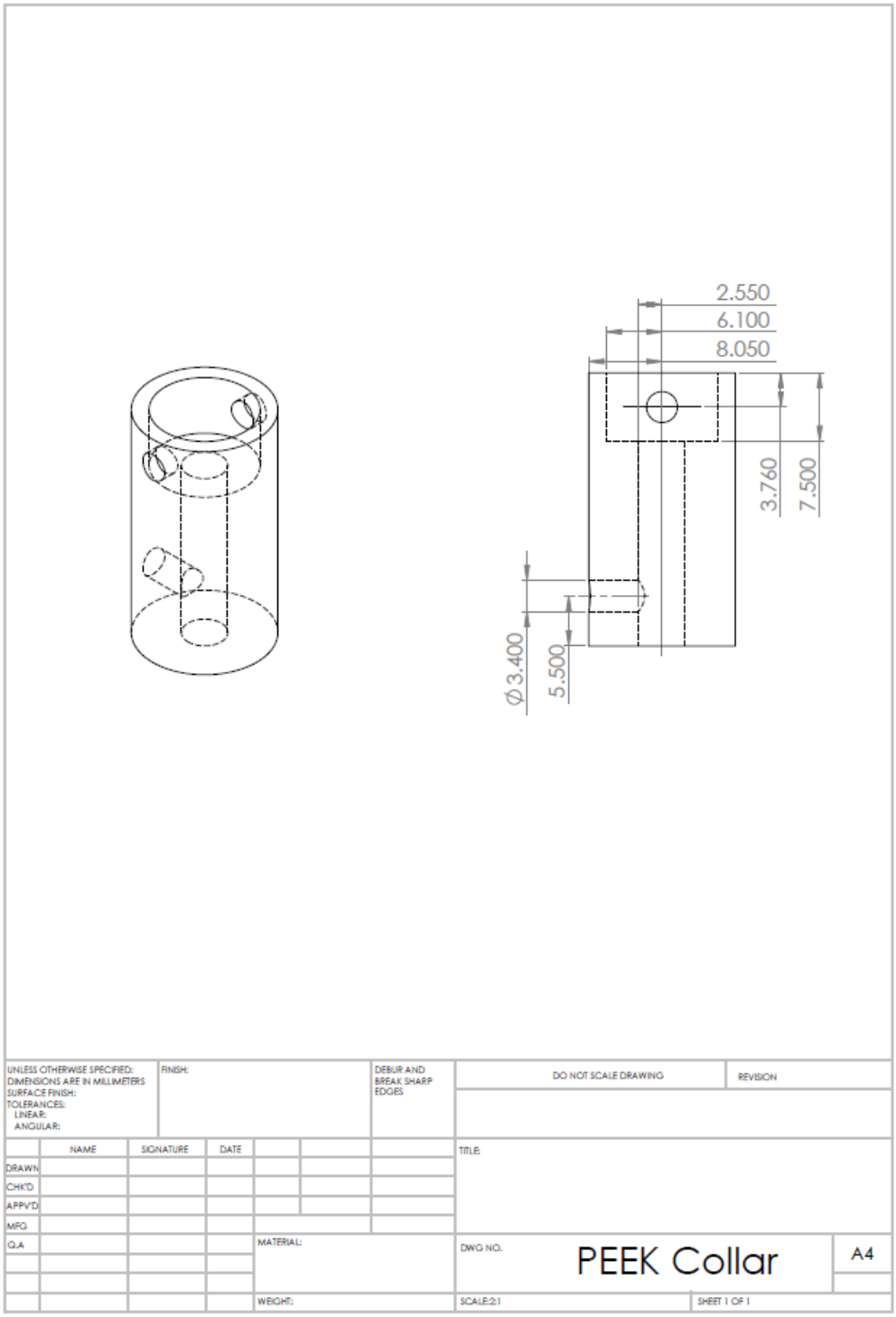
2.550
6.100
8.050
3.760
7.500
Ø3.400
5.500
UNLESS OTHERWISE SPECIFIED:
DIMENSIONS ARE IN MILLIMETERS
SURFACE FINISH:
TOLERANCES:
LINEAR:
ANGULAR:
FINISH:
DEBUR AND BREAK SHARP EDGES
DO NOT SCALE DRAWING
REVISION
NAME
SIGNATURE
DATE
DRAWN
CHK'D
APPV'D
MFG
Q.A
TITLE:
MATERIAL:
DWG NO.
PEEK Collar
A4
WEIGHT:
SCALE:2:1
SHEET 1 OF 1

Microswitch Mounting Bracket

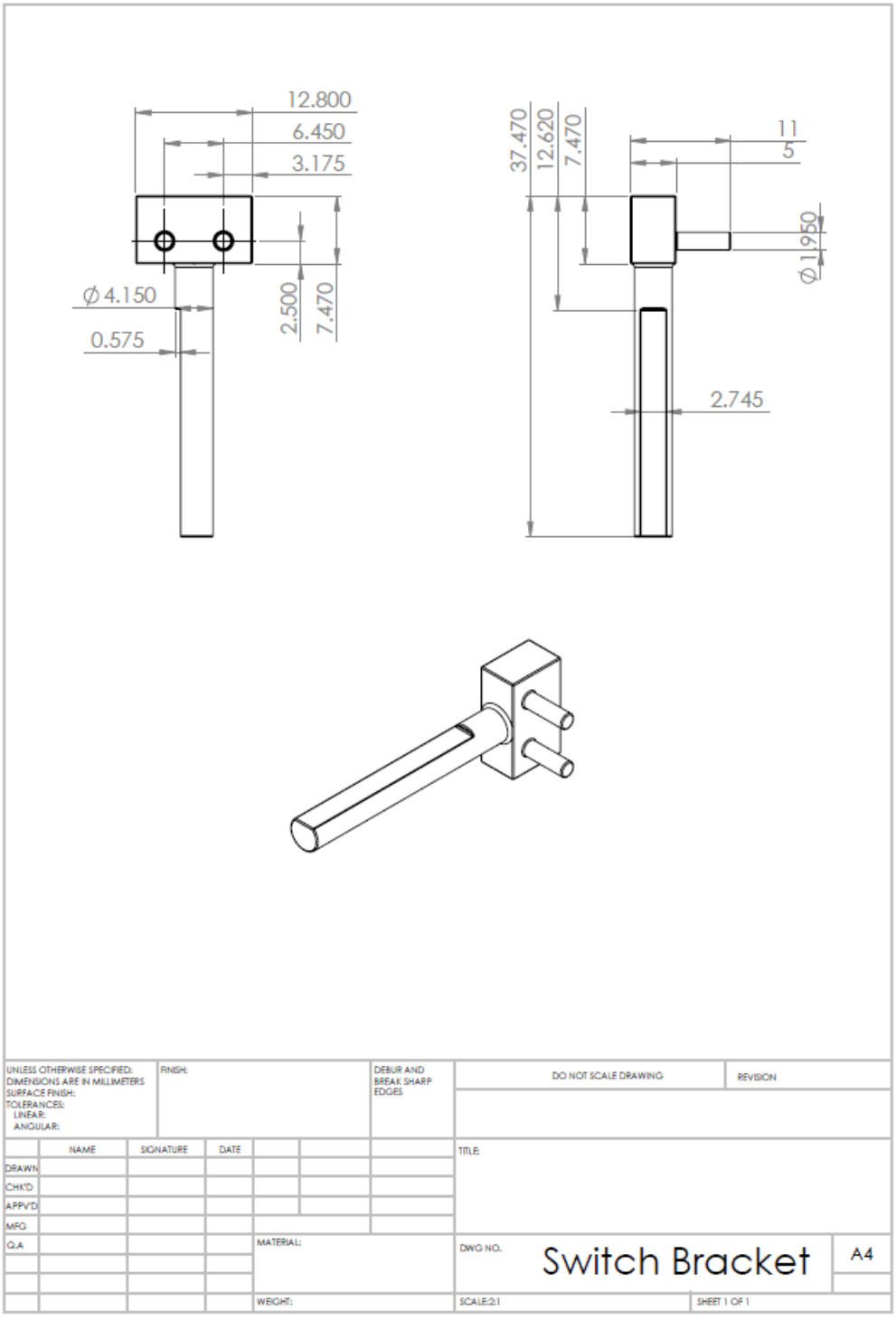

Extruder Housing 1

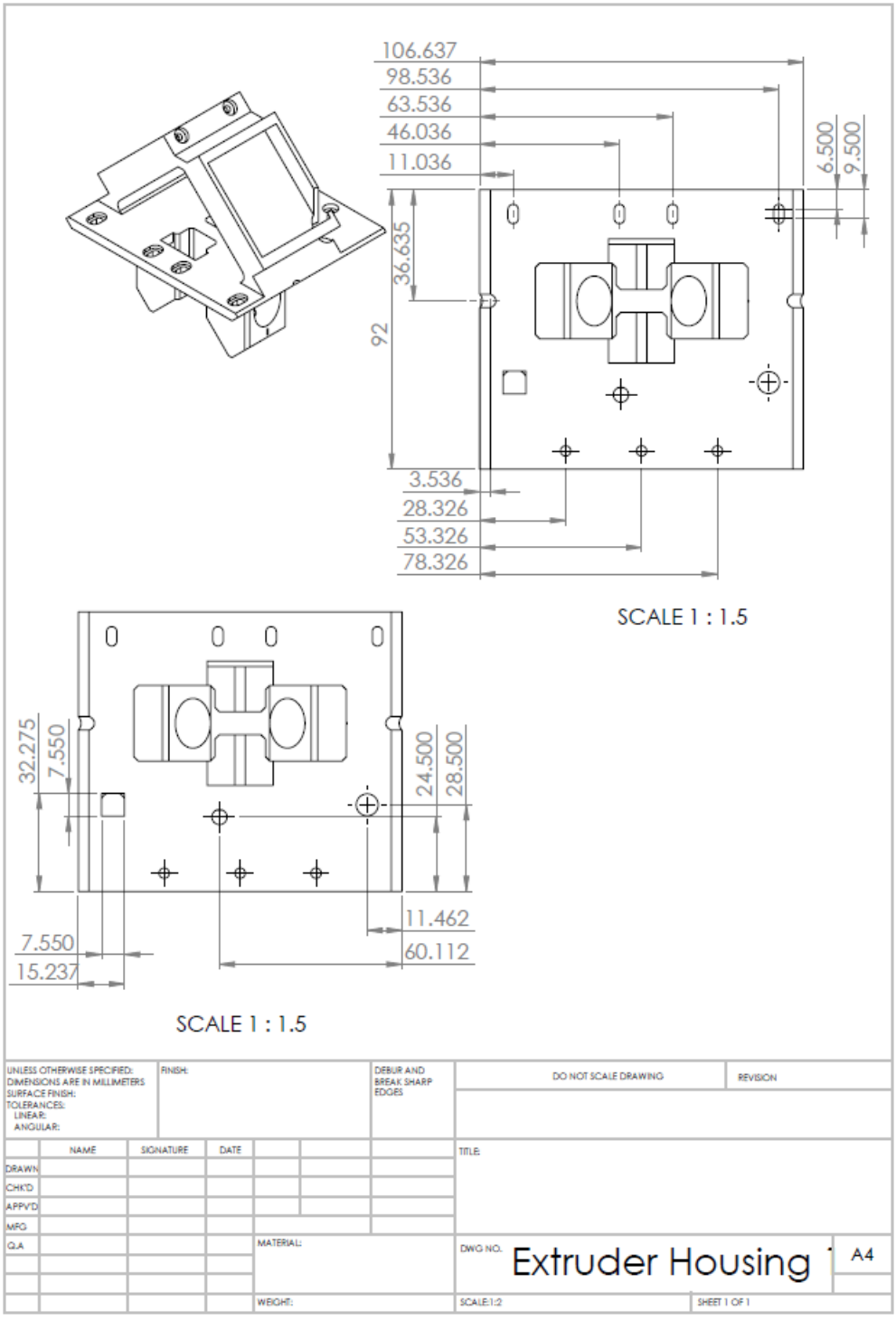

Extruder Housing 2

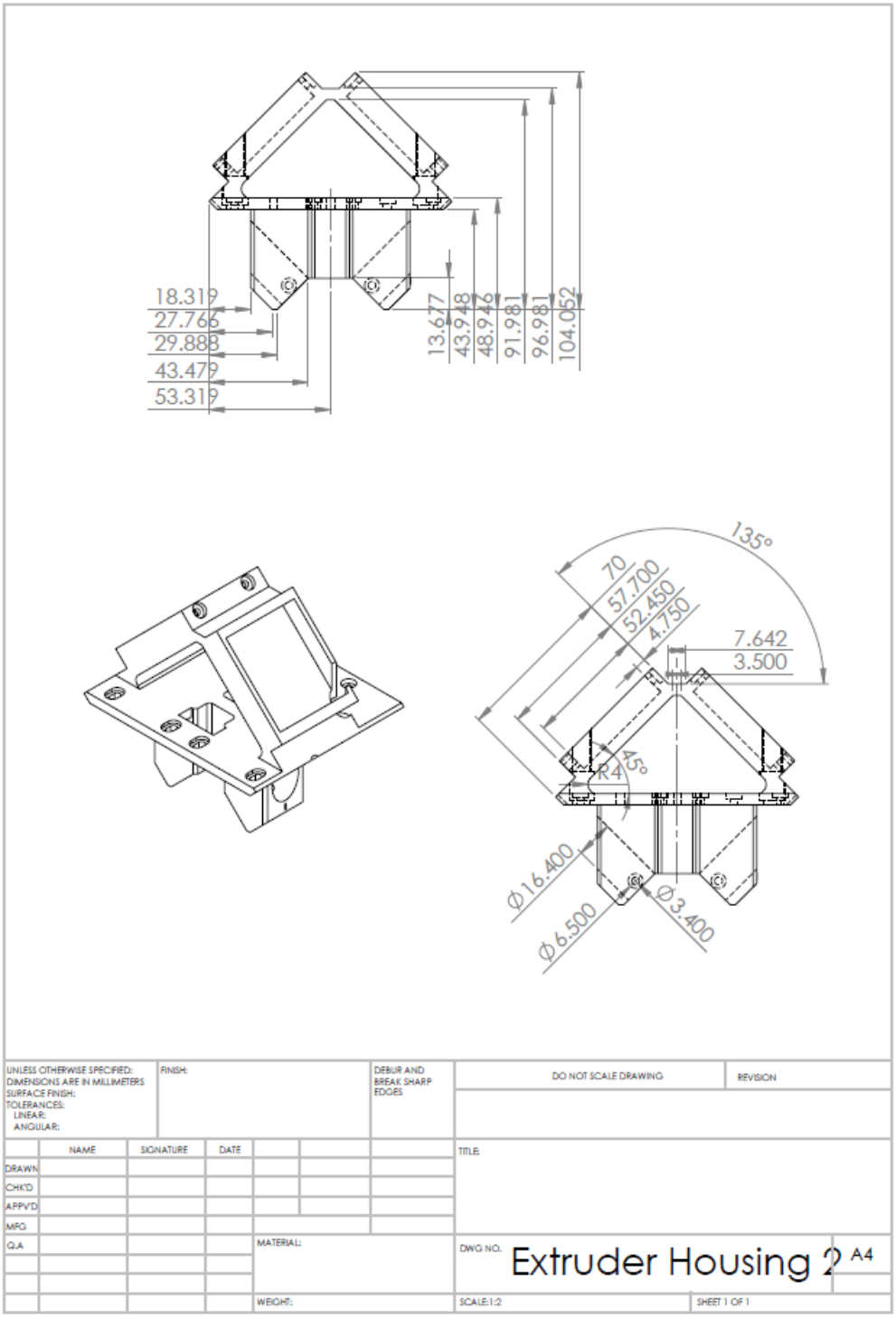

Extruder Housing 3

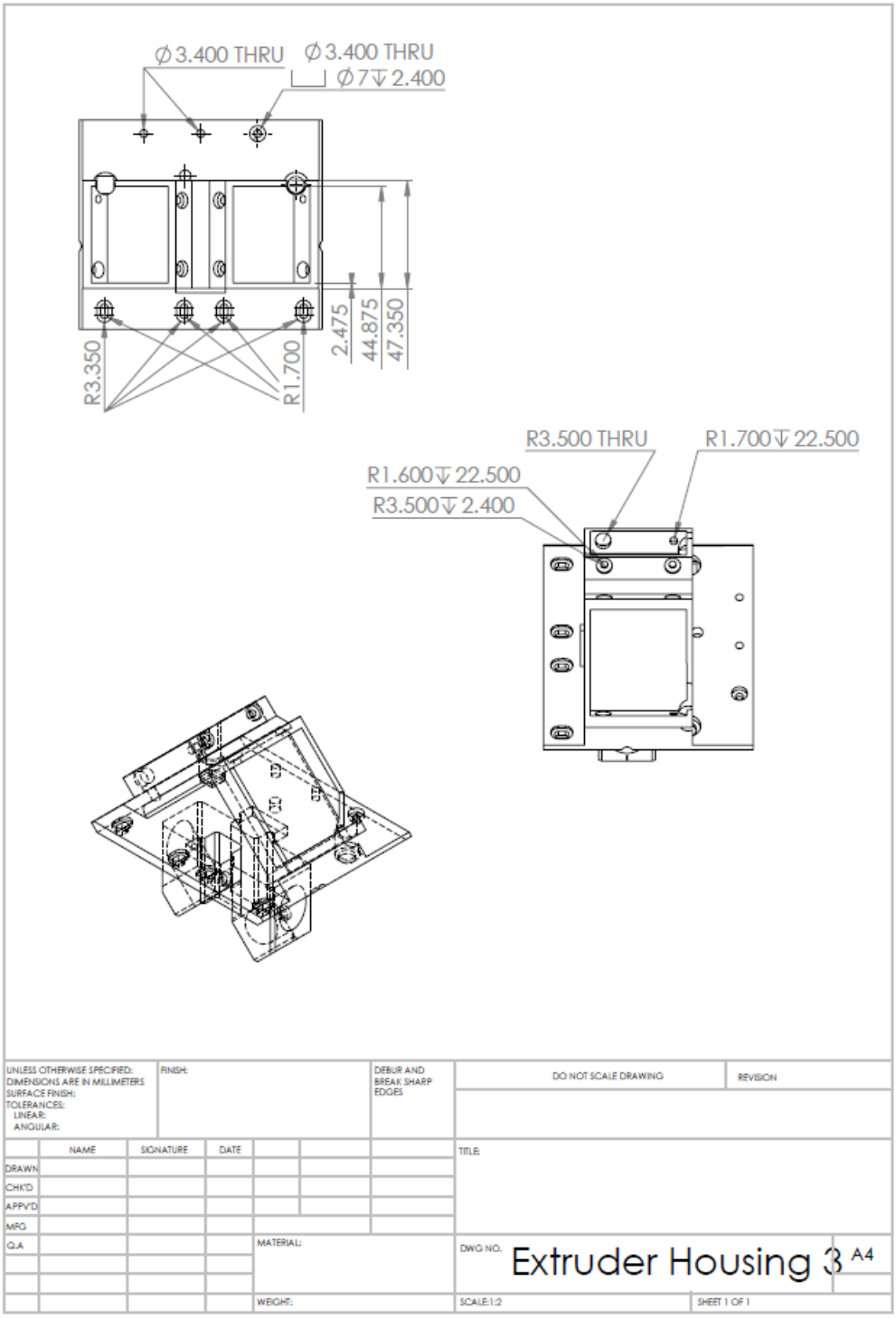

Perspex Print Bed

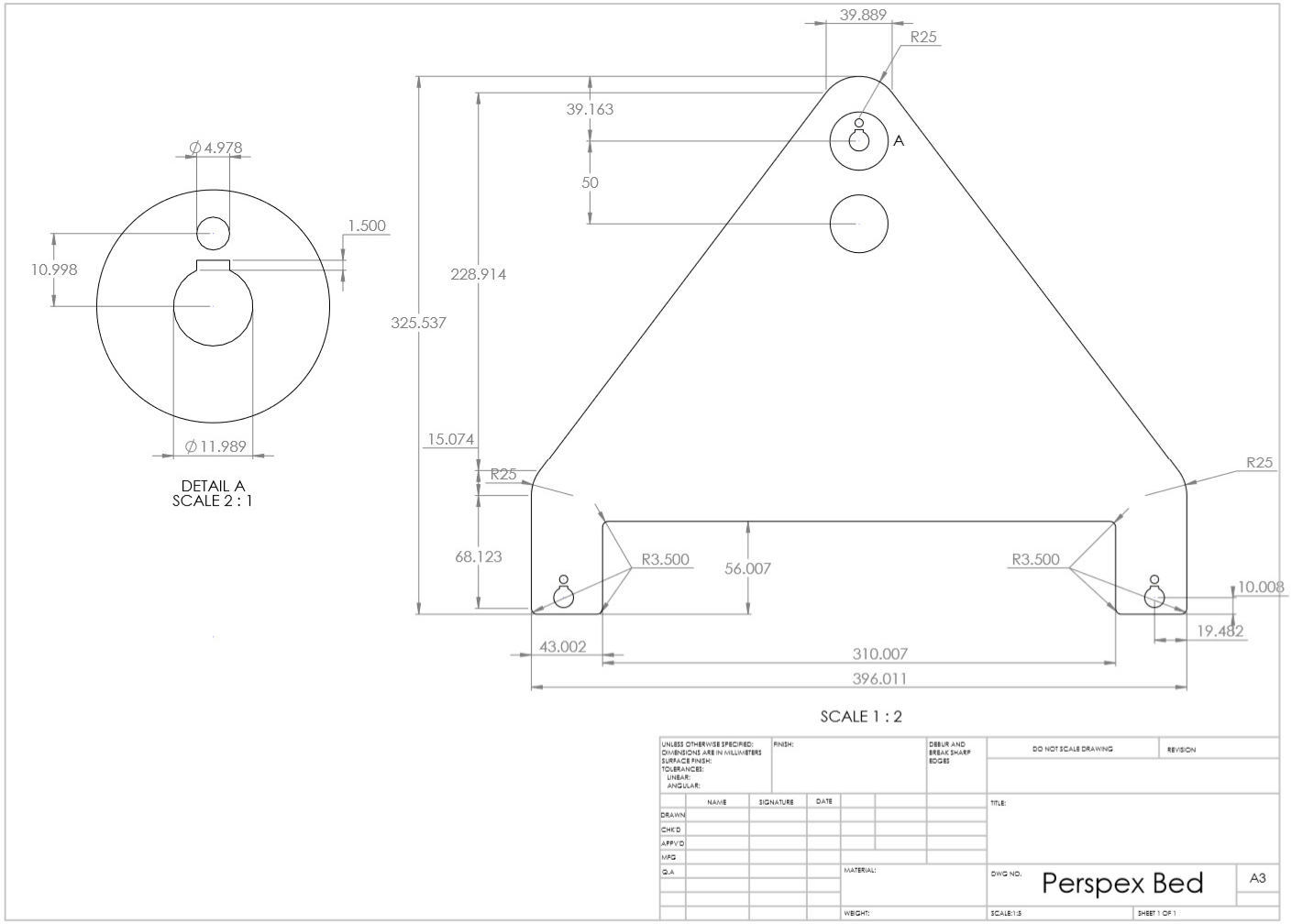

APPENDIX D –SIMULATION PARAMETERS

	ABS[77]	PLA[78-80]	Ti6Al4V[81]
Molar Mass (kg/mol)*	0.211	0.0721	0.446
Density (kg/m^3)	1060	1251	4430
Specific Heat Capacity (J/Kg.K)	1400	1800	0.5263
Dynamic Viscosity (Pa.s)	5	5	N/A
Thermal Conductivity (W/m.K)	0.23	0.11	6.7

* As molar mass cannot be determined for ABS or PLA due to the unknown degree of polymerisation of the materials skeletal structure, a single degree of polymerisation has been selected to represent each material.

REFERENCES

1. Campbell, T., et al., *Could 3D Printing Change the World?* Technologies, Potential, and Implications of Additive Manufacturing. Washington, DC: Atlantic Council, 2011.
2. International, A., *Standard Terminology for Additive Manufacturing Technologies*. 2012, www.astm.org: West Conshohocken, PA.
3. Kruth, J.P., M.C. Leu, and T. Nakagawa, *Progress in Additive Manufacturing and Rapid Prototyping.* CIRP Annals - Manufacturing Technology, 1998. **47**(2): p. 525-540.
4. Hull, C.W., *Apparatus for production of three-dimensional objects by stereolithography*. 1986, Google Patents.
5. Williams, J.C. and E.A. Starke Jr, *Progress in structural materials for aerospace systems.* Acta Materialia, 2003. **51**(19): p. 5775-5799.
6. Petrovic, V., et al., *Additive layered manufacturing: sectors of industrial application shown through case studies.* International Journal of Production Research, 2010. **49**(4): p. 1061-1079.
7. Song, Y., et al., *Manufacture of the die of an automobile deck part based on rapid prototyping and rapid tooling technology.* Journal of Materials Processing Technology, 2002. **120**(1–3): p. 237-242.
8. Al Mortadi, N., et al., *Design and fabrication of a sleep apnea device using computer-aided design/additive manufacture technologies.* Proceedings of the Institution of Mechanical Engineers, Part H: Journal of Engineering in Medicine, 2013. **227**(4): p. 350-355.
9. Hengsbach, S. and A. Lantada, *Rapid prototyping of multi-scale biomedical microdevices by combining additive manufacturing technologies.* Biomedical Microdevices, 2014. **16**(4): p. 617-627.
10. Murr, L.E., et al., *Next-generation biomedical implants using additive manufacturing of complex, cellular and functional mesh arrays.* Philosophical Transactions of the Royal Society A: Mathematical, Physical and Engineering Sciences, 2010. **368**(1917): p. 1999-2032.
11. Ding, Y., et al., *An integrated manufacturing system for rapid tooling based on rapid prototyping.* Robotics and Computer-Integrated Manufacturing, 2004. **20**(4): p. 281-288.
12. Harrysson, O.L.A., et al., *Direct metal fabrication of titanium implants with tailored materials and mechanical properties using electron beam melting technology.* Materials Science and Engineering C: Biomimetic and Supramolecular Systems, 2008. **28**(3): p. 366-373.
13. Leong, K.F., et al., *Characterization of a poly-epsilon-caprolactone polymeric drug delivery device built by selective laser sintering.* Bio-Medical Materials And Engineering, 2007. **17**(3): p. 147-157.
14. Schmidt, M., D. Pohle, and T. Rechtenwald, *Selective Laser Sintering of PEEK.* CIRP Annals - Manufacturing Technology, 2007. **56**(1): p. 205-208.
15. Ramanath, H.S., et al., *Melt flow behaviour of poly-ε-caprolactone in fused deposition modelling.* Journal of Materials Science: Materials in Medicine, 2008. **19**(7): p. 2541-2550.
16. *Design and Production of Wind Tunnel Testing Models with Selective Laser Sintering Technology Using Glass-Reinforced Nylon.* Materials Science Forum, 2007. **532-533**: p. 653-656.

17. Levy, G.N., R. Schindel, and J.P. Kruth, *RAPID MANUFACTURING AND RAPID TOOLING WITH LAYER MANUFACTURING (LM) TECHNOLOGIES, STATE OF THE ART AND FUTURE PERSPECTIVES.* CIRP Annals - Manufacturing Technology, 2003. **52**(2): p. 589-609.
18. Br, et al., *Advanced Material Studies for Additive Manufacturing in terms of Future Gear Application.* Advances in Mechanical Engineering, 2014. **2014**: p. 10.
19. Wong, K.V. and A. Hernandez, *A Review of Additive Manufacturing.* ISRN Mechanical Engineering, 2012. **2012**: p. 10.
20. Bourell, D., et al. *A brief history of additive manufacturing and the 2009 roadmap for additive manufacturing: looking back and looking ahead*. in *US-Turkey Workshop on Rapid Technologies*. 2009.
21. Bechmann, F., *Changing the future of additive manufacturing.* Metal Powder Report, 2014. **69**(3): p. 37-40.
22. Eitel, E., *The future of ADDITIVE MANUFACTURING.* Machine Design, 2013. **85**(3): p. 52-56.
23. Lu, X., et al., *Fine lattice structures fabricated by extrusion freeforming: Process variables.* Journal of Materials Processing Technology, 2009. **209**(10): p. 4654-4661.
24. Leong, K.F., et al., *Engineering functionally graded tissue engineering scaffolds.* Journal of the Mechanical Behavior of Biomedical Materials, 2008. **1**(2): p. 140-152.
25. Guo, N. and M. Leu, *Additive manufacturing: technology, applications and research needs.* Frontiers of Mechanical Engineering, 2013. **8**(3): p. 215-243.
26. Westberg, H., et al. *Truly three dimensional structures microfabricated by laser chemical processing*. in *Solid-State Sensors and Actuators, 1991. Digest of Technical Papers, TRANSDUCERS '91., 1991 International Conference on*. 1991.
27. Reynolds, N.J., *Materials Science and Technologies : Functionally Graded Materials*. 2011, New York, NY, USA: Nova Science Publishers, Inc.
28. Hofmann, D.C., et al., *Compositionally graded metals: A new frontier of additive manufacturing.* Journal of Materials Research, 2014. **29**(17): p. 1899-1910.
29. Mahamood, R.M., et al., *Functionally graded material: an overview.* 2012.
30. Shiota, I. and Y. Miyamoto, *Functionally graded materials 1996*. 1997: Elsevier.
31. Chua, C.K., et al., *Selective laser sintering of functionally graded tissue scaffolds.* MRS Bulletin, 2011. **36**(12): p. 1006-1014.
32. Müller, E., et al., *Functionally graded materials for sensor and energy applications.* Materials Science and Engineering: A, 2003. **362**(1–2): p. 17-39.
33. Pompe, W., et al., *Functionally graded materials for biomedical applications.* Materials Science and Engineering: A, 2003. **362**(1–2): p. 40-60.
34. Niendorf, T., et al., *Functionally Graded Alloys Obtained by Additive Manufacturing.* Advanced Engineering Materials, 2014. **16**(7): p. 857-861.
35. Li, L., W.U.H. Syed, and A.J. Pinkerton, *Rapid additive manufacturing of functionally graded structures using simultaneous wire and powder laser deposition.* Virtual and Physical Prototyping, 2006. **1**(4): p. 217-225.
36. Sankar, B.V., *An elasticity solution for functionally graded beams.* Composites Science and Technology, 2001. **61**(5): p. 689-696.
37. Gupta, N., et al., *Ballistic Studies on TiB2-Ti Functionally Graded Armor Ceramics.* Defence Science Journal, 2012. **62**(6): p. 382-n/a.
38. Matsuo, S., F. Watari, and N. Ohata, *Fabrication of a functionally graded dental composite resin post and core by laser lithography and finite element analysis of its stress relaxation effect on tooth root.* Dental materials journal, 2001. **20**(4): p. 257-274.
39. Watari, F., et al., *Biocompatibility of materials and development to functionally graded implant for bio-medical application.* Composites Science and Technology, 2004. **64**(6): p. 893-908.

40. Pham, D.T. and R.S. Gault, *A comparison of rapid prototyping technologies.* International Journal of Machine Tools and Manufacture, 1998. **38**(10–11): p. 1257-1287.
41. Chua, C.K., K.F. Leong, and C.S. Lim, *Rapid prototyping: principles and applications*. 2010: World Scientific.
42. *Stratasys Introduces Digital ABS2 High-Rigidity Material for Its Polyjet 3D Printers.* UAE Government News, 2013.
43. Capel, A.J., et al., *Design and additive manufacture for flow chemistry.* Lab on a Chip, 2013. **13**(23): p. 4583-4590.
44. Wang, J. and L.L. Shaw, *Fabrication of Functionally Graded Materials Via Inkjet Color Printing.* Journal of the American Ceramic Society, 2006. **89**(10): p. 3285-3289.
45. .Ltd, S. *Connex3 System Specifications*. 2015 [cited 2015 30/05]; Available from: http://www.stratasys.com/3d-printers/production-series/connex3-systems.
46. Wehmöller, M., et al., *Implant design and production—a new approach by selective laser melting.* International Congress Series, 2005. **1281**(0): p. 690-695.
47. Abe, F., et al., *The manufacturing of hard tools from metallic powders by selective laser melting.* Journal of Materials Processing Technology, 2001. **111**(1–3): p. 210-213.
48. Sandron, S., et al., *3D printed metal columns for capillary liquid chromatography.* Analyst, 2014.
49. Beal, V.E., et al., *Evaluating the use of functionally graded materials inserts produced by selective laser melting on the injection moulding of plastics parts.* Proceedings of the Institution of Mechanical Engineers, 2007. **221**(B6): p. 945-954.
50. Vilar, R., *Laser cladding.* Journal of Laser Applications, 1999. **11**(2): p. 64-79.
51. Santos, E.C., et al., *Rapid manufacturing of metal components by laser forming.* International Journal of Machine Tools and Manufacture, 2006. **46**(12–13): p. 1459-1468.
52. Janaki Ram, G.D., C.K. Esplin, and B.E. Stucker, *Microstructure and wear properties of LENS® deposited medical grade CoCrMo.* Journal of Materials Science : Materials in Medicine, 2008. **19**(5): p. 2105-11.
53. Muller, P., P. Mognol, and J.-Y. Hascoet, *Modeling and control of a direct laser powder deposition process for Functionally Graded Materials (FGM) parts manufacturing.* Journal of Materials Processing Technology, 2013. **213**(5): p. 685-692.
54. Pei, Y.T. and J.T.M. De Hosson, *Functionally graded materials produced by laser cladding.* Acta Materialia, 2000. **48**(10): p. 2617-2624.
55. Knoppers, G., et al. *The reality of functionally graded material products*. in *Intelligent Production Machines and Systems-First I* PROMS Virtual Conference: Proceedings and CD-ROM set*. 2005. Elsevier.
56. Gibson, I., D.W. Rosen, and B. Stucker, *Additive manufacturing technologies*. 2010: Springer.
57. Masood, S.H., *Advances in fused deposition modeling*.
58. Khalil, S., J. Nam, and W. Sun, *Multi‐nozzle deposition for construction of 3D biopolymer tissue scaffolds.* Rapid Prototyping Journal, 2005. **11**(1): p. 9-17.
59. Jafari, M.A., et al., *A novel system for fused deposition of advanced multiple ceramics.* Rapid Prototyping Journal, 2000. **6**(3): p. 161-175.
60. *Stratasys Launches FDM Nylon 12.* Entertainment Close - Up, 2013.
61. Wagner Jr, J.R., E.M. Mount Iii, and H.F. Giles Jr, *1 - Extrusion Process*, in *Extrusion (Second Edition)*, J.R.W.M.M.F. Giles, Editor. 2014, William Andrew Publishing: Oxford. p. 3-11.
62. Wagner Jr, J.R., E.M. Mount Iii, and H.F. Giles Jr, *41 - Feedblocks and Dies*, in *Extrusion (Second Edition)*, J.R.W.M.M.F. Giles, Editor. 2014, William Andrew Publishing: Oxford. p. 467-476.

63. Colbert, J.A., *The extrusion of multi-layer barrier tubing from cross linked polyethylene (PEX)*. 2001. p. 59-68.
64. Shrader, E. and C. Cobb, *Co-Extrusion Printing for Low Cost and High Performance Energy Devices.*
65. Kim, G., et al., *Coaxial structured collagen-alginate scaffolds: fabrication, physical properties, and biomedical application for skin tissue regeneration.* Journal of Materials Chemistry, 2011. **21**(17): p. 6165-6172.
66. Cornock, R., S. Beirne, and G.G. Wallace. *Development of a Coaxial Melt Extrusion Printing process for specialised composite bioscaffold fabrication*. in *Advanced Intelligent Mechatronics (AIM), 2013 IEEE/ASME International Conference on*. 2013.
67. *PLA UP Premium Filament*. 2015 [cited 2015 03/05]; Available from: http://store.3dprintingsystems.com/3D_Printer_Filament/UP-PLA?sort=pd.name&order=ASC.
68. *ABS Filament*. 2015 [cited 2015 03/05]; Available from: http://store.3dprintingsystems.com/3D_Printer_Filament/1.75mm_ABS_Filament_Radical_Red?sort=pd.name&order=ASC.
69. Garlotta, D., *A Literature Review of Poly(Lactic Acid).* Journal of Polymers and the Environment, 2001. **9**(2): p. 63-84.
70. Eng, B., *Fabrication of FDM 3D objects with ABS and PLA and determination of their mechanical properties.*
71. N. Turner, B., R. Strong, and S. A. Gold, *A review of melt extrusion additive manufacturing processes: I. Process design and modeling.* Rapid Prototyping Journal, 2014. **20**(3): p. 192-204.
72. *Hybrid Stepper Motors*. Size 42mm High Torque Hybrid Stepping Motor 2015 [cited 2015 31/05]; Available from: http://www.motioncontrolproducts.com/pdfs/hybrid-stepper-motors.pdf.
73. *Miniature Switches*. Ultra Miniature Microswitches 2015 [cited 2015 31/05]; V1.0:[Available from: http://camdenboss.com/media/category/files/399-CSMU0100.pdf.
74. *High Heat-Resistance and High Sensitive Thermistor*. GT Thermistor 2015 [cited 2015 31/05]; Available from: http://www.mouser.com/ds/2/362/semitec%20usa%20corporation_gtthermistor-549366.pdf.
75. *ATmega2560 - Arduino Pin Mapping*. 2015 [cited 2015 31/05]; Available from: http://www.arduino.cc/en/Hacking/PinMapping2560.
76. *DMOS Microstepping Driver with Translator and Overcurrent Protection*. 2015 [cited 2015 31/05]; Available from: https://www.pololu.com/file/download/a4988_DMOS_microstepping_driver_with_translator.pdf?file_id=0J450.
77. matbase.com. *General Purpose ABS*. 2014 [cited 2014 4/11]; Available from: http://www.matbase.com/material-categories/natural-and-synthetic-polymers/commodity-polymers/material-properties-of-acrylonitrile-butadiene-styrene-general-purpose-gp-abs.html#properties.
78. Sin, L.T., A.R. Rahmat, and W.A.W.A. Rahman, *3 - Thermal Properties of Poly(lactic Acid)*, in *Polylactic Acid*, L.T.S.R.R.A.W.A. Rahman, Editor. 2013, William Andrew Publishing: Oxford. p. 109-141.
79. Sin, L.T., A.R. Rahmat, and W.A.W.A. Rahman, *4 - Chemical Properties of Poly(lactic Acid)*, in *Polylactic Acid*, L.T.S.R.R.A.W.A. Rahman, Editor. 2013, William Andrew Publishing: Oxford. p. 143-176.

80. Sin, L.T., A.R. Rahmat, and W.A.W.A. Rahman, *5 - Mechanical Properties of Poly(lactic Acid)*, in *Polylactic Acid*, L.T.S.R.R.A.W.A. Rahman, Editor. 2013, William Andrew Publishing: Oxford. p. 177-219.
81. Matweb.com. [cited 2014 4/11]; Available from: http://asm.matweb.com/search/SpecificMaterial.asp?bassnum=MTP641.